Characterization of Heat Storage Materials with Neutron Scattering and Imaging Techniques

Perizat Berdiyeva

Dissertation for the degree of Philosophiae Doctor

Department of Chemistry

Faculty of Mathematics and Natural Sciences

University of Oslo

2020

Series of dissertations submitted to the
Faculty of Mathematics and Natural Sciences, University of Oslo
No. 2304

ISSN 1501-7710

Cover: Hanne Baadsgaard Utigard.
Print production: Reprosentralen, University of Oslo.

Armandai bilseñ qialga qanat kush biter,

Zayaga ketpes, armanyñ ushin tokken ter,

Tozimin shyñdap, qairatyn janyp, qashanda

Muratqa jeter, jaqsynyñ qosyn jekken er.

Ata - Abdissattar Ospanov

Preface

This dissertation is submitted for the degree of Philosophiae Doctor at the Department of Chemistry, Faculty of Mathematics and Natural Sciences, University of Oslo. The research presented here was conducted at the Institute for Energy Technology (IFE), Technical University of Denmark (DTU), FRM-II research reactor (MLZ), ILL neutron source, ISIS pulsed neutron and muon source, National Laboratory of Standards and Technology (NIST), the Swiss Light Source (SLS) and at the Diamond Light Source (DLS), between June 2017 and May 2020 as a part of the Neutrons for Heat Storage (NHS) project funded by NordForsk under the supervision of Professor Bjørn Christian Hauback and co-supervisors Professor Helmer Fjellvåg and Dr. Stefano Deledda.

Chapter 1 of this dissertation explains the motivation for the work and discusses the issues of energy efficiency and storage, focusing on thermochemical energy storage. The concept of the work is also described where the importance of neutron imaging technique is accentuated. Chapter 2 describes the experimental techniques used throughout the research project. Chapter 3 presents the most important findings from the scientific publications and manuscripts written during this PhD project. Chapter 4 provides a summary of the project and an outlook for thermochemical heat storage materials and systems.

This work was supported by NordForsk Nordic Neutron Science Program via grant No. 82206.

Perizat Berdiyeva

June 2020

Acknowledgements

First, I would like to thank my supervisors Bjørn and Stefano for all the provided help and support during my PhD-work at IFE. Thanks to Magnus S., Christoph, Marian and Kenneth for discussion and assistance with the laboratory experiments. A special thanks to Magnus N. for being a good friend and colleague throughout our PhD projects at IFE. Thanks to my colleagues from the NHS project, Didier, Rune, Anastasiia, Viktoria and Saman for the nice collaboration and their valuable contribution to my PhD-work. Thanks to Smagul for his help during my traineeship period in SOL.

Thanks to Jakob for being a nice office mate and for uncountable tea and coffee breaks with scientific and even more non-scientific discussions during his stay in Norway. There are lots of memories to recall and there will be more in the future.

A very special thanks to my friend Anjitha for her immense support and always pulling me out from home to enjoy the nice weather. Thanks for the precious time and many delicious indian meals you have always made for me and others: I will miss that the most!

To the person who is ‘guilty’ of my application for the PhD-study – Jose, thank you very much for believing in me. I would not have experienced all these moments if you had not encouraged me to try myself in research.

Tusen takk til min onkel Jørn for welcoming me in Norway, providing a nice place to live throughout my stay in this beautiful country. Thanks for being the most loyal, fun and fantastic landlord!

And last, but not least, a huge thanks to my parents, siblings, friends and relatives from very far away homeland – Kazakhstan, who have always supported me and my crazy ideas.

Abstract

Nearly three-quarters of the energy generated by society is squandered as waste heat, and industries account for around 50 % of that. A solution to this issue can be provided by a safe and efficient heat storage system, and ammonia sorption materials have the potential to fulfill the requirements and accommodate for the growing demand for effective energy capture and reuse.

This dissertation contributes to the knowledge of metal halide ammines as a potential thermochemical heat storage system, which exhibits good cyclability over a long period of time and a high efficiency. Metal halide ammines undergo desorption and absorption of NH_3-gas in a chemical reaction, which consequently results in an uptake or release of heat, respectively. These endothermic and exothermic reactions can be performed in a closed system, utilizing external waste heat for NH_3 release, typically in the temperature range T = 20 °C to 400 °C, while the heat can be released by NH_3 reabsorption.

In this dissertation new insight is provided into a thermochemical heat storage reactor prototype using the metal halide ammine salt $Sr(NH_3)_xCl_2$ for low-temperature applications (40-80 °C). The changes in kinetics and chemical- and physical properties during NH_3 cycling are studied by neutron imaging and scattering techniques. The honeycomb-shaped scaffold has been continuously developed throughout the PhD project, based on the results obtained from the neutron imaging investigations. Initially, the macroscopic changes of the sample were investigated, which were caused by expansion and contraction of the sample during NH_3 ab- and desorption, respectively. This resulted in mechanical stress and deformation of the stainless-steel honeycomb. Thus, the honeycomb was mechanically stabilized, but further experiments revealed a poor heat-conductivity of the honeycomb. The honeycomb was subsequently produced from aluminum, which significantly improved the heat transfer. A further improvement was obtained by confinement of $SrCl_2$ in expanded natural graphite, which increased the kinetics and heat transfer, while reducing the mechanical stress on the reactor. Here it has been demonstrated for the first time how both qualitative and quantitative analysis of thermochemical heat storage materials and systems can be performed using neutron imaging and scattering techniques.

Moreover, a more fundamental study on mixed cation $Mg_{1-x}Mn_x(NH_3)_6Cl_2$ and $Mg_{1-x}Ni_x(NH_3)_6Cl_2$ compounds is presented and discussed with respect to tailoring the kinetics and thermal properties of metal halide ammines towards applications for thermochemical heat storage.

Publication List

This dissertation is based on the following 4 publications

[I] ***In-situ* neutron imaging study of NH_3 absorption and desorption in $SrCl_2$ within a heat storage prototype reactor**

P. Berdiyeva, A. Karabanova, M. G. Makowska, R. E. Johnsen, D. Blanchard, B. C. Hauback and S. Deledda, *Journal of Energy Storage.* 2020, 29, 101388.

[II] **Neutron radiography for modeling thermochemical heat storage reactors: case study on $SrCl_2$-NH_3 system**

A. Karabanova, P. Berdiyeva, S. Soprani, R. E. Johnsen, B. C. Hauback, S. Deledda, and D. Blanchard, *Journal of Energy Storage,* 2020 *(submitted)*

[III] **$Sr(NH_3)_8Cl_2$-ENG composite for thermochemical heat storage applications studied by *in-situ* neutron imaging**

P. Berdiyeva, A. Karabanova, D. Blanchard, B. C. Hauback and S. Deledda, *Journal of Power Sources*, 2020 *(to be submitted)*

[IV] **Synthesis, structure and NH_3 sorption properties of mixed $Mg_{1-x}Mn_x(NH_3)_6Cl_2$ ammines**

P. Berdiyeva, A. Karabanova, J. B. Grinderslev, R. E. Johnsen, D. Blanchard, B. C. Hauback and S. Deledda, *Energies*, 2020, 13, 2746.

I am a co-author of the following publication, which is not part of this dissertation:

[V] **Importance of using intrinsic kinetics in modeling thermochemical heat storage system: $SrCl_2$-NH_3 case study**

A. Karabanova, P. Berdiyeva, M. van der Pal, R. E. Johnsen, S. Deledda and D. Blanchard, *Applied Thermal Engineering*, 2020 *(to be submitted)*

Selected Presentations

Talk I ‘Strontium Chloride Ammine System for Heat Storage: Neutron Imaging study’, Nordic Neutron Science Program (NNSP) meeting, Copenhagen, Denmark, 2018

Talk II ‘*In-situ* neutron imaging study of NH_3 absorption and desorption in $SrCl_2$ in a heat storage prototype reactor’, Gordon Research Seminars on Neutron Scattering, Hong Kong, 2019

Poster I ‘*In-situ* neutron imaging study of NH_3 absorption and desorption in $SrCl_2$ in a heat storage prototype reactor’, Presented at Gordon Research Conferences on Neutron Scattering, Hong Kong, 2019

Poster II ‘Neutron Imaging study of Strontium Chloride Ammine System for Heat Storage’, Presented at the Nordic Neutron Science Program (NNSP) and the Danscatt meeting, Aarhus, Denmark, 2019

The NNSP student prize was awarded for this poster.

List of abbreviations

DSC	Differential scanning calorimetry
ENG	Expanded natural graphite
FRM-II	Forschungsneutronenquelle Heinz Maier-Leibnitz
ILL	Institute Laue-Langevin
LHS	Latent heat storage
NECTAR	Neutron computed tomography and radiography
NeXT	Neutron and X-ray tomography
NI	Neutron imaging
NIST	National Institute of Standards and Technology
NR	Neutron radiography
NT	Neutron tomography
PND	Powder neutron diffraction
PXD	Powder X-ray diffraction
RT	Room temperature
SANS	Small-angle neutron scattering
SHS	Sensible heat storage
SLS	Swiss Light Source
SR-PXD	Synchrotron radiation powder X-ray diffraction
TES	Thermal energy storage
TGA	Thermogravimetric analysis
THS	Thermochemical heat storage
2D	Two-dimensional
3D	Three-dimensional

Table of Contents

Chapter 1. Introduction

1.1 Motivation

Mankind is facing extreme ecological challenges in the coming years, already triggered several decades ago by an unsustainable energy consumption. The exponentially growing world population and improved living standards are depleting Earth's resources faster than they can be regenerated, and the world's energy demand and consumption has increased exponentially in the past century. The energy sources represent a major challenge, as almost 90% of the energy is produced from fossil fuels, *e.g.* coal, gas and oil, which produce hazardous gases such as CO_2 and NO_x during combustion, commonly known as greenhouse gases.[1,2] Consequently, the average global temperature is increasing, which correlates with the increasing atmospheric CO_2 concentration (Figure 1.1). This has a severe impact on the environment, and climate change is observed all over the planet, resulting in unpredictable and more extreme weather conditions on Earth, as observed in the past decades.[3]

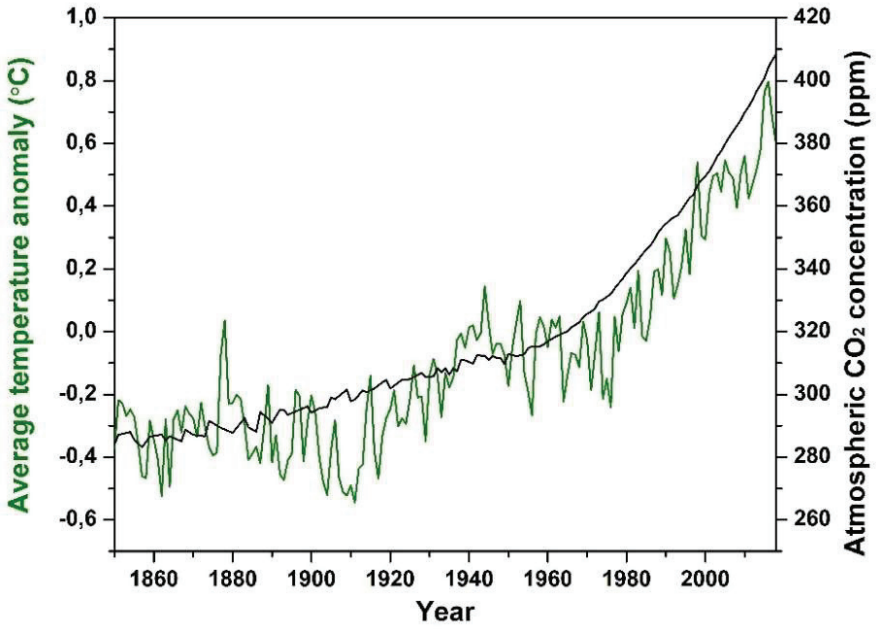

Figure 1.1. Average temperature anomaly relative to the atmospheric CO_2 concentration in the period 1850-2018. Data are obtained from ref.[4]

The atmospheric CO_2 concentration increased from 283 to 309 ppm over a century in 1850-1950s, initiated by the invention of the steam engine in 1778 and the start of the industrial revolution.[4,5] The increasing combustion of fossil fuels has resulted in an atmospheric CO_2 concentration of 413 ppm in April, 2020.[6] Over the past few decades, the global temperature has increased by approximately 0.8 °C as compared to the 1961-1990 average temperature, and is steadily increasing.[4] The correlation between global warming and greenhouse gas emissions has been evident throughout the Earth's history.[7,8] Thus, a reduction of greenhouse gas emission is a necessity to avoid global warming and the accompanying consequences. This requires a transition towards a more sustainable society, where renewable- and environmentally-friendly energy sources are a prerequisite.

Significant efforts are done to reduce the human impact on the environment, by implementing new cooperations such as "The Paris agreement", supported by the United Nations in 2016 and signed by more than 180 countries, which acknowledges the climate changes caused by greenhouse gas emissions, and aims to limit the global temperature rise well below 2 °C.[9,10] Thus, increased focus on research and new technologies for alternative energy sources has to be enforced, also motivated by the fact that fossil fuels will eventually be depleted, while the energy demand will remain.[11]

A vast progress has been done on both research and implementation of fossil-free renewable energy sources, in particular for wind and solar energy systems.[12–18] However, the energy harvested from these renewable energy sources is intermittent by nature, and depends on the weather and the day and night shifts, and they also fluctuate over the course of a month and a year. Thus, these sources are unevenly distributed over time, as well as geographically. Hence, energy storage is a necessity to store the energy produced in excessive amounts and to be available for later use.[19] The efficient use of the produced energy is vital for a sustainable society, where safe and accessible energy storage systems are needed for both large and small scale applications.[20]

Energy storage has received significant attention from the world energy outlook.[21] In particular, electrochemical energy conversion and storage in fuel cells and batteries are attractive, due to the possibility for wide implementation of this technology.[22,23] These energy systems for mobile applications could provide a significant reduction in greenhouse gas emissions from vehicles and transportation systems,[24,25] and the technology has already been widely commercialized.[26,27] Additionally, highly efficient stationary battery systems have successfully been implemented by

coupling with either photovoltaic or wind energy sources.[28–31] Heat storage systems have also gained interest for stationary applications, where they can be combined with concentrated solar power.[32,33] The use of heat storage systems combined with the renewable energy sources is another potential way of diminishing CO_2 emissions by replacing the aging heating systems based on fossil fuel combustion and providing carbon-free heating in buildings. Varying the temperature range, thermal energy storage (TES) systems can be implemented for both large- and small-scale applications in industry or domestic use, where the aging energy infrastructure can be replaced by a clean and decentralized energy production.

1.2 Thermal Energy Storage

Thermal energy storage (TES) can be applied for heating, cooling, power generation and industrial processes, where the excess thermal energy can be stored and saved for later use (Figure 1.2).[34] TES has several potential advantages, such as an increase in overall energy efficiency and energy reliability by bringing solution for waste heat and reduction in pollution of the environment, *i.e.* less CO_2 emissions into atmosphere.[35,36]

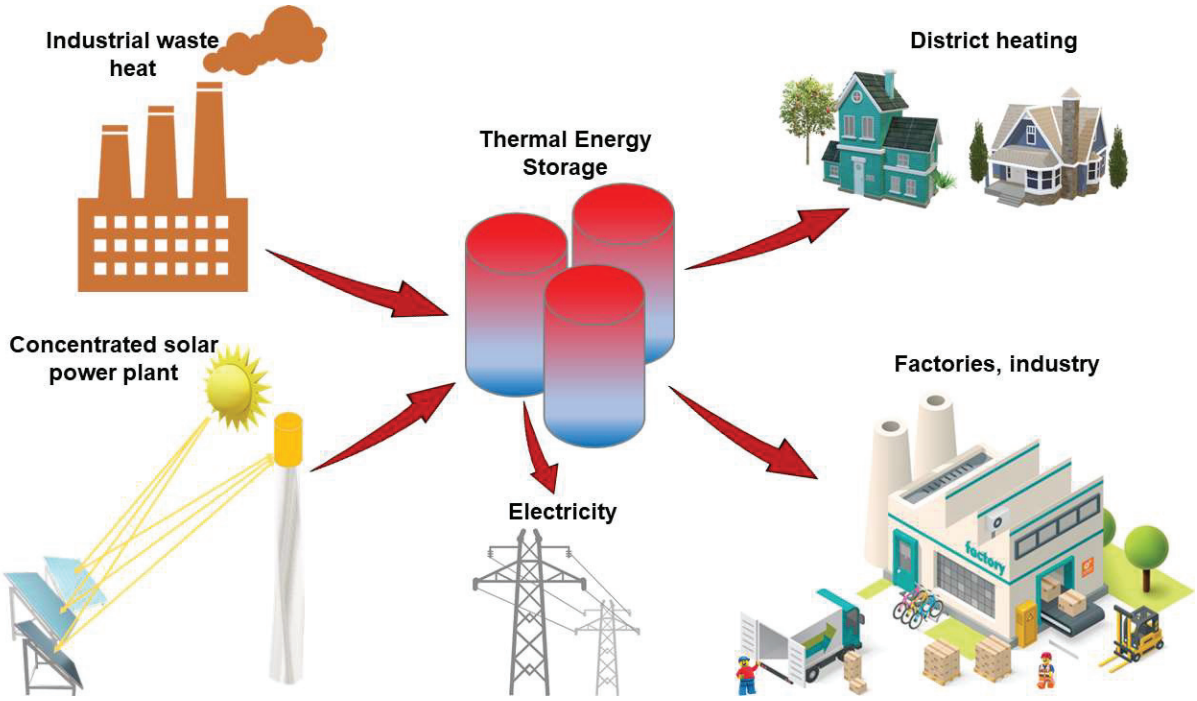

Figure 1.2. Illustration of thermal energy storage use: the produced and surplus heat captured by TES can be stored and used for various high- and low-temperature applications.

The research and development of most TES systems is focused on materials, such as investigation of storage media for various temperature ranges, storage containers and development of thermal insulation material.[34] TES systems can be divided into three different categories: *i*) sensible heat storage (SHS) systems, where the heat capacity and change in temperature of the material during charging and discharging is utilized to store the energy;[37] *ii*) latent heat storage (LHS) systems, which utilizes the enthalpy-change during the phase transition of a material;[38] and *iii*) thermochemical heat storage (THS) systems, based on endothermic and exothermic solid-gas/liquid reaction.[39] Generally, SHS and LHS systems, or a combination of both, are used in solar thermal power plants for large scale energy storage and in buildings on a smaller scale.[40–42]

SHS systems are typically used for energy storage applications at the temperatures ranging from 120 °C to 1250 °C.[43] The heat storage medium for the SHS systems is typically rock, sandstone, brick, soil, or concrete, which are densely packed in insulated steel vessels. The materials used for the SHS systems are abundant, cheap and very stable throughout their operational time, but this systems endure large heat losses.[44]

LHS systems operate at temperatures from 120 °C to 400 °C, utilizing heat-uptake or -release when the storage material undergoes a reversible phase change *e.g.* from solid-solid, solid-liquid or liquid-gas.[45,46] Typical materials used for such systems are molten salts or various metals and their alloys, and some examples are Al, Mg, Si and Zn, $Zn_{70}Sn_{30}$ and $AlSi_{12}$ alloys.[47–50] LHS generally has the benefit of being a more compact system as compared to SHS.

THS systems operate at temperatures from RT to 1200 °C, utilizing the enthalpy change associated with a chemical reaction. Reversibility is a prerequisite for these systems. When the material releases the gas in an endothermic reaction, the thermal energy is stored chemically in the separation of the solid and the gas. When the solid and the gas is recombined, the heat from the exothermic reaction can be extracted. The advantage of THS systems over SHS and LHS systems is that the heat can be stored for an indefinite amount of time. It is stored chemically and only released upon recombination of the reactants, while SHS and LHS systems gradually lose heat to their surroundings.

THS systems can generally operate based on *e.g.* hydrates, carbonates or ammines. Carbonates have been substantially investigated for thermochemical heat storage for high temperature

applications and are relevant for concentrated solar power plants.[51–53] Various relatively low price and readily available metal hydrides have also been proposed as potential high- and low-temperature heat storage materials.[54,55] Hydrates and ammines have been investigated for their potential applications in domestic heating for low-temperature applications.[56] However, some hydrates such as $MgCl_2(H_2O)_x$ and $Na_2S(H_2O)_x$ were reported to have a low cyclability and high possibility for degradation if cycled at temperatures higher than 50 °C.[57] In contrast, metal halide ammines have shown an excellent cyclability and high energy density.[58]

Thermochemical heat storage systems. Though THS systems have advantage over the SHS and LHS regarding high heat storage density, they face some limitations due to mass transfer that increases the complexity of the THS reactor design.[56] Both efficient heat and mass transfer are key elements for the efficiency of the THS reactor and system. Innovative THS reactor design is a major part of the development of THS systems, and therefore many studies have been carried out on both reactor design and materials towards achieving optimal THS system.[59–63]

The 'sorption pipes' design that consist of an outer and an inner perforated cylindrical shell with vermiculite-$CaCl_2$ as sorption material in between the shells has been investigated.[60] During discharge, the anhydrous salt absorbs water vapor, it turns to a solid crystalline hydrate and a high amount of heat is released. During charge, the heat is provided in the inner cylindrical shell and the water vapor is released. This type of reactor has a rather simple setup and achieve high energy storage densities of more than 900 $MJ \cdot m^{-3}$.

A reactor prototype containing sandwich plates with embedded metal foam with either $MgCl_2$ or LiCl salts, an ammonia source and a thermal oil for heating has also been investigated.[64] However, the swelling of the salt during absorption, slowed down the NH_3 flow, and thus preventing the cycling at a sufficient rate. This setup was improved by reducing the mass of the salt and implementing shell-n-tube type heat exchanger, containing heat exchanging fluid inside the tubes and the aluminum foam placed in aluminum container. Nevertheless, a poor performance of the reactor was observed due to the poor thermal heat transfer from the thermal oil to the tubes and plates.[65] $CaCl_2$ mixed with expanded natural graphite in a lab-scale setup was investigated using shell-n-tube design that contained eight discs with $CaCl_2$-ENG composite material with thermal oil as the heat transfer fluid inside the shell.[66] Despite the poor heat transfer from the thermal oil, a high desorption rate was observed with an energy storage density of 1512 $MJ \cdot m^{-3}$.

Many similar studies have been performed with different sorption materials and heat exchangers for waste heat recovery ($T < 100$ °C). For example, a $SrBr_2 \cdot 6H_2O$ coated heat exchanger within a honeycomb-shaped THS reactor with an efficiency of 77 % of the reactor and the overall energy storage density of 767 $MJ \cdot m^{-3}$ has been reported.[67] Similarly, $CaCl_2$ impregnated in a mesoporous ceramic in a honeycomb-shaped THS reactor has been studied, where the composite material was found to absorb more water than the original ceramic material.[68] After 25 cycles, no decomposition or cracks were observed in the system. The overall heat extraction performance of the reactor was 65 % and the overall energy storage density was 272 $MJ \cdot m^{-3}$. A $CaCl_2$-NH_3 system mixed with Ti sponges within a THS reactor has also been studied, where the improvement of the heat transfer was up to 59 % when $CaCl_2$ was embedded in Ti as the heat transfer media, as compared to unmixed $CaCl_2$.[69,70] These studies suggest that by optimizing both THS reactor design and the materials, *e.g.* mixing the sorption materials with a heat transfer matrix, the efficiency of the overall THS system can be improved.

THS systems are still considered as a new type of systems and are undergoing extensive research and development.[71] In a recent review of thermochemical heat storage materials, it was reported that the THS materials have major advantages over the conventional LHS and SHS systems in terms of cyclability.[39,56] Besides, they also exhibit high volumetric and gravimetric energy densities in a wide temperature range.[72,73]

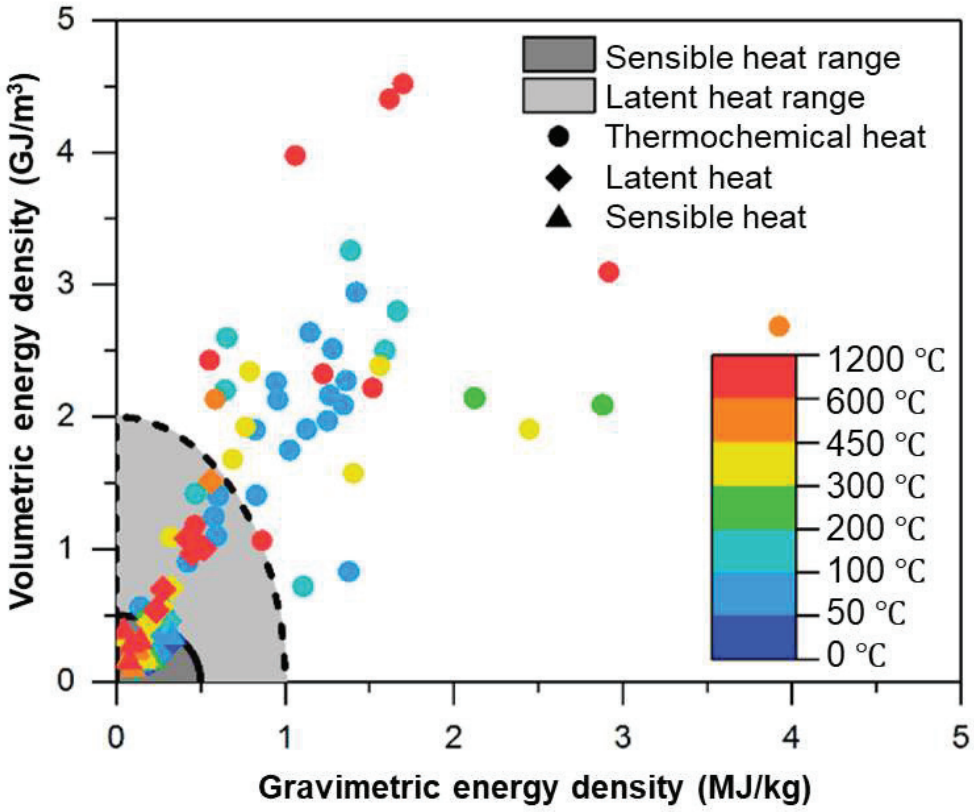

Figure 1.3. Volumetric and gravimetric energy densities of TES materials for the three primary types of heat storage, SHS, LHS and THS. Figure from ref.[72]

Typical energy densities for SHS, LHS and THS based materials are shown in Figure 1.3.[72] The triangles represent sensible heat storage materials, rhombs represent latent heat storage materials and circles depict thermochemical heat storage materials. The color indicates operating temperatures. Heat storage materials that operate *via* thermochemical reactions have the potential for significantly higher energy densities, both gravimetrically and volumetrically, as compared to those that work on sensible or latent heat (highlighted as dark gray and light gray areas, respectively).[72] Furthermore, thermochemical heat storage materials cover a large range of operating temperatures and can therefore be tailored to the desired application. However, the thermochemical storage solutions require further research on the storage materials, in order to obtain a better understanding of successful full system integration and design for practical applications. One such promising class of storage materials is the family of metal halide ammines.

1.3 Metal Halide Ammines

Ammonia and hydrogen have been proposed as alternative energy carriers compared to fossil fuels. However, ammonia is toxic and corrosive, but it can be safely stored in solid materials, where it is chemically bonded in different materials, *e.g.* inorganic salts.[74] The possibility for safe and efficient storage of ammonia gas has been exploited for metal halide ammines.[75–78]

The indirect hydrogen storage capabilities of $Mg(NH_3)_6Cl_2$, $Ca(NH_3)_8Cl_2$, $Mn(NH_3)_6Cl_2$, and $Ni(NH_3)_6Cl_2$ have been extensively investigated.[77] All four metal chloride ammines can be compacted to solid tablets with densities of more than 95% of the crystal density. This gives very high indirect hydrogen densities, both gravimetrically and volumetrically. Upon heating, NH_3 is released from the salts, and by employing an appropriate catalyst, H_2 can be released corresponding to up to 9.78 wt% H and 0.116 kg H/L for the $Ca(NH_3)_8Cl_2$ salt.[77,79] The NH_3 release from all four salts have been investigated using temperature-programmed desorption employing different heating rates. The desorption is found to be limited mainly by the heat transfer, indicating that the desorption kinetics are extremely fast. During desorption from solid tablets of $Mg(NH_3)_6Cl_2$, $Mn(NH_3)_6Cl_2$, and $Ni(NH_3)_6Cl_2$, nanoporous structures develop, which facilitate desorption from the interior of such compact tablets.[77,80,81] Density functional theory calculations reproduce trends in the desorption enthalpies for the studied systems, and suggest a mechanism where individual chains of the ammonia are released from the surface of the crystal, thus explaining the fast absorption/desorption processes.[82,83] This class of compounds has been extensively studied in the past century, and the synthesis, crystal structure and thermal stability are well established.[84–91] Metal chloride ammines can possess high gravimetric ammonia and hydrogen capacities and the amount of NH_3 that can be absorbed varies amongst the metal halides.[92–95] The NH_3 and H_2 contents depending on the metal cation and halide anion are presented in Table 1.1.

Table 1.1. Ammonia and hydrogen gravimetric densities of selected metal halide ammines.[79,84,92,96]

Metal ion	Chloride			Bromide			Iodide		
	Number of NH_3	NH_3 (wt%)	H (wt%)	Number of NH_3	NH_3 (wt%)	H (wt%)	Number of NH_3	NH_3 (wt%)	H (wt%)
Sn^{2+}	4	26.4	4.7	5	23.4	4.2	5	18.6	3.3
Ba^{2+}	8	39.6	7.0	8	31.4	5.6	10	30.3	5.4
Co^{2+}	6	44.0	7.8	6	31.8	5.6	6	24.6	4.4
Ni^{2+}	6	44.1	7.8	6	31.9	5.7	6	24.7	4.4
Fe^{2+}	6	44.6	7.9	6	32.2	5.7	6	24.8	4.4
Mn^{2+}	6	44.8	8.0	6	32.2	6.4	6	24.9	4.4
Sr^{2+}	8	46.2	8.2	8	35.5	6.3	8	28.5	5.1
Mg^{2+}	6	51.8	9.2	6	35.7	6.3	6	27.0	4.8
Li^{+}	3	54.7	9.7	4	44.0	7.8	4	33.7	6.0
Ca^{2+}	8	55.1	9.8	8	40.5	7.2	6	25.8	4.6

The chemical energy from metal halide ammines can be extracted using fuel cells, where ammonia can be used as a fuel in either direct-ammonia fuel cells or solid oxide fuel cells operating at temperatures about 400 °C.[97,98] If used for indirect hydrogen storage, ammonia is converted into hydrogen and nitrogen, where the hydrogen can be used in a polymer electrolyte membrane fuel cell operating at temperatures below ~100 °C.[99,100] However, ammonia can be poisonous for these fuel cells, thus an incomplete conversion is an issue.[101]

Metal halide ammines have shown promising applications as ammonia storage material for on-board selective catalytic reduction (SCR) of hazardous NO_x gases from diesel cars and trucks,[102–104] and thus contribute to the reduction of greenhouse gas emission from vehicle engines.[105,106] The remarkable potential of the metal halide ammines and their wide potential for application within energy storage have deepened the research also for other possible applications, *e.g.* heat storage applications.

Thermodynamics of metal halide ammines. Metal halide ammines are formed directly in an exothermic reaction between ammonia and a dry salt, often at RT.[85,107–110] However, for some metal halides, *e.g.* LiF, NaCl, KBr, MgF_2 and CaF_2, ammonia uptake is not observed at ambient

conditions.[109] Desorption of ammonia is achieved by heating the metal halide ammines to a specific temperature, where NH_3 is released in an endothermic reaction. The ammonia release temperatures can vary a lot for different materials, and the release is often a multi-step process occurring over a broad temperature interval, often with reversible ammonia ab- and desorption from 20 °C to more than 400 °C.[75,92] Thorough thermodynamic studies on different metal halide ammines have revealed good kinetics and high cyclability for ammonia ab- and desorption.[86,111] These properties suggest potential applications in thermochemical heat storage systems.[112,113]

Magnesium and 3d-block metal halides. Metal halide ammines readily form from earth alkali metals and transition metals. The ionic radii of Mg^{2+} is similar to that of the 3d-transition divalent metals, M^{2+}, and thus their structures show similarities.[114] Their metal halides absorb six ammonia equivalents[115,116] to form hexammines, and a high gravimetric ammonia density of 51.8 wt % is achieved in $Mg(NH_3)_6Cl_2$.[111,117] This compound has also been investigated for indirect hydrogen storage due to the high H_2 content of $\rho_m(H_2)$ = 9.2 wt%.[77,80,81,102,118,119] $Mg(NH_3)_6Cl_2$ thermally releases ammonia in three steps: *i*) at 142 °C (4 equivalents of NH_3), *ii*) at 230 °C (1 equivalent of NH_3) and *iii*) at 375 °C (1 equivalent of NH_3), using a backpressure of 1 bar of ammonia.[120] A similar three-step ammonia desorption is observed for the other metal halides hexammines, *e.g.* $Mn(NH_3)_6Cl_2$ releases 4 NH_3, 1 NH_3 and 1 NH_3 with desorption-temperatures at 80 °C, 180 °C and 354 °C, respectively, while $Ni(NH_3)_6Cl_2$ desorbs at 168 °C, 327 °C and 396 °C, respectively.[92] $Mg(NH_3)_6Cl_2$, $Mn(NH_3)_6Cl_2$ and $Ni(NH_3)_6Cl_2$ have the volumetric NH_3 capacities of 639, 618 and 657 $kg \cdot m^{-3}$, respectively.[121] However, their usable capacities are decreased to 426, 412 and 438 $kg \cdot m^{-3}$ due to the release of the last 2 equivalents of NH_3 at too high temperatures. The desorption temperatures are related to the charge density of the metal cation,[110] and a higher charge-density cation binds NH_3 more strongly. This is reflected by the ionic radii for Mg^{2+} (r = 0.71 Å), Mn^{2+} (r = 0.80 Å) and Ni^{2+} (r = 0.69 Å).[114]

$Mg(NH_3)_xCl_2$, $Mn(NH_3)_xCl_2$ and $Ni(NH_3)_xCl_2$ are isostructural for all the known ammines (x = 1, 2, 6) and the metal clorides.[77,116,117,122,123] The hexammines crystallize in the K_2PtCl_6 type structure, with a cubic unit cell and space group symmetry *Fm*-3*m,* where the octahedral units of $M(NH_3)_6$ are contained in a cubic lattice of Cl atoms, with each metal ion (*M*) octahedrally coordinated by six N atoms (Figure 1.4 a). The diammines crystallize in the $Cd(NH_3)_2Cl_2$ type structure, with an orthorhombic unit cell and space group symmetry *Cmmm*. Each Cl atom is

shared by two neighboring metal atoms in edge-sharing octahedral chains, and each metal ion is octahedrally coordinated by two ammonia and four chloride in a trans geometry (Figure 1.4 b). The monoammines crystallize in the $Ni(NH_3)Cl_2$ type structure, with a monoclinic unit cell and space group symmetry *I*2/*m*. Each Cl atom is shared by three metal atoms in edge-sharing double octahedral chains, and the metal ion is octahedrally coordinated by one ammonia and five chloride (Figure 1.4 c). MCl_2 (*M* = Mg, Mn and Ni) crystallizes in the $CdCl_2$ type structure, with a trigonal unit cell and space group symmetry *R*-3*m*.[124–126] The octahedral units of [MCl_6] are connected via sharing half of the edges, resulting in layers of MCl_2 (Figure 1.4 d). The volume of the unit cells decreases in the order Mn > Mg > Ni, in accordance with the decreasing ionic radii.

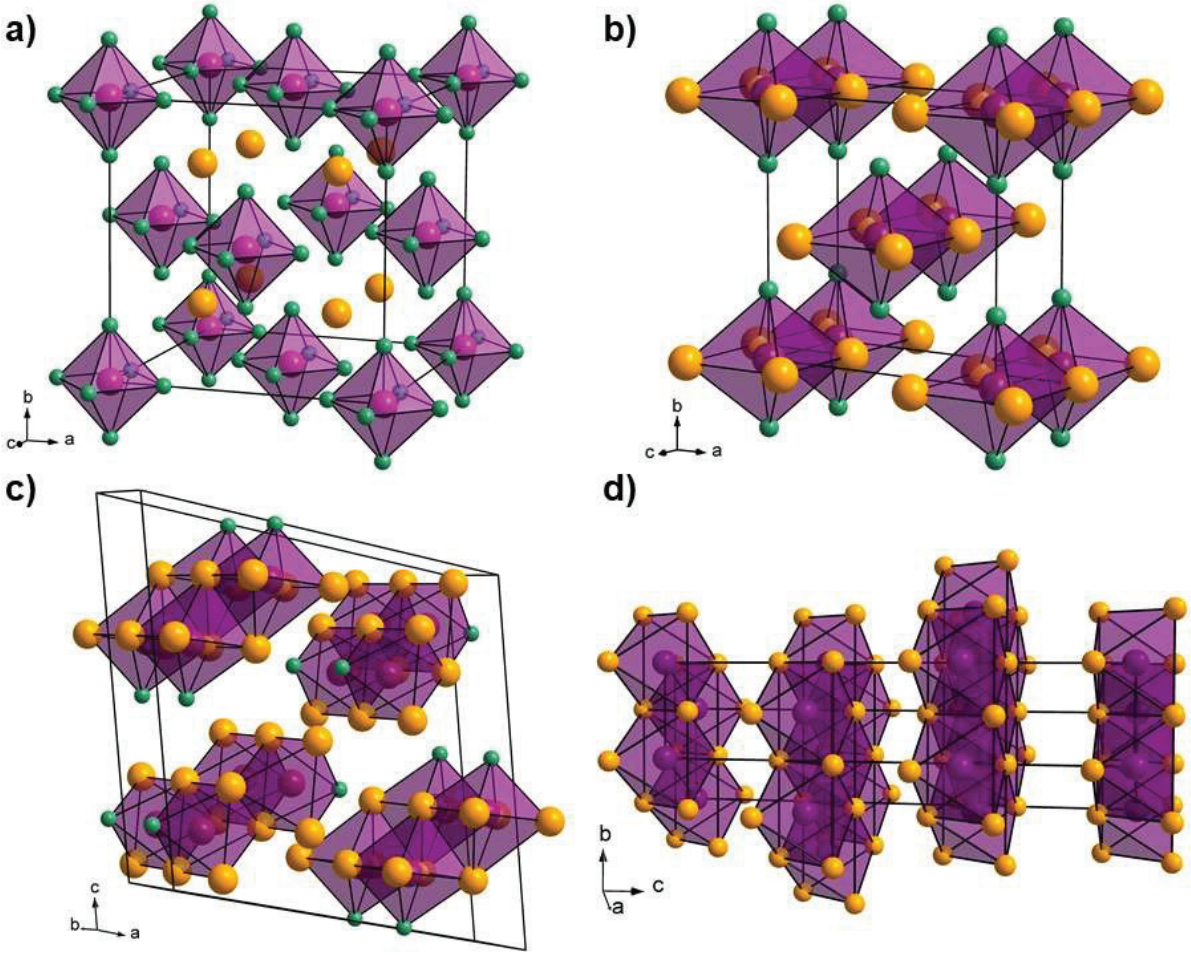

Figure 1.4. Crystal structures of a) $M(NH_3)_6Cl_2$ (*M* = Mg, Mn, Ni; *Fm*-3*m*), b) $M(NH_3)_2Cl_2$ (*Cmmm*), c) $M(NH_3)Cl_2$ (*I*2/*m*) and d) MCl_2 (*R*-3*m*). Color scheme: *M* – violet, N – green, Cl – yellow. H is omitted for clarity.

Calcium, strontium and barium chloride ammines. $Sr(NH_3)_8Cl_2$ has been suggested as one of the most promising metal halide ammines for ammonia storage, both due to a high volumetric NH_3 capacity of 642 kg·m^{-3} at RT and to the favorable NH_3 desorption temperatures of around 40-50 °C against a backpressure of 1 bar of NH_3.[127,128] Seven NH_3 equivalents are desorbed at low temperatures (40-50 °C), whereas the last NH_3 equivalent is more strongly bounded, and a temperature of around 150 °C is required for desorption and reformation of $SrCl_2$. Thus, the accessible volumetric ammonia density of $Sr(NH_3)_8Cl_2$ is 562 kg·m^{-3} for low-temperature applications (T < 50 °C), and this makes it the most promising metal halide ammine for low-temperature applications.[129]

In comparison, an octammine is also formed for calcium chloride, $Ca(NH_3)_8Cl_2$ with a volumetric NH_3 capacity of 678 kg·m^{-3}. Six NH_3 equivalents are desorbed at temperatures below 100 °C, but the last two ammonia equivalents are desorbed between 175 and 275 °C,[77] lowering the accessible volumetric ammonia density to 509 kg·m^{-3}. $Ba(NH_3)_8Cl_2$ has a relatively low volumetric NH_3 capacity of 597 kg·m^{-3} at RT, but has the advantage that all eight ammonia equivalents are released in one step below 50 °C.[79,121] However, $BaCl_2$ is highly toxic which limits its application.[130]

$Sr(NH_3)_8Cl_2$ crystallizes in an orthorhombic unit cell with space group symmetry *Pnma* and unit cell parameters a = 12.22187(4), b = 7.47501(2), c = 15.34330(5) Å and V = 1401.74(1) Å^3 at 20 °C (Figure 1.5 a). In the crystal structure, Sr^{2+} is coordinated by eight ammonia molecules through the lone pair on nitrogen, forming isolated $[Sr(NH_3)_8]^{2+}$ polyhedra that are shaped as double capped trigonal prisms.[128] Cl^- acts as counter ions, and the structure is built from close-packing of $[Sr(NH_3)_8]^{2+}$ polyhedra (Figure 1.5 a).[128] Depending on the partial pressures of ammonia and the heating rate during desorption, $Sr(NH_3)_8Cl_2$ may form either $Sr(NH_3)_2Cl_2$ or $Sr(NH_3)Cl_2$. $Sr(NH_3)_2Cl_2$ is isostructural to $Ca(NH_3)_2Cl_2$ and crystallizes in space group *Abm*2 with unit cell parameters a = 6.1812(3) Å, b = 8.1532(4) Å, c = 12.6659(8) Å and V = 638.32 Å^3 at 25 °C.[96,127] Sr^{2+} coordinates to four Cl^-, forming layers of corner-sharing $[Sr(NH_3)_2Cl_4]$ octahedra in the *ab* plane (Figure 1.5 b). $Sr(NH_3)Cl_2$ crystallizes in space group *Cmcm* with unit cell parameters a = 4.4785(1) Å, b = 14.2403(5) Å, c = 7.4883(2) Å and V = 477.57 Å^3 at 35 °C.[127] Sr^{2+} is seven-fold coordinated to six chlorine atoms and one NH_3 molecule, forming a capped trigonal prism which form layers in the *ac* plane with NH_3 pointing out from those layers (Figure 1.5 c). $SrCl_2$ crystallizes in the CaF_2 type structure with a cubic unit cell, space group symmetry *Fm*-3*m* and

unit cell parameters a = 6.9792(5) Å and V = 339.95 Å^3 at RT.[131] The structure is built from a *fcc* packing of the Sr^{2+} cations, while the Cl^- occupy the tetrahedral positions in the cation lattice. Thus, each Sr^{2+} is coordinated by eight Cl^- in a cubic arrangement (Figure 1.5 d).[132]

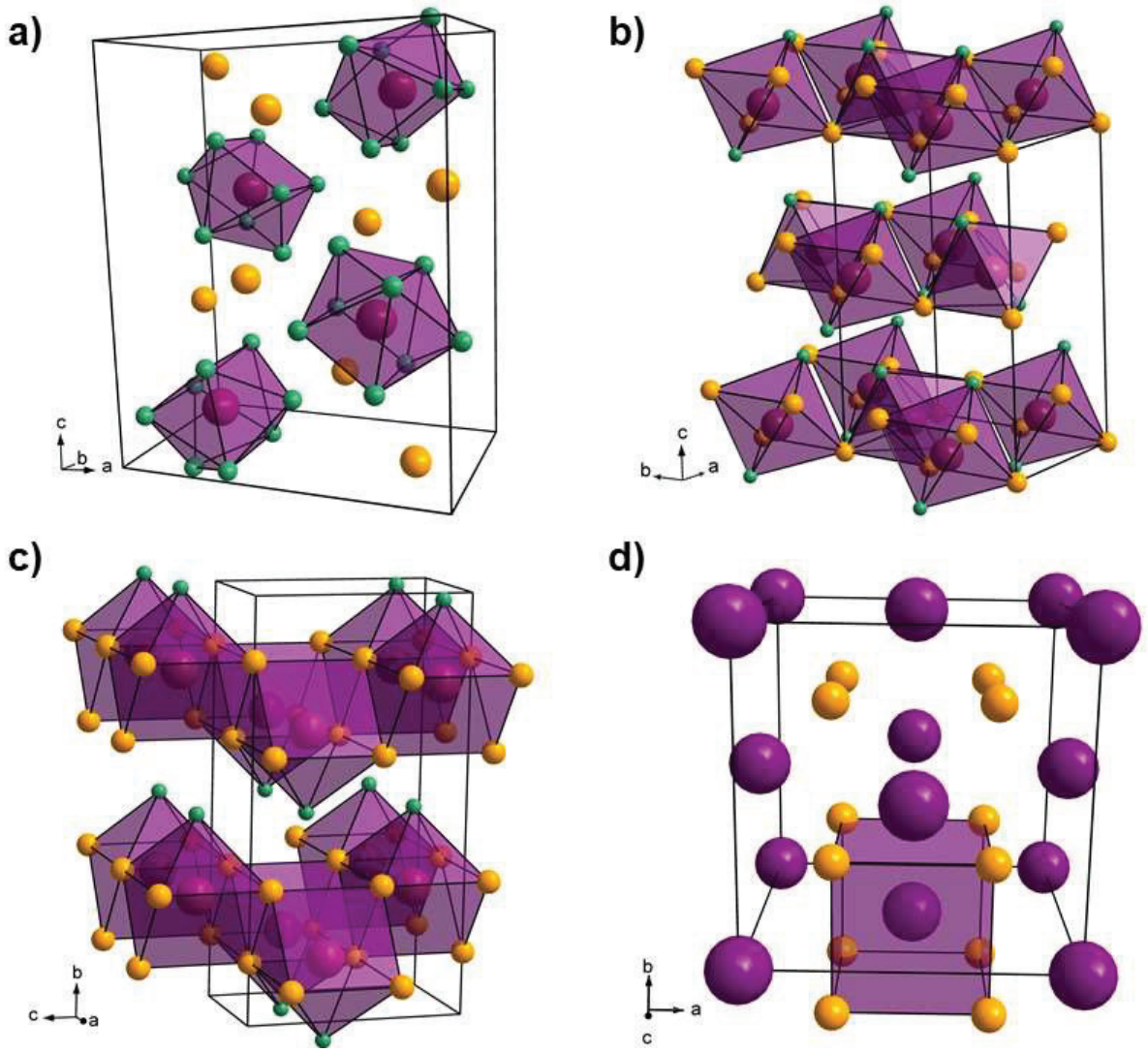

Figure 1.5. Crystal structures of a) $Sr(NH_3)_8Cl_2$ (*Pnma*), b) $Sr(NH_3)_2Cl_2$ (*Abm*2), c) $Sr(NH_3)Cl_2$ (*Cmcm*) and d) $SrCl_2$ (*Fm*-3*m*). Color scheme: Sr – violet, N – green and Cl – yellow. H is omitted for clarity.

Tuning the thermal properties of metal halide ammines. The possibility of tuning the ammonia storage properties of metal halide ammines has been extensively investigated, and one approach is by formation of solid solutions.[121,133,134] The binding energy of ammonia with the surrounding ions

strongly depends on the elements and structures of the metal halides.[127] Thus, the binding energy can be tailored by mixing metal halides due to the changes in the crystal structures and ionic radii of the elements.[135]

Tunable ammonia desorption properties were demonstrated for the mixed cation compounds $Ca_{1-x}Sr_x(NH_3)_8Cl_2$ and $Sr_{1-x}Ba_x(NH_3)_8Cl_2$. It was found that the temperatures for ammonia desorption could be altered by changing the mixing ratio, and thus tailored towards a desired desorption temperature.[103,121,133,134] Similarly, the crystal structures and ammonia storage properties were studied for the mixed anion compounds $CaCl_2$-$CaBr_2$, $SrCl_2$-$SrBr_2$ and $SrCl_2$-SrI_2, and the intermediate ammonia storage properties were shown.[103,136,137] Solid solution between $MgCl_2$ and either $MnCl_2$ or $NiCl_2$ and their corresponding ammines has been demonstrated in this PhD dissertation. These results will be discussed in more detail in Section 3.5.

1.4 Scope of this work

Thermal energy storage plays a pivotal role in a carbon-free energy society and is important for an increase in the effective use of energy. This project focuses on the investigations of metal halide ammines as potential thermochemical heat storage materials for waste heat recovery. Endothermic and exothermic sorption reactions between metal halide and NH_3 gas at temperatures in the range 20-400 °C make these systems very promising candidates for THS applications, with a prospect in the district heating.

Materials with high energy densities, which can release the energy in controlled manner when heated, can be favorable for heat storage applications. In this work, $Sr(NH_3)_8Cl_2$ and its composites with expanded natural graphite (ENG) were studied for thermochemical heat storage. This material was chosen based on the high storage capacity and cyclability at low temperatures. Thus, it is an excellent candidate for waste heat recovery applications, where the operating temperatures are aimed for the range 40-80 °C.

Waste heat can be stored and saved for later use in a closed THS system with metal halide ammines as illustrated in Figure 1.6 for metal halide ammines. Excess heat generated by an external source can be transferred to the solid $Sr(NH_3)_8Cl_2$, which subsequently releases ammonia gas in an endothermic reaction. The released ammonia gas can then be condensed in a second reservoir and kept in a liquid state. When the connection between the desorbed $SrCl_2$ salt and liquid ammonia is

closed, the system can be retained at ambient conditions indefinitely. Once the heat is needed, the connection can be opened, and the ammonia can be reabsorbed by $SrCl_2$ in an exothermic reaction. The reaction is spontaneous at RT and results in the formation of $Sr(NH_3)_8Cl_2$. This exothermic reaction can provide heat which can be utilized, *e.g.* for domestic heating.

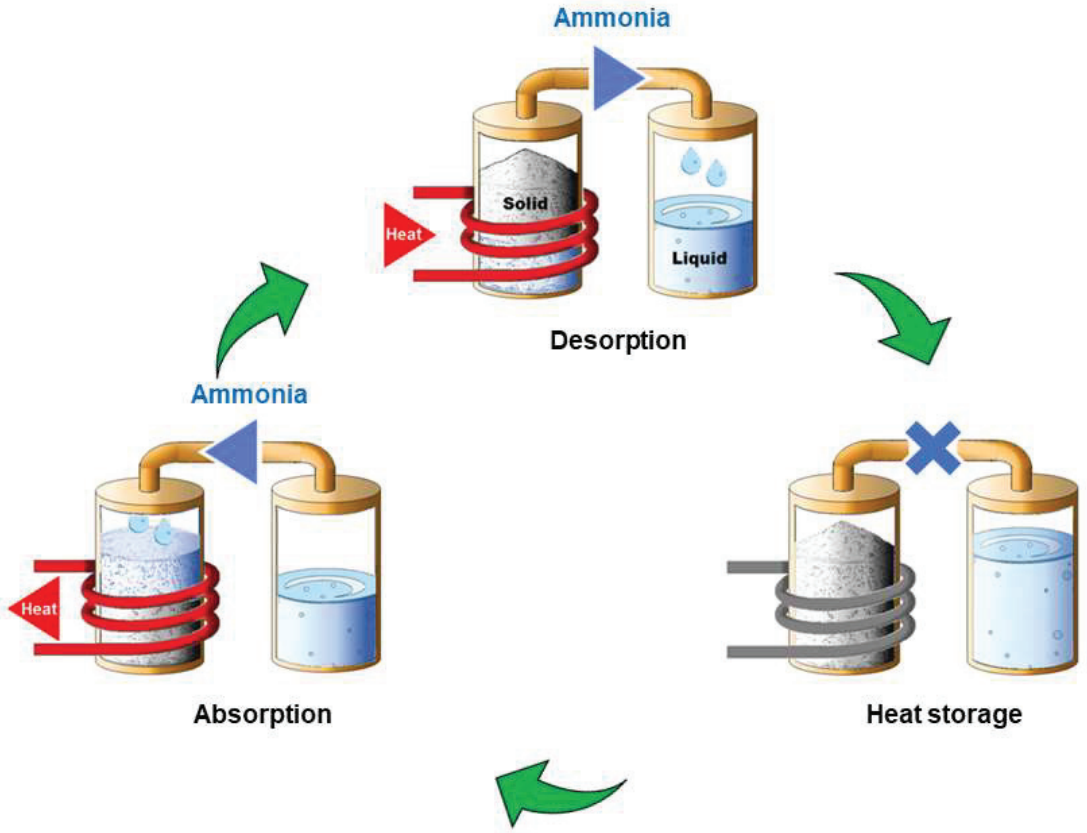

Figure 1.6. Schematic representation of the operation of a THS system of metal halide ammines. The green arrows indicate the workflow of the THS system. Desorption occurs when heat is given into the system. When the valve is closed, the heat is chemically stored as liquefied NH_3, while the NH_3 is absorbed when the valve is opened again, and the heat may be extracted.

Safe operation of the THS system during ammonia cycling is essential. Therefore, it is crucial that the storage material is thoroughly investigated during ammonia cycling. While the crystal structure of $SrCl_2$ and the corresponding ammines are well known (see Section 1.3), investigations of the changes in the macro- and microstructures are scarcely reported, whilst they change significantly during ammonia ab- and desorption, due to the significant volume changes of up to 300 %.

Thus, for safe and efficient operation of the THS reactor, a better understanding of the variations on different length scales is essential. This is addressed in this dissertation, and for the first time *via* neutron imaging and small-angle neutron scattering. These methods provide new valuable information on the materials during operation of the THS reactor prototype.

The main focus of this dissertation is on the use of neutron radiography and tomography. *In-situ* neutron radiography (2D) studies can provide significant knowledge on the ammonia uptake and release processes in the material, *e.g.* homogeneous or inhomogeneous ammonia absorption and desorption. Moreover, by following the ammonia desorption process, the efficiency and heat conductivity of the reactor components (a honeycomb-shaped scaffold in our case) can be determined. Neutron tomography (3D) studies allow in-depth investigation of the honeycomb. Furthermore, both qualitative and quantitative analysis of the obtained neutron radiography data can be performed, and the precise amount of absorbed or desorbed ammonia can be calculated. A depiction of the process is illustrated in Figure 1.7.

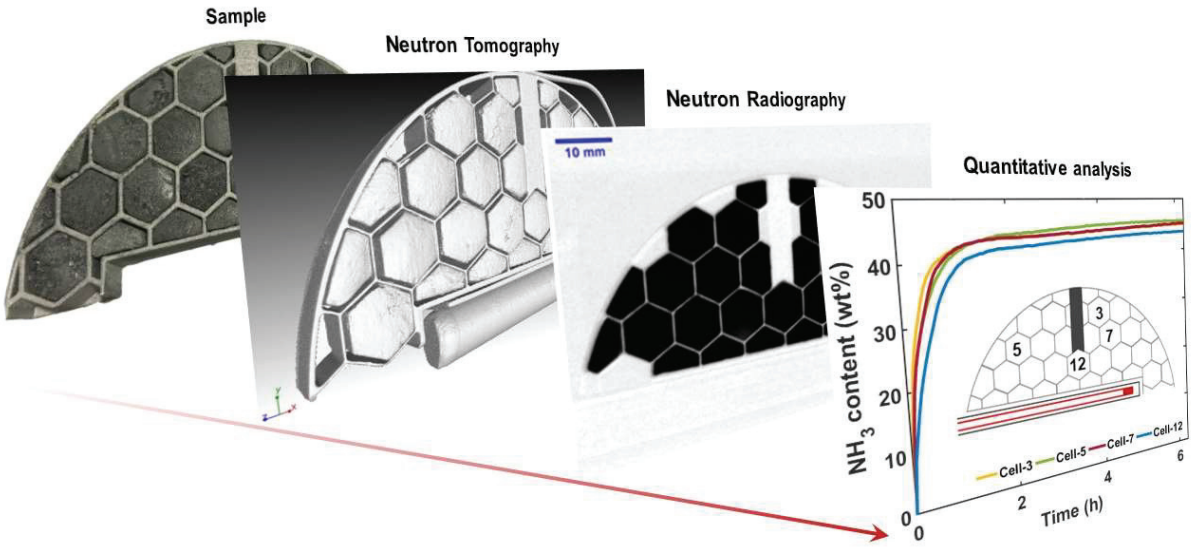

Figure 1.7. Demonstration of neutron imaging study process from sample preparation to neutron imaging data analysis.

The details of the neutron imaging instrumentation and the experimental setup are described in Chapter 2. The continuous design and optimization of the THS reactor prototype, honeycomb and the storage material are presented in Publication I-III, and described in more details in Chapter 3.

Chapter 2. Synthesis and Characterization Methods

2.1 Synthesis

The samples are hydroscopic and must be handled in an inert atmosphere. An Ar-filled glovebox (< 0.1 ppm of O_2 and H_2O) has been used during sample handling and during the synthesis.

2.1.1 Mechanochemical Milling and Heat Treatment

The mechanochemical technique with high-energy ball milling was used for synthesis of the samples presented in this dissertation. This technique can reduce the particle size of the reactants and promote solid-solid reactions. Homogeneous samples are obtained from this method, due to thorough mixing of the reactants during the milling process and, at the same time, the particle size is decreased due to the impact between powder and balls. This improves the reactivity of the sample due to the increased surface area of the particles. The high force resulting from the impact between the balls and powder may trigger formation of new compounds and polymorphs, which may not be obtained by other synthesis methods.[138]

For high-energy ball milling, the sample is loaded into a vial with balls and is sealed in argon atmosphere. Two of such vials are inserted in the ball milling equipment for mass balance. The vials are then shaken in a complex motion that combines back-and-forth swings with short lateral movements resulting in both high impact and grinding effect from the mechanical milling (Figure 2.1).

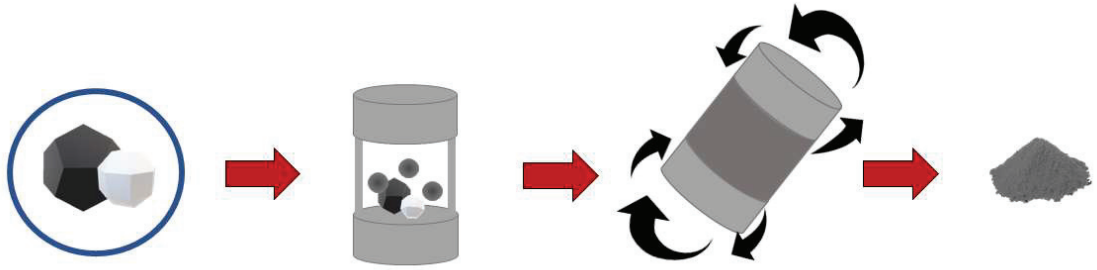

Figure 2.1. Schematic representation of the synthesis procedure using high-energy ball milling.

Several parameters can be altered during this type of synthesis: the milling time, the pause time and the number or size of the balls, which all contribute to the effects induced by the

mechanochemical treatment. Adjusting the milling time can ensure full conversion of the reaction, while extended milling time may lead to formation of amorphous compounds. Pause time is used to avoid overheating of the sample during milling. The number or size of balls relative to the amount of sample (ball-to-powder ratio) should be appropriate to achieve the right grinding effect, but a too high ratio may result in contamination from the balls.[139] For planetary ball milling, the milling intensity can be tweaked, while it is fixed for high-energy ball milling.

The synthesis of compounds presented in this dissertation were performed using a SPEX SamplePrep 8000D Dual Mixer high-energy ball mill. The powders were placed in a 25 mL hardened steel vial together with hardened steel balls (Ø = 10 mm) in a ball-to-powder mass ratio of 16:1. The intensity of the milling process was fixed, and the milling program was for one hour with no pause time.

Heat treatment after mechanochemical milling was used to improve the crystallinity of the sample, typically by keeping the sample at temperatures (T > 300 °C) for several days. The samples were placed in a stainless-steel cylinder, sealed in argon atmosphere and placed in an in-house built oven and heated with 1 °C·min^{-1} and kept under isothermal conditions. The temperature during the heat treatment is crucial parameter in order to obtain the optimal results. For example, crystallinity of the $Mg_{1-x}Mn_x(NH_3)_6Cl_2$ and $Mg_{1-x}Ni_x(NH_3)_6Cl_2$ solid solutions presented in this dissertation is improved by heating them up to 350 °C, while heating to higher temperatures might result in phase separation of the compounds, melting, or decomposition. To avoid this, TGA-DSC measurements were performed prior to heat treatment of the samples, in order to obtain precise crystallization temperatures of the compounds or even more information about thermal properties of the compounds (Section 2.2).

For this dissertation, mechanochemical synthesis and heat treatment were utilized for solid-solid reactions to form solid solutions, *e.g.* $Mg_{1-x}Mn_x(NH_3)_6Cl_2$ and $Mg_{1-x}Ni_x(NH_3)_6Cl_2$. Additionally, thermal treatments were used for the dehydration of the precursor materials MCl_2 (M = Mn, Ni), to ensure that the compounds were water free by heating them up under dynamic vacuum.

2.2 Thermal and Volumetric Analysis

2.2.1 Thermogravimetric Analysis and Differential Scanning Calorimetry (TGA-DSC)

Thermogravimetric analysis (TGA) provides information on mass change during heating of the sample. This is often combined with differential scanning calorimetry (DSC), which is used to characterize thermal events, such as endo- and exothermic reactions. DSC signals are observed as a difference in the heat flow between the sample and the reference. When an exothermic reaction occurs, the heat flow decreases on the sample side due to the released energy, while for an endothermic reaction the heat flow to the sample increases as a result of the consumed energy. The analysis of the TGA-DSC data may provide insight into the *i*) crystallization temperature; *ii*) activation energies by applying the Kissinger method;[140] *iii*) the gas release temperature, amount of gas and decomposition pathways of the compounds, *iv*) melting temperature.

Thermogravimetric analysis (TGA) and differential scanning calorimetry (DSC) of the mixed cation $Mg_{1-x}Mn_x(NH_3)_6Cl_2$ and $Mg_{1-x}Ni_x(NH_3)_6Cl_2$ solid solutions presented in this dissertation were obtained using a Netzsch STA 449 F3 Jupiter apparatus. In a typical experiment, the samples (~10-30 mg) were placed in an Al crucible with a pierced lid under protective argon atmosphere and heated from 25 °C to 500 °C $\Delta T/\Delta t$ = 5 °C·min^{-1}) in an argon flow of 50 mL·min^{-1}. For Kissinger analysis, the samples were measured with different heating rates, $\Delta T/\Delta t$ = 1-40 °C·min^{-1} to obtain the activation energies for ammonia desorption. Prior to the TGA-DSC measurements, the baselines were obtained for each set of experiment with the same heating rates.

2.2.2 Sieverts Apparatus

Sieverts type apparatus can be used for solid-gas reactions for investigations of the reaction kinetics. These reactions can be performed in cycles where the absorption and desorption processes are studied. Typically, Sieverts apparatus contains a gas source, calibrated volume and an oven. The pressure of the gas in the system is controlled during the sorption reactions at ambient or elevated temperatures. By monitoring the gas pressure drop or increase (ΔP) in the system, the number of desorbed or absorbed molecules (Δn) in the formula unit can be calculated using the formula of the ideal gas (Equation 2.1). V is the volume of the system, R is the gas-constant and T is the temperature.

$$\Delta n = \frac{\Delta PV}{RT} \tag{2.1}$$

An in-house built Sieverts apparatus at the Department of Energy Conversion and Storage, Danish University of Technology (DTU), was used for preparation, cycling and activation of $SrCl_2$ and $SrCl_2$-ENG composite materials for the small-angle neutron scattering and neutron imaging experiments (Subsection 2.3.2 and 2.3.3). Furthermore, the NH_3 absorption and desorption studies of the mixed cation $Mg_{1-x}Mn_x(NH_3)_6Cl_2$ and $Mg_{1-x}Ni_x(NH_3)_6Cl_2$ solid solutions were performed using this Sieverts apparatus.

2.3 Structural Characterization

2.3.1 X-ray and Neutron Powder Diffraction

Diffraction techniques, such as powder X-ray diffraction (PXD) or powder neutron diffraction (PND) are powerful tools for phase identification, characterization and structure determination of solid crystalline compounds. Each compound results in a unique diffraction pattern dependent on the composition, the atomic position within the crystal structure and the unit cell parameters. The techniques are based on the coherent scattering of X-rays or neutrons, which interact with the electrons or the nuclei, respectively. This scattering results in a diffraction pattern with Bragg peaks at specific angles as described by the Bragg's law:

$$2d \cdot sin\theta = n \cdot \lambda \tag{2.2}$$

where $2d \cdot sin\theta$ describes the path difference between two waves enduring interference, θ is the reflected angle of the wave, λ is the wavelength of the incident wave, n is a positive integer and d is an interplanar distance between the lattice planes of the crystalline material (Figure 2.2).

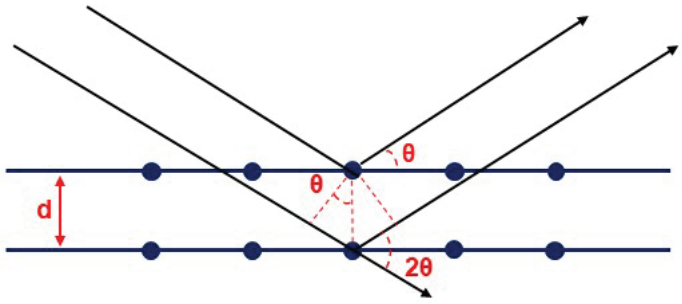

Figure 2.2. Visualization of Bragg's law.

Valuable information can be extracted from the diffraction pattern. The peak positions give information on the periodicity of the structure, the lattice parameters and the volume of the unit cell, while the intensities of the Bragg peaks contain information on the relative positions of the atoms within the unit cell and the thermal vibrations. Microstructural analysis of the peak shapes can provide additional information about strain and stress of the particles.

Powder X-ray Diffraction. Powder X-ray diffraction (PXD) is a valuable tool in materials science, due to the ease of the technique and the amount of information that can be collected from the diffraction data. X-rays interact with the electrons and the scattering length depends on the number of electrons. While each element has a unique scattering power, neighboring elements in the periodic table may be challenging to distinguish from each other. Furthermore, scattering from light elements may be negligible in compounds containing heavier elements, thus the positions of light elements such as H are often very challenging to determine from X-rays.

The preliminary studies on some of the compounds discussed in this dissertation were performed using a Bruker D8 Advance diffractometer with Cu – Kα radiation ($\lambda_{K\alpha1}$ = 1.5406 Å, $\lambda_{K\alpha2}$ = 1.5444 Å). The samples were typically loaded into borosilicate capillaries (Ø = 0.5 mm) and sealed with glue in the glovebox. Data were usually collected in the 2θ range 5 – 100°.

In-situ Synchrotron Radiation Powder X-ray Diffraction (SR-PXD). X-rays generated by a synchrotron ring provide a well-collimated X-ray beam with intensities several orders of magnitude higher than conventional laboratory X-ray diffractometers, and therefore providing rapid and high-quality diffraction data. This allows to study reactions *in-situ*, *i.e.* data can be collected during variable temperature or pressure, and changes in the crystalline compounds can be detected. Thus, *in-situ* measurements can provide information on the formation of intermediate phases, decomposition products, thermal expansion, changes in the crystallite size and the crystal structures that can be used to distinguish different compounds in the diffraction data.

For a typical SR-PXD experiment, the powdered samples were packed in a borosilicate capillary (Ø = 0.5 mm) and sealed with glue or grease. The sample was rotated during data acquisition, and the exposure time were typically 10-30 seconds. The variable temperatures were achieved using a cryostream or heat blower in the temperature range RT to 500 °C. The temperatures were

calibrated using a NaCl standard.[141,142] SR-PXD data were collected from the Diamond Light Source and the Swiss Light Source.

Powder Neutron Diffraction. Powder neutron diffraction (PND) is complimentary to PXD studies. The coherent scattering length of neutron are significantly different as compared to X-rays. The neutrons interact with the nucleus of an element, but changes in a much more random fashion with atomic number. Thus, neighboring elements in the periodic table can have significantly different scatterings lengths (Figure 2.3). Additionally, as the neutron is scattered by the nucleus, the scattering length is dependent on the isotope, and may differ significantly. For example, the incoherent scattering length of natural hydrogen is 25.27 fm and its coherent scattering length is -3.74 fm, while its isotope – deuterium has incoherent scattering length of 4.04 fm and coherent scattering length of 6.67 fm.[143] The incoherent scattering may affect the background in the diffractogram causing high signal-to-noise ratio, and this can be resolved by substitution of hydrogen by deuterium. By isotope enrichment of some compounds and thus changing the contrast, the desired information *e.g.* hydrogen (deuterium) positions, from the sample can be extracted. This makes PND a valuable complementary tool for PXD for determination of the positions of atoms 'visible' to neutrons.

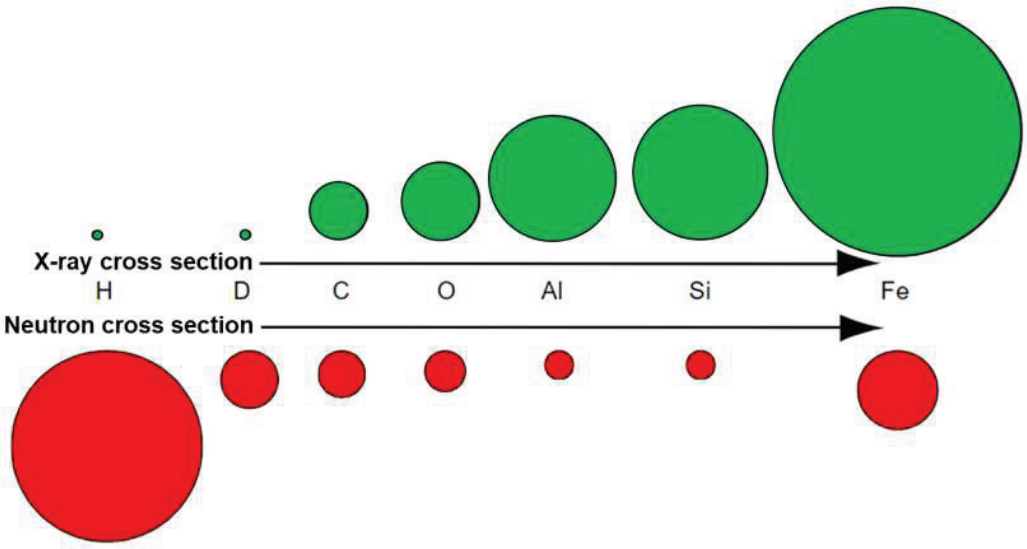

Figure 2.3. X-ray and neutron scattering cross sections. X-ray cross section is proportional to the atomic number, while the cross section of neutron is randomly dependent on the elements and their isotopes. Figure adapted from ref.[144]

Phase identification and Rietveld refinement. The positions and relative intensities of the Bragg peaks are unique for a crystalline phase. Phase identification were performed using the ICSD,[145] by search-matches with the PDF-4 database[146] and by the EVA software (only for PXD data). When the phase could not be identified, the unit cell were indexed in the software Free objects for crystallography (FOX).[147,148] The space group symmetry can be determined from a careful analysis of systematic extinctions of the Bragg peaks. Structural solution can be performed in FOX and used as a starting model for Rietveld refinements.

Rietveld refinements is used for structural refinement by fitting the entire calculated profile from the model to the experimental data using a least-squares approach. This allows for extraction of unit cell parameters, refinement of the atomic positions, occupancy refinements, quantitative phase analysis, obtain information on displacement parameters, and the profile can be refined to extract microstructural information.[149] In this dissertation, Rietveld refinements were performed on SR-PXD data for the mixed cation $Mg_{1-x}Mn_x(NH_3)_6Cl_2$ and $Mg_{1-x}Ni_x(NH_3)_6Cl_2$ solid solutions using the software TOPAS.[150,151]

Xpress beamtime for powder neutron diffraction studies of the deuterated mixed cation $Mg_{1-x}Mn_x(ND_3)_6Cl_2$ and $Mg_{1-x}Ni_x(ND_3)_6Cl_2$, (x = 0.1) ammines was granted by the ISIS neutron and muon source, and the investigation of hydrogen positions and the ammonia dynamics in the compounds was planned. However, the experiments have been postponed to an indefinite date, due to the temporary shutdown of the facility amid Covid-19 outbreak in Spring 2020.

2.3.2 Small-Angle Neutron Scattering

Small Angle Neutron Scattering (SANS) is a technique that is used to study the microstructure and nanostructure (radius, shape, volume, fractal dimension, mass, etc.) of materials on length scales from ~10 Å to ~1000 Å.[152] For particle or pore systems, SANS allows to perform structural characterization of the material through the determination of the form factor ($P(q)$) and structure factor ($S(q)$). When the neutrons are scattered by the sample, scattering arise from both interference from scattering entities (“scatterers”), which belong to the same object, and interferences from scatterers belonging to different objects within a sample.[153] A visual interpretation of the interactions between different elements of the medium is shown in Figure 2.4.

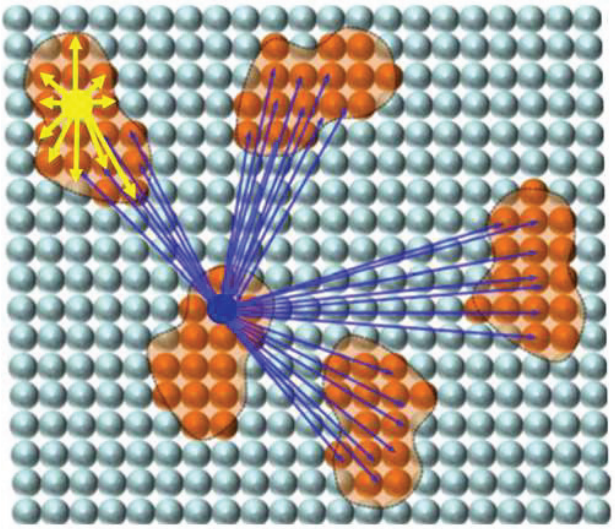

Figure 2.4. Interpretation of the form factor $P(q)$ and structure factor $S(q)$. $P(q)$ describes interactions between elementary scatterers (yellow arrows) within the same object while $S(q)$ elucidates interactions of elementary scatterers belonging to different objects within the investigated area (blue arrows). Figure adapted from ref.[153]

Generally, SANS data is described on a q-scale, where only the alterations of scattering length of the order of q^{-1} are inquired in a given range of q.[152] This range can qualitatively be separated into regions which give different information about the same sample. In the high q-range (around $q >$ 0.1 Å^{-1}), information about the size and shape of the smallest structures (or pores) can be extracted. In the low q-range ($q <$ 0.01 Å^{-1}), information about the organization of particles on larger length scales, as well as dimensions of particle clusters, can be obtained. The whole SANS pattern, including the intermediate q-range, can sometimes be used to model the experimental data with a specific structural model.[154]

The preliminary results from SANS studies on microstructural changes in $SrCl_2$ and $SrCl_2$-ENG composite materials during NH_3 absorption and desorption are briefly discussed in this dissertation. The detailed investigation is in progress and the full analysis will be described in more detail in future publications. The data were obtained using the instrument vSANS[155] at the National Institute of Standards and Technology (NIST), USA and LARMOR[156] at the ISIS neutron and muon source, UK.

2.3.3 Neutron Imaging

Neutron imaging is a technique that probes the structure of materials on a typical size range from few μm to several cm. It is complimentary to X-ray imaging with the advantage of high penetration power into the bulk of the material.[157] Neutron imaging primarily consists of neutron radiography and neutron tomography, where two-dimensional (2D) and three-dimensional (3D) information from the investigated sample can be extracted, respectively.

Neutron radiography. For a neutron radiography (NR) experiment, the sample is placed in a neutron beam with an incident intensity that interacts with the object and changes its intensity behind that object. This interaction is described by the interaction of the neutrons with the nuclei of the atoms that are present in the object. In this process, a part of the neutron beam is transmitted through and some are absorbed by the object. A distribution of attenuation coefficient within the object reduces the intensity of neutrons when it goes through the object. This information is detected by a detector array, recording 2D images, which is a projection of the object on the detector plane. The recorded beam on the detector is the result of conversion of the neutrons into visible light by scintillator which is then captured by a camera. Different elements within the object have different attenuation behavior, and the neutrons going through the object carry information of the object composition following the Beer-Lambert law:

$$I = I_0 \, e^{-\mu x} \tag{2.3}$$

where I is the transmitted or scattered intensity, I_0 is the incident intensity, μ is the attenuation coefficient and x is the thickness of the object. The attenuation coefficient represents how much each element is attenuating the neutron beam: the darker the image is, the more the object is attenuating. While various detector systems are employed in NR (combination of film and neutron-sensitive converter foil, neutron sensitive imaging plates, etc.), the digital imaging detectors (combination of scintillator and CCD or CMOS cameras) have been the key factor for development of the neutron imaging instruments nowadays. The conventional scintillators include crystalline ^{6}LiF/ZnS, which are widely used for neutron imaging applications, however GADOX (gadoliniumoxisulfate) scintillators, previously used only for X-ray imaging, have also been recently exploited for neutron imaging.[158] The thickness of the scintillator is fundamental in

achieving a high resolution and efficiency which are determined by the neutron capture probability and high light output of the scintillator.[159]

The instrumentation for neutron radiography and tomography requires a specific geometry (Figure 2.5), where a well-collimated beam, *i.e.* with low divergence, is important in order to obtain high spatial resolution. Generally, neutrons are collimated by slits, apertures, or collimation systems in order to reduce the range of directions in which the radiation moves and thus, get sharp images. The investigated sample is placed on a sample stage, allowing translational movement in *x*, *y* and *z* directions. The distance between the source and the sample (*L*) is also very important since the ratio between *L* and the pinhole diameter *D* influences the incident divergence. This determines the blur *d* on the detector.

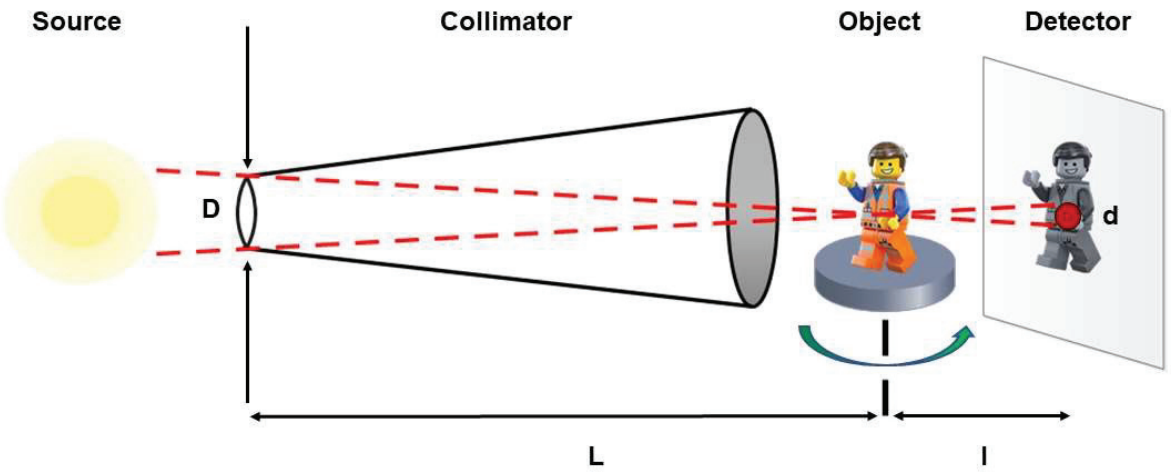

Figure 2.5. Typical geometry of a neutron imaging instrument.

Thus, a higher *L/D* ratio results in higher resolution, that can be adjusted by either increasing the source-to-sample distance (*L*) or decreasing pinhole diameter (*D*). However, increasing the distance (*L*) can be challenging due to the need for large space, and reducing the pinhole diameter (*D*) may result in reduced neutron flux. The distance between the sample and the detector (*l*) can be decreased which can also help in achieving high resolution image. The captured radiography images are then processed and saved in a computer for further data analysis.

Image analysis. For image analysis, the obtained images are normalized by open beam images, *i.e.* the images of the incident beam I_0 taken with no sample following the operation:

$$p = \frac{r - r_{DC}}{r_{OB} - r_{DC}} \quad (2.4)$$

where p is the normalized projection, r is the radiography image of an object, r_{DC} is the dark current image (no beam), r_{OB} is the open beam image or measured I_0. This normalization of the obtained radiography images removes the detector bias and neutron beam intensity fluctuations during neutron imaging experiments.

Both qualitative and quantitative analysis can be performed on the normalized neutron radiography images. Qualitative data analysis includes the visual characteristic properties of the objects, where the presence of pores, cracks or physical changes during *in-situ* studies can be observed. Quantitative image analysis allows us to calculate the precise amount of elements or materials within an investigated object, *i.e.* the thickness of the specific element can be calculated based on its neutron attenuation coefficient (Eq. 2.3). Thus, significant different neutron attenuation coefficients give a good contrast between the elements in the sample. However, incoherent neutron scattering can add errors to the data during image analysis. This can be a problem for hydrogen-containing compounds, due to the high incoherent scattering cross section of H (80 barns = $8 \cdot 10^{-23}$ cm^2).[143] As a result, beam hardening effects can take place which makes transmission values behind the sample to appear higher than the real value. This results in an underestimated thickness of the volume occupied by the incoherent scattering element.[160]

NR has some disadvantages due to the data acquisition in 2-dimensions only. The detected signal from radiogram (spots, agglomeration of specific material, etc.) can be local or spread over the investigated sample volume, and the depth cannot be observed by only neutron radiography studies. To obtain the 3-dimensional volume information, neutron tomography needs to be performed.

Neutron tomography is utilized as an indirect method to obtain 3D images, where several neutron radiography images are combined and reconstructed to acquire volume information. The 3D image of an object is achieved by its rotation from 0° to 360° during irradiation and data acquisition. Through careful analysis of the reconstructed 3D image, information about the inner structure (pores, cracks, impurities, etc.) can be extracted. The possibility of viewing the object through orthogonal XY-, XZ- and YZ-planes allows to discover obscured information, which is not possible to get with neutron radiography.

Neutron radiography and tomography studies on a specially designed THS reactor prototype (Figure 2.6) with the $SrCl_2$ and $SrCl_2$-ENG samples were analyzed at two different beamlines. The first neutron imaging experiments on THS reactor prototype with the $SrCl_2$ were conducted at NECTAR beamline[161] using thermal neutron flux with a mean energy of 28 meV at FRM-II Heinz-Maier Leibnitz Institute, Germany. ZnS/^{6}LiF scintillator screen combined with a CCD camera (Andor iKon-L-BV) was used and the collimation ratio of L/D = 230 was employed.

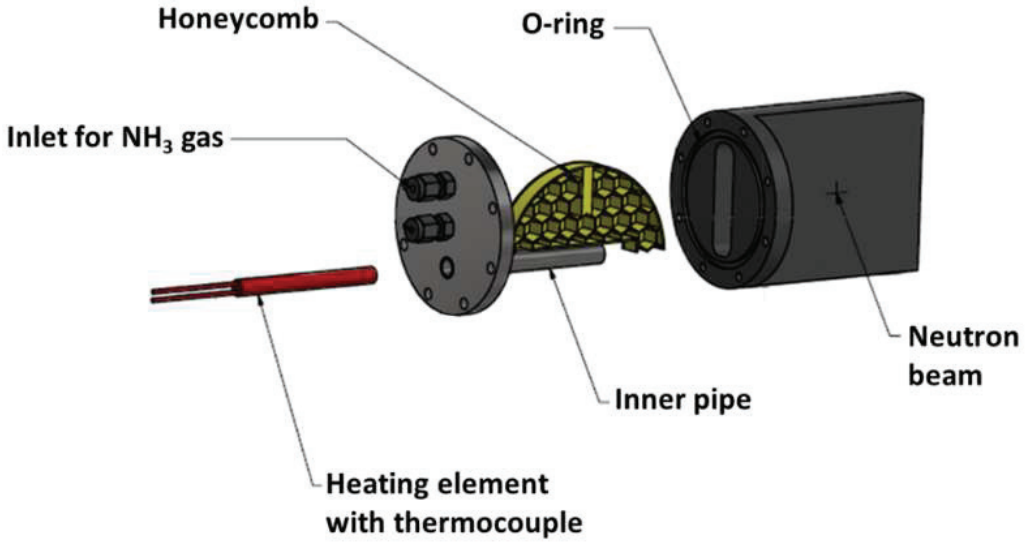

Figure 2.6. Schematic view of the THS reactor prototype used for neutron imaging experiments. Figure from ref.[162]

The resolution of 200 μm provided high quality neutron radiography data, which was utilized for *in-situ* NH_3 sorption studies of the THS reactor prototype. Furthermore, subsequent qualitative analysis of the investigated sorption processes was performed.

The second neutron imaging experiments on THS reactor prototype with the $SrCl_2$-ENG composite material was performed using a cold neutron beam (λ = 2.8 Å) at the NeXT instrument at the D50 beamline,[163] Institute Laue-Langevin, France. The cold neutrons with the flux of $1.5 \cdot 10^8$ n/cm^2/s were collimated to a 23 mm pinhole (L/D ~ 330) and detected using a Gadox scintillator screen with a field of view of 10 cm x 10 cm and a given thickness of 50 μm (Figure 2.7). The scintillated light was captured by a CMOS camera (Hamamatsu Orca 4V2) providing images with a time resolution of 1 s. Both neutron radiography and tomography experiments were conducted and

quantitative image analysis was performed, where the NH_3 spatio-temporal concentration in the $Sr(NH_3)_8Cl_2$-ENG composite was calculated (Section 3.2).

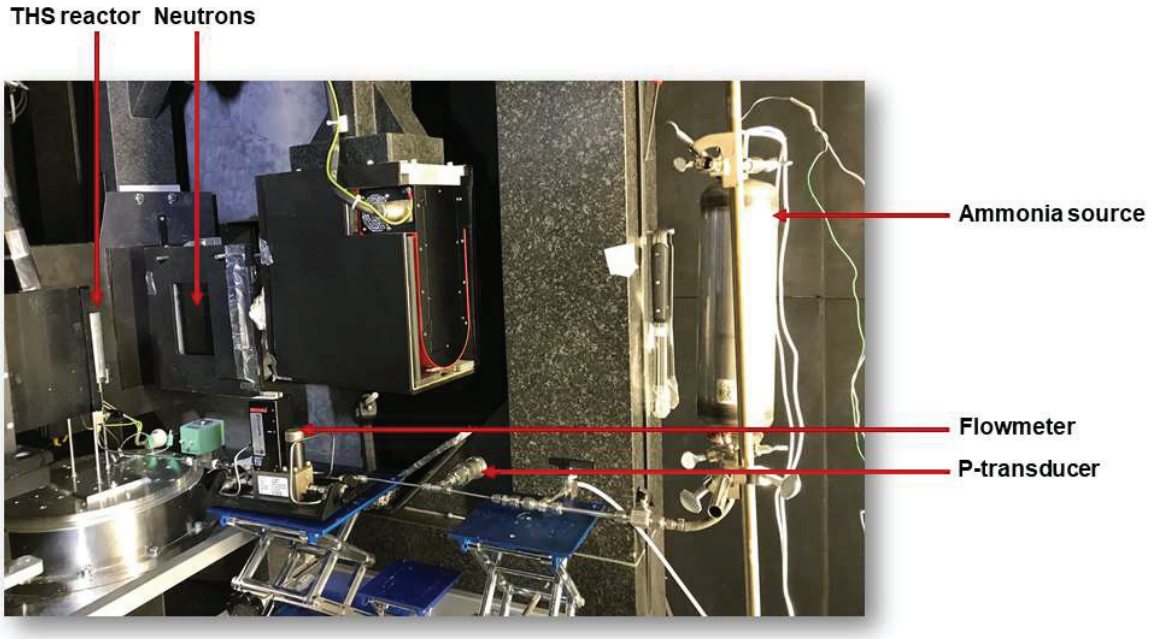

Figure 2.7. The experimental setup for the neutron imaging experiments with NeXT.

The obtained data from neutron radiography and tomography experiments was treated using image analysis and 3D image reconstruction software, including ImageJ,[164,165] XAct,[166] MuhRec,[167] TomViz[168] and VG Studio MAX.[169]

Chapter 3. Primary Results

This chapter describes the main results achieved during the PhD-project. Section 3.1 presents the *in-situ* neutron imaging study of the $SrCl_2/Sr(NH_3)_8Cl_2$ system within a THS reactor prototype and gives a comparison of the obtained neutron imaging results with numerical modelling. This is associated with Publication I and II. Section 3.2 describes the *in-situ* neutron imaging study of the $SrCl_2/Sr(NH_3)_8Cl_2$-ENG composite materials within the upgraded THS reactor prototype described in Publication III. Furthermore, spatio-temporal NH_3 concentration in the composite material during cycling is discussed, and the results are compared to the findings in Publication I. Section 3.3 shows preliminary results of the microstructural analysis of the $SrCl_2/Sr(NH_3)_8Cl_2$-ENG composite during ammonia cycling as investigated by small-angle neutron scattering. Section 3.4 describes the latest *in-situ* neutron imaging investigation on the upgraded THS reactor prototype, based on the findings in Publications I-III. Both Section 3.3 and Section 3.4 presents unpublished results, which will be described in more detail in forthcoming publications. Section 3.5 presents the investigation of ammonia storage properties of the mixed cation $Mg_{1-x}Mn_x(NH_3)_6Cl_2$ and $Mg_{1-x}Ni_x(NH_3)_6Cl_2$. Publication IV contains the detailed study on the $Mg_{1-x}Mn_x(NH_3)_6Cl_2$ compounds, while the results from the $Mg_{1-x}Ni_x(NH_3)_6Cl_2$ study form part of a manuscript in preparation.

3.1 *In-situ* Neutron Imaging Study of the $SrCl_2/Sr(NH_3)_8Cl_2$ System

This section provides an overview of important findings from the investigation of the $SrCl_2/Sr(NH_3)_8Cl_2$ system using neutron imaging, which is the main focus of this dissertation. Neutron imaging is a technique that can provide 2D or 3D images of the inner structures of bulk objects, that may not be obtainable by other techniques, and thus making it a unique tool for various studies in materials science.[159,170–172] The nondestructive neutron probe is advantageous over X-rays and has been widely used for archaeological and biological materials.[173–176] The particular strong interaction with hydrogen has resulted in significant interest of utilizing neutron imaging for research fields like hydrogen storage materials and hydrogen-containing systems.[177–181] Energy conversion devices such as fuel cells have also been widely investigated by neutron imaging studies.[182–186]

Interaction of neutrons with hydrogen has been a key element for our studies, where homogeneous ab/desorption of NH_3 in $SrCl_2/Sr(NH_3)_8Cl_2$ is a prerequisite. **Publication I** describes the results from the very first application of neutron imaging for investigating the NH_3-distribution in materials for thermochemical heat storage systems. A specially designed THS reactor prototype was prepared for the experiments. It contained $SrCl_2$ powder embedded in a stainless-steel honeycomb scaffold. The THS reactor prototype is illustrated in Figure 3.1, showing the honeycomb, the cells where the $SrCl_2$ powder was placed and the heating element.

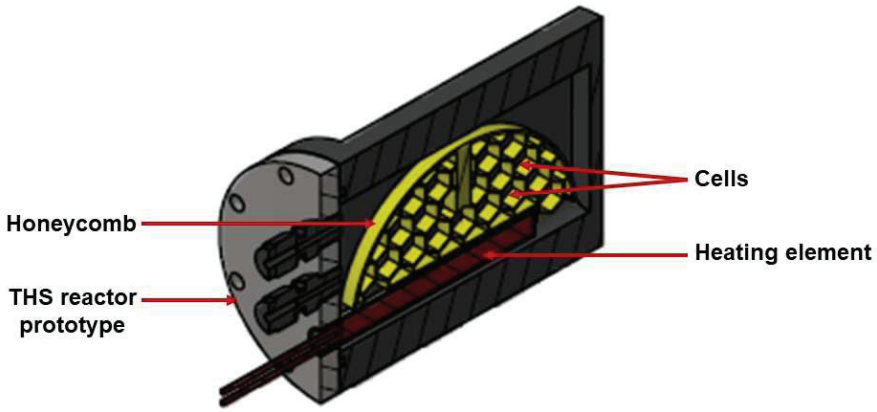

Figure 3.1. Schematic representation of the THS reactor prototype and its main components.

The formation of $Sr(NH_3)_xCl_2$ (x = 0-8) during NH_3 cycling was studied by *in-situ* neutron radiography, where the high neutron attenuation coefficient of H easily revealed the location of NH_3 in the sample. Thus, NH_3 is visible in neutron radiograms as dark areas (see Figure 3.2).

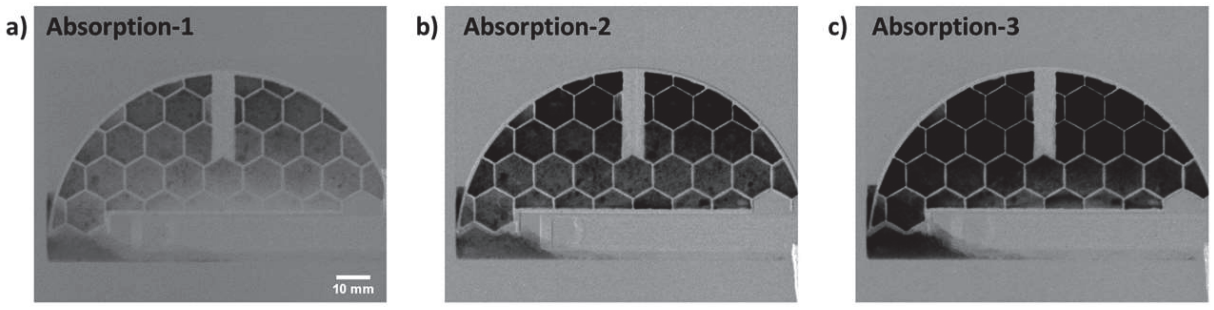

Figure 3.2. A series of normalized neutron radiography images representing the formation of $Sr(NH_3)_xCl_2$ (dark areas for increasing x) after each absorption process. a) absorption-1, b) absorption-2 and c) absorption-3. The figure is taken from Publication I.[162]

Each absorption was followed by a desorption process at selected temperatures. The difference in saturation degree of NH_3 (x) in $Sr(NH_3)_xCl_2$ after each absorption was found to be a result of the volume expansion and formation of micropores after the first cycle. The evolution of micropores provided paths for more NH_3 to diffuse into the powder beds in the subsequent cycles. Thus, the NH_3 saturation degree increased significantly in the first three absorption steps, and is observed as darker areas in Figure 3.2. This was further investigated by qualitative analysis of the neutron radiography images by determination of the change in the neutron transmission $I(\lambda)$ over the sample during each cycle. This is described in more detail in Publication I.

$Sr(NH_3)_8Cl_2$ formation is followed by a severe volume expansion during the first and subsequent cycles. In the fourth absorption cycle the volume expansion was up to 10 % during $Sr(NH_3)_xCl_2$ formation, and mainly observed in the axial direction perpendicular to the honeycomb plane. This observation was achieved by placing the THS reactor prototype so that the powder expansion direction is perpendicular to the neutron beam direction. During ammonia absorption, the powder particles increased in volume, but limited to axial expansion, as the radial expansion was prevented by the cell walls. It can also be noted in Figure 3.2 that there was some amount of $SrCl_2/Sr(NH_3)_xCl_2$ outside of the honeycomb. One side of the honeycomb was open for free $SrCl_2$ and NH_3 interaction, and the powder fell off the honeycomb during mounting of the THS reactor. Besides, the significant powder expansion also contributed to the displacement of some powder from the cells.

The stainless-steel honeycomb was utilized in this study in order to provide a homogeneous heat distribution over the whole area of the powder bed during the NH_3 desorption. However, *in-situ* neutron radiography studies revealed an inhomogeneous NH_3 release from $Sr(NH_3)_xCl_2$ due to a non-uniform heat distribution. Careful investigation of the NH_3 desorption showed that the direction of the heat was from the heating element toward the top of the honeycomb, and not from the walls of each cell of the honeycomb as expected (this is schematically shown in later section 3.4). Thus, the thermal conductivity of stainless steel was found to be too low for this application.

Complementary neutron tomography studies were performed on the THS reactor prototype with different saturation states of the $SrCl_2/Sr(NH_3)_8Cl_2$ powder. In-depth analysis of the reconstructed 3D images of the THS reactor prototype and different orthogonal planes provided very important

information. A distortion of the honeycomb back plate was discovered (see Figure 3.3), likely caused by the powder expansion, and therefore resulting in mechanical stress on the honeycomb.

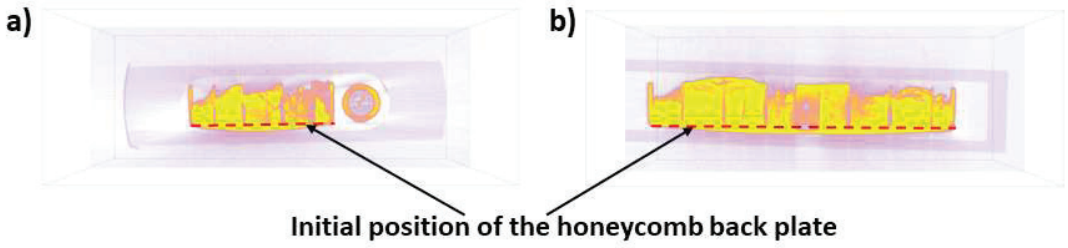

Figure 3.3. Orthogonal views of the 3D image of the honeycomb a) XY-plane and b) YZ-planes showing the irregularity of the powder thickness over the honeycomb area and the deformation of the honeycomb back plate due to $Sr(NH_3)_8Cl_2$ formation followed by the volume expansion. The red dashed lines represent the position of the back plate before the absorption process. The figure is adapted from Publication I.[162]

The back plate was only welded to the honeycomb net along the outer edges and is therefore vulnerable to the mechanical stress resulting from the significant volume expansion of the powder. This observation was crucial for the optimization of the THS reactor design, since the mechanical stability of the honeycomb is required for safe and efficient operation.

The neutron radiography results discussed in **Publication I** are compared with numerical simulations in **Publication II**. The modelling for the heat storage reactor was performed using the software COMSOL Multiphysics® using the integrated thermochemistry, to model the ammonia flow and the heat transfer for optimization of the final reactor design. The reaction advancement was also investigated, where the saturation of NH_3 was studied and the numerical values of the absorbed or desorbed NH_3 were obtained during the ab- and desorption cycles. The comparison of the experimental (from neutron radiography) and the numerical data (from modelling) showed a good agreement in case of both absorption and desorption processes in the $SrCl_2/Sr(NH_3)_8Cl_2$ system. However, the powder thickness in the honeycomb was slightly different during the neutron imaging experiment, as compared to the fixed thickness during the modelling. As discussed above, during the neutron imaging experiment, the loose powder and the significant powder volume expansion, gave an uneven distribution of powder thickness over the honeycomb. In turn, this

resulted in slight discrepancies between the experimental and modelling data, which is discussed in more details in Publication II. Comparison to the numerical calculations showed the possibility of verifying a numerical model of a THS reactor by using neutron radiography data, demonstrated for the first time.

Based on the results discussed in Publications I and II, several issues in the THS reactor prototype were observed:

- Loose powder
- Mechanical instability of the honeycomb
- Poor heat conductivity of the stainless-steel honeycomb

These issues were the motivation for improvements in the THS reactor prototype and the experimental setup. The upgrade of the setup and the improvement of the sample and the subsequent study with neutron imaging is presented in the following Section 3.2, which also describes the main results from **Publication III**.

3.2 $SrCl_2$-ENG Composite Material with Enhanced Kinetics

As described in Section 3.1, the uptake and release of NH_3 in $SrCl_2/Sr(NH_3)_8Cl_2$ system undergoes severe volume expansion, providing mechanical stress to the THS system. This undesired behavior of metal halide ammines can limit their potential in applications where safe operation is a prerequisite. Thus, the $SrCl_2$ powder was mixed with expanded natural graphite (ENG). The porous nature of ENG reduces the effect of the volume expansion, as the powder can freely expand and contract in the ENG matrix without applying a mechanical stress to the THS system. The method of ENG impregnation with salts was previously applied to various systems, resulting in enhanced sorption reactions kinetics and thermal conductivity of the materials.[66,187–193] It has been reported that the thermal conductivity of the $SrCl_2$-ENG composite can be increased by up to 182 % as compared to $SrCl_2$.[189] The diffusion path of the NH_3 gas into the bulk of the salt can be reduced due to the high porosity of ENG, thus resulting in fast NH_3 diffusion. The matrix of ENG impregnated with the $SrCl_2$ salt was mounted in the stainless-steel honeycomb inside the THS reactor prototype and investigated by *in-situ* neutron imaging. The experimental setup was upgraded with a flowmeter and a temperature sensor, which allowed for monitoring of the NH_3 flow and the composite temperature during NH_3 cycling, respectively.

Publication III presents the results from neutron radiography and tomography experiments on $SrCl_2/Sr(NH_3)_8Cl_2$-ENG composite materials within the THS reactor, which was measured at the NeXT beamline at ILL, Grenoble, France. In the improved THS reactor, the honeycomb back plate and the net were welded together, thus improving the mechanical stability during the NH_3 cycling. The composite material was cut into solid pellets and placed inside the cells of the stainless-steel honeycomb. The obtained images showed the homogeneous ammonia absorption in the honeycomb and the slight expansion of the composite material. The absorption reaction was complete in about 2 hours, revealing higher absorption kinetics of the composite material, with respect to the pure salt. During desorption, the NH_3 release was inhomogeneous, and the desorption reaction went in one direction from the heating element to the top of the honeycomb (see Figure 3.4).

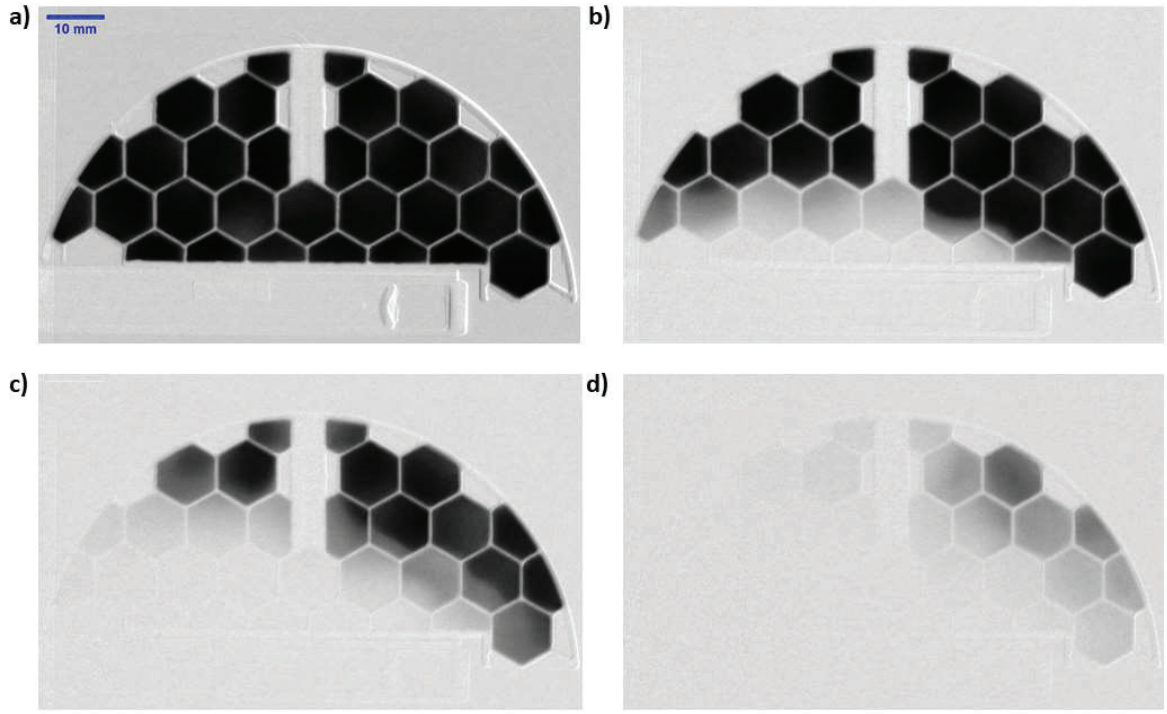

Figure 3.4. Normalized neutron radiography series showing the ammonia desorption from the $Sr(NH_3)_8Cl_2$-ENG composite at 200 °C after a) 0 min, b) 10 min, c) 20 min and d) 30 min.

While the $Sr(NH_3)_8Cl_2$-ENG composite showed improved kinetics, and the ENG contributed to a more efficient heat transfer within the composite material, the stainless steel honeycomb did not provide a uniform heat distribution over the honeycomb area during ammonia desorption. The heat

conductivity of the ENG is better than the stainless-steel. Hence, the honeycomb did not give a benefit during the NH_3 desorption processes. This is related to the poor heat conductivity of stainless-steel as described in Section 3.1.

The spatio-temporal NH_3 content in $Sr(NH_3)_8Cl_2$ was calculated using the Beer-Lambert law (Eq 2.3), and an NH_3 uptake of up to 45.7 wt% was achieved during the first cycle (theoretical gravimetric capacity is 46.2 wt%). The deviations in the NH_3 content in the different cells are due to deviations in the amount of powder ($SrCl_2$) over the honeycomb area. The following NH_3 desorption at 200 °C resulted in desorption of 7 moles of NH_3 and formation of $Sr(NH_3)_8Cl_2$ with an NH_3 content of 5.7 wt% (see Figure 3.5). While a homogeneous NH_3 absorption was observed, the NH_3 desorption rate in the cells of the honeycomb highly depends on their relative position and distance from the heating element. The cells closer to the heating element (cell 5 and 12) release NH_3 faster than the ones further away (cell 3 and 7), as the direction of the heat is from the lower left corner towards the top right corner, as seen in Figure 3.4.

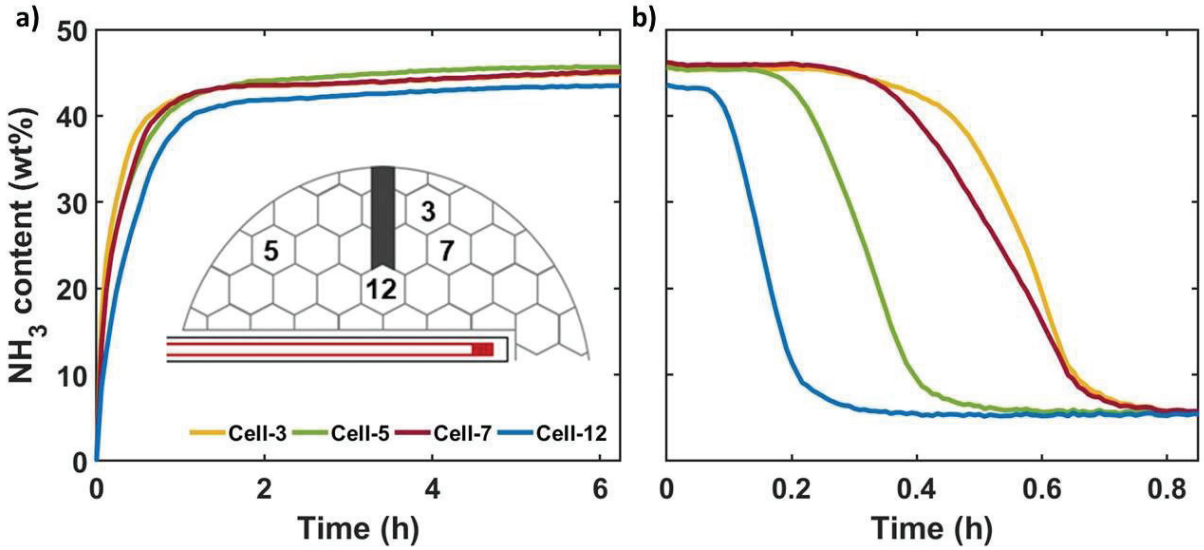

Figure 3.5. Spatio-temporal NH_3 concentration in selected cells of the honeycomb during a) absorption-1, when $Sr(NH_3)Cl_2$ is formed and b) desorption-1 when 7 NH_3 equivalents are released from the composite, resulting in the formation of $Sr(NH_3)Cl_2$ at 200 °C. The figure is adapted from Publication III.

Moreover, the temperature of the composite material was measured during NH_3 cycling. The thermocouple was inserted into the stainless-steel housing on the top of the honeycomb. The

temperature increased up to 55 °C during the exothermic absorption process, illustrating that the composite material meets the requirements of a THS system for low-temperature applications.

In the $SrCl_2$-ENG composite, the ENG mainly served as a buffer allowing the $SrCl_2$ powder to freely expand in the porous matrix during the ammonia uptake and formation of $Sr(NH_3)_8Cl_2$, providing mechanical stability for the material during the ammonia cycling. This was confirmed by complementary neutron tomography studies of the composite material at its initial state $SrCl_2$-ENG (a) and after NH_3 cycling and formation of $Sr(NH_3)Cl_2$ (see Figure 3.6).

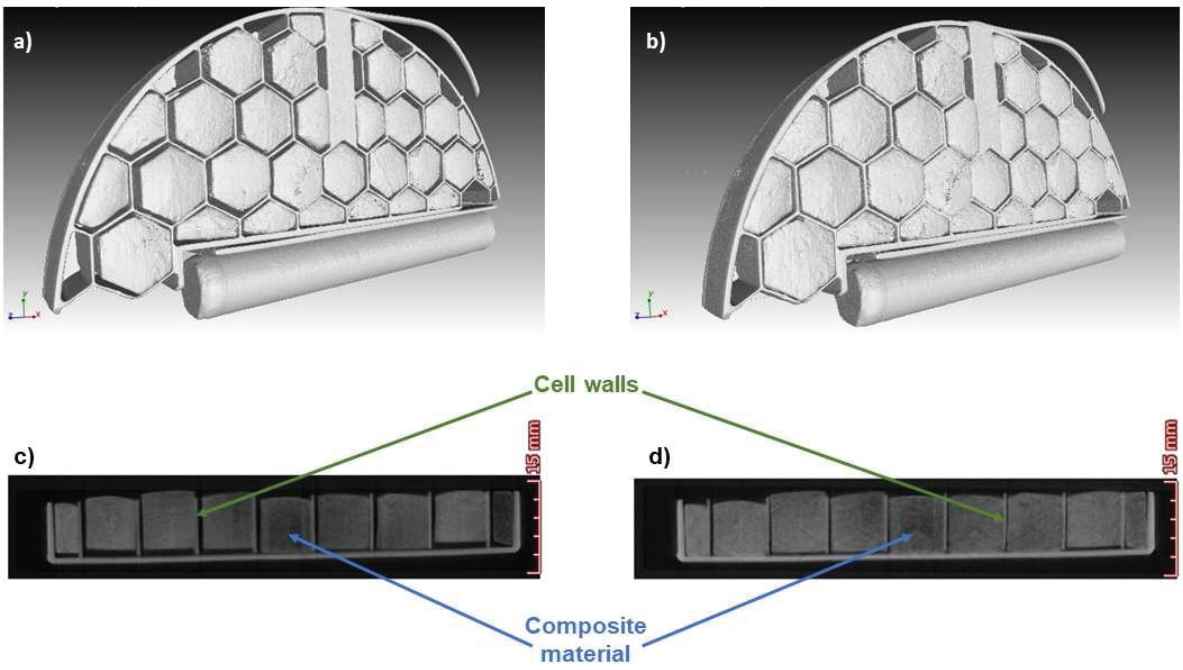

Figure 3.6. Top: 3D visualization of the honeycomb at the a) initial state ($SrCl_2$-ENG) and b) the desorbed state ($Sr(NH_3)Cl_2$-ENG). Bottom: The view of the honeycomb in XZ-plane after 3D reconstruction, showing the change in the composite material before and after NH_3 cycling: c) $SrCl_2$-ENG and d) $Sr(NH_3)Cl_2$-ENG.

This work shows that the new $SrCl_2$-ENG composite material gives an improvement of the THS system due to a better mechanical stability and improved kinetics. However, poor heat conductivity of the stainless-steel honeycomb during NH_3 release still represents a limiting factor. The volume expansion maintained by the ENG matrix was crucial to reduce the mechanical stress on the honeycomb. During the experiment it was possible to acquire additional data on the sample

temperature and NH_3 flow to/from the cell. However, the behavior of $SrCl_2$ within the ENG matrix with respect to pore formation and $SrCl_2$ particle size changes during NH_3 cycling remains unknown. An investigation of micro- and nano-structure formations in the $SrCl_2$-ENG composite upon NH_3 sorption would provide a better understanding of the system. This can be achieved by using SANS as discussed in the following Section 3.3.

3.3 Microstructural Evolution in the $SrCl_2$-ENG During NH_3 Cycling

This section provides a brief overview of the microstructural evolution within the $SrCl_2$-ENG composite as observed by SANS. The results presented in this section were obtained on the vSANS (very small-angle neutron scattering) instrument at NIST, USA with a Q-range of 0.02 nm^{-1} to 1.5 nm^{-1}. Only preliminary studies of the SANS data are presented here, and a detailed investigation is still in progress.

SANS is a valuable technique, extensively used both in the fields of soft and hard condensed matter.[194–197] This technique is widely applied also for the investigation of energy storage materials, *e.g.* batteries, which undergo microstructural changes during charging and discharging.[198–203] Investigations with SANS of nanoscale structural features and the following changes occurring in a material due to different handling and processing methods, as well as resulting from changes occurring *in-situ*, can provide information about the bulk particle structure.[204] Here SANS experiments were performed in order to investigate *in-situ* nanoscale changes during NH_3 sorption processes in the $SrCl_2$-ENG composite, revealing information on the spatial evolution of the powder inside the matrix, as well as the salt morphology.

The SANS profiles of $SrCl_2$ in the initial (with no ammonia) and desorbed states (before absorption) are shown in Figure 3.7 (a). The profiles vary between each state, in particular between the initial state and the two subsequent desorbed states, after which the profiles are more similar (2 and 3). These observations agree well with the ‘activation’ of $SrCl_2$ in the initial cycles and formation of micropores that allow more NH_3 to be ab-/desorbed in the following cycles, see Sections 3.1 and 3.2.

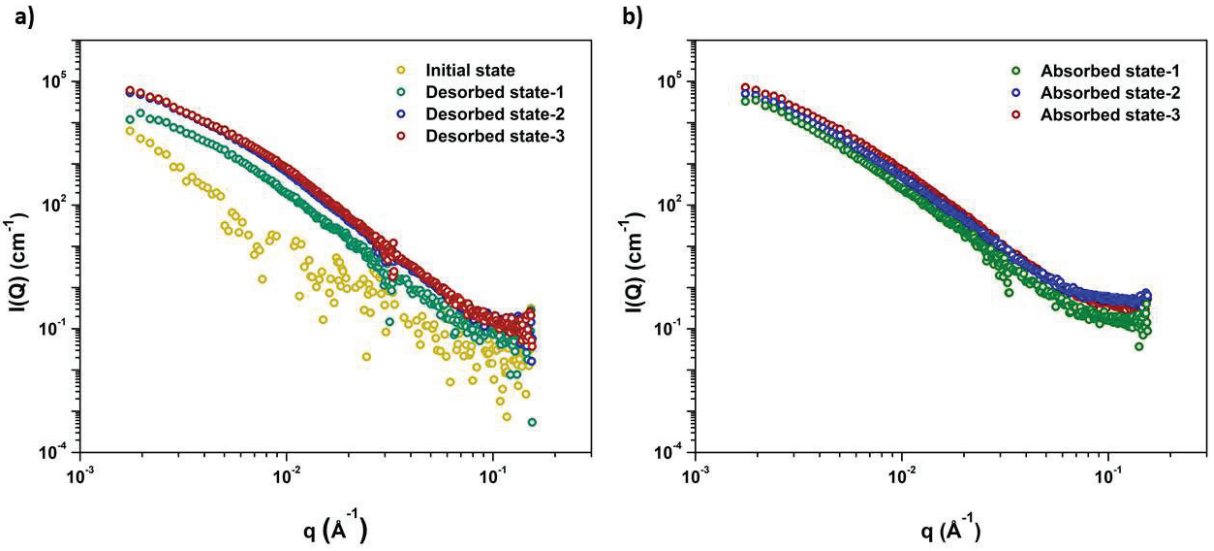

Figure 3.7. SANS data from the powder sample for a) the desorbed states ($Sr(NH_3)Cl_2$), and b) the absorbed states ($Sr(NH_3)_8Cl_2$). In the initial state the sample has no ammonia. The desorbed state 1, 2 and 3 were obtained after heating the sample at the temperatures 64, 64 and 150 °C, respectively. The absorbed state 1, 2 and 3 were obtained at NH_3 gas pressures of 2.4, 2.9 and 1.9 bar, respectively.

There was no resolvable plateau in the signal from the initial state (yellow) that would correspond to specific particle sizes. Instead, the linearity of the scattering curve indicates a broad distribution of particle sizes. In contrast, after the first NH_3 cycle, the signal from the sample in the desorbed state-1 (green) shows a deviation from linearity in the range of $q = 2 \cdot 10^{-3}$ Å^{-1} to $5 \cdot 10^{-2}$ Å^{-1} compared to the initial state. This demonstrates a change in the size and shape of the particles. The desorption was conducted at 64 °C (*i.e.* only 7 moles of NH_3 are desorbed), and therefore the profile shows the contribution from $Sr(NH_3)Cl_2$. A further change in the profile is observed after one more NH_3 cycle (blue), the desorption being conducted at the same temperature of 64 °C. This signal from $Sr(NH_3)Cl_2$ demonstrates that the nanostructure of the powder particles is still evolving after two cycles. However, after the third cycle (T = 150 °C) the profile stabilizes (red).

Figure 3.7. (b) presents the SANS profile of $Sr(NH_3)_8Cl_2$ after absorption-1 (green), 2 (blue) and 3 (red). The significant amount of hydrogen in $Sr(NH_3)_8Cl_2$ resulted in an increase of the background up to 0.5 cm^{-1}, one order of magnitude higher compared to the SANS signal from the powder particles in the initial and desorbed states ($I(Q)$ ~0.05 cm^{-1}). This increase in the

background is due to the large incoherent neutron scattering cross-section of hydrogen. The signal from $Sr(NH_3)_8Cl_2$ in all cycles is similar, with only a small difference. This may be caused by an increase of the amount of absorbed NH_3 which is consistent with the increase in the background with every cycle. The background signal in absorbed state-2 is relatively higher than that for the other two absorbed states due to the higher amount of absorbed NH_3 achieved by applying an NH_3 pressure of 2.9 bar. The NH_3 pressure during absorption-1 and -3 was lower: 2.4 bar and 1.9 bar, respectively.

These preliminary investigations of the $SrCl_2$-ENG using the SANS technique illustrate the possibility of obtaining information about microscopic changes occurring in the composite material upon NH_3 cycling. Ongoing studies on the pore and particle size and shape will bring additional insight about the $SrCl_2/Sr(NH_3)_8Cl_2$ composite in the ENG matrix.

3.4 Upgrade of the THS Reactor

This section describes the improvements applied to the THS reactor prototype, based on findings described in Sections 3.1-3.3. An upgraded THS reactor prototype was tested and studied by *in-situ* neutron imaging. It contained an aluminum-honeycomb to improve the thermal conductivity, which was not satisfactory with the stainless-steel honeycomb. Both the $SrCl_2/Sr(NH_3)_8Cl_2$ and the $SrCl_2/Sr(NH_3)_8Cl_2$-ENG composite systems were investigated at the FRM-II research reactor in Germany using the NECTAR instrument. Complete data analysis is still in progress and will be analyzed and submitted for publication by the end of 2020.

Figure 3.7 depicts the series of neutron radiography images of the $Sr(NH_3)_xCl_2$ during the NH_3 release at 100 °C against 1 bar of NH_3. The fully absorbed $Sr(NH_3)_8Cl_2$ (Figure 3.8 a) starts desorbing NH_3 from each cell at the same time (Figure 3.8 b), and the desorption is independent on the distance from the heating element (located below the honeycomb), as the aluminum honeycomb allows the fast distribution of the heat. This effect can also be seen from the NH_3 desorption behavior within each cell (Figure 3.8 c), where the $Sr(NH_3)_8Cl_2$ powder close to the cell edges start releasing NH_3 simultaneously and persist until all 7 moles of NH_3 are desorbed (Figure 3.8 d) at 100 °C, demonstrating excellent efficiency of the honeycomb.

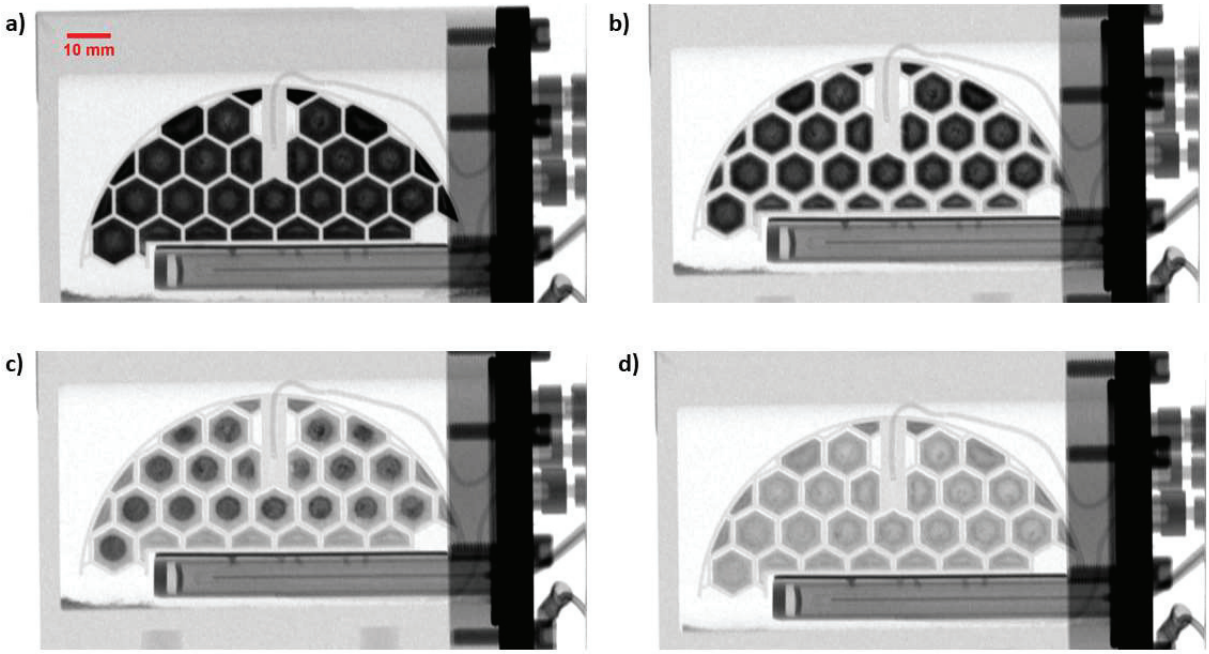

Figure 3.8. Neutron radiography images of $Sr(NH_3)_8Cl_2$ during desorption at 100 °C and 1 bar of NH_3 after a) 0 min, b) 20 min, c) 40 min and d) 1 hour from the start of the desorption process. The images are open beam normalized.

This preliminary analysis of the neutron imaging data shows the significant effect the honeycomb material can have for ensuring an efficient heat transfer.

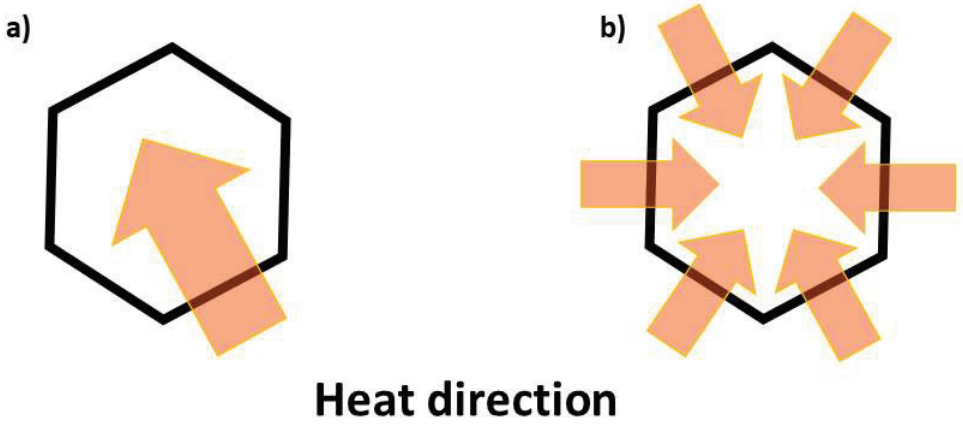

Figure 3.9. A schematic representation of the heat direction within each cell of the honeycomb depending on the material: a) stainless-steel and b) aluminum.

The effect of the stainless-steel *vs* aluminum honeycomb with regards to heat transfer within a single cell is illustrated in Figure 3.9. The heat direction is mainly one-directional (from and away the heating element) when stainless-steel is used, while the aluminum-made honeycomb provides a homogeneous heat distribution coming from each side of the cell. The efficiency of the THS reactor prototype highly depends on the efficiency of the individual components, and homogeneous absorption and desorption of NH_3 during THS reactor operation is a key element for an efficient THS system.

3.5 Tailoring the Properties of Metal Halide Ammines

There has been several studies on optimization of the NH_3 ab/desorption kinetics in metal halide ammines and tailoring of the NH_3 desorption temperature by formation of solid solutions.[70,94,96,161] This approach is used to tune the NH_3 storage capability of the metal halide ammines, where both cation and anion mixing result in intermediate properties of the final compounds.

$Mg_{1-x}Mn_x(NH_3)_6Cl_2$ (x = 0.025, 0.05, 0.1, 0.3 and 0.5) mixed metal halide ammines. In this section the study addressing the mixed cation $Mg_{1-x}Mn_x(NH_3)_6Cl_2$ and $Mg_{1-x}Ni_x(NH_3)_6Cl_2$ solid solutions is discussed. **Publication IV** reports the SR-PXD, TGA-DSC and volumetric studies with Sieverts apparatus on $Mg_{1-x}Mn_x(NH_3)_6Cl_2$ (x = 0.025, 0.05, 0.1, 0.3 and 0.5) mixed metal halide ammines with reversible NH_3 storage capacity in the temperature range 20-400 °C. Intermediate properties to that of the monometallic $Mg(NH_3)_6Cl_2$ and $Mn(NH_3)_6Cl_2$ metal halide ammines are observed.[205] SR-PXD data revealed that the mixed cation $Mg_{1-x}Mn_x(NH_3)_6Cl_2$ (x = 0.025, 0.05, 0.1, 0.3 and 0.5) solid solutions crystallize in a cubic unit cell with space group symmetry *Fm*-3*m*, isostructural to the precursor materials. *In-situ* SR-PXD data showed that the diammine and monoammine compounds were formed as intermediate phases and are also isostructural to the intermediate phases observed during ammonia desorption from $Mg(NH_3)_6Cl_2$ and $Mn(NH_3)_6Cl_2$.

Rietveld refinement of the SR-PXD data for the mixed metal hexammines revealed a unit cell volume increase with increasing of Mn content according to Vegard's law. The DSC study of the compounds using the Kissinger method revealed changes in the activation energies for each NH_3 desorption step in $Mg_{0.5}Mn_{0.5}(NH_3)_6Cl_2$ compared to $Mg(NH_3)_6Cl_2$ and $Mn(NH_3)_6Cl_2$. A change in the activation energy of the first 4 moles of NH_3 desorption from $Mg_{0.5}Mn_{0.5}(NH_3)_6Cl_2$ was observed (E_a = 54.8 kJ·mol^{-1}), compared to $Mg(NH_3)_6Cl_2$ (E_a = 60.8 kJ·mol^{-1}). This change might

be affected by the activation energy of the 4 moles of NH_3 from $Mn(NH_3)_6Cl_2$ (E_a = 43.5 kJ·mol^{-1}). However, the activation energies for the second and third NH_3 desorption steps were not significantly different from the monometallic compounds.

During *in-situ* SR-PXD of $Mg_{0.5}Mn_{0.5}(NH_3)_6Cl_2$, an intermediate compound was observed during the final NH_3 desorption from $Mg_{0.5}Mn_{0.5}(NH_3)Cl_2$ (Figure 3.10 (yellow diffraction pattern)). Similarly, an unidentified phase has also been reported for the NH_3 desorption from $Mn(NH_3)Cl_2$, which has been suggested to be a result of a non-stoichiometric NH_3 release from the monoammine during formation of $MnCl_2$.[206] Our *in-situ* SR-PXD results for $Mn(NH_3)_6Cl_2$ and $Mg_{0.5}Mn_{0.5}(NH_3)_6Cl_2$ suggest the formation of the hemiammines, $Mn(NH_3)_{0.5}Cl_2$ and $Mg_{0.5}Mn_{0.5}(NH_3)_{0.5}Cl_2$, respectively. However, a precise characterization of their crystal structures was not possible due to the short temperature range the phase was observed and the poor crystallinity of the compound. The complementary volumetric studies on $Mg_{0.5}Mn_{0.5}(NH_3)_6Cl_2$ confirmed a two-step process during the desorption of the final mole of NH_3 from $Mg_{0.5}Mn_{0.5}(NH_3)Cl_2$.

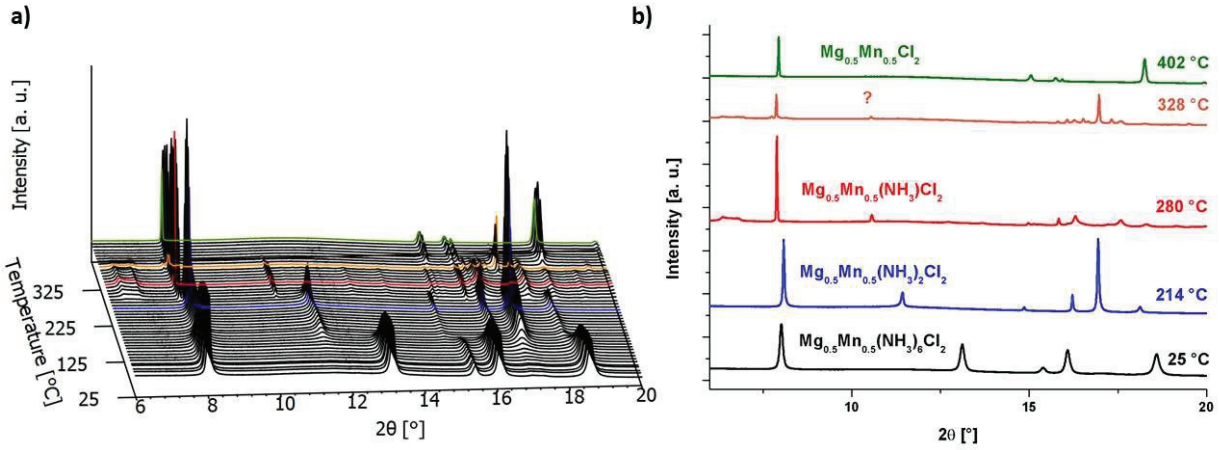

Figure 3.10. a) *In-situ* SR-PXD of $Mg_{0.5}Mn_{0.5}(NH_3)_6Cl_2$ measured from RT to 402 °C with a heating rate of 5 °C·min^{-1} and λ = 0.82646 Å, and b) SR-PXD patterns at selected temperatures. The figure is taken from Publication IV.[205]

After the full NH_3 desorption of $Mg_{1-x}Mn_x(NH_3)_6Cl_2$ solid solutions at T = 440 °C using TGA-DSC, the samples were examined using SR-PXD. The stability of the $Mg_{1-x}Mn_xCl_2$ solid solutions was confirmed by SR-PXD, showing the presence of only one phase, thus the solid solution does

not phase separate. Several NH_3 absorption and desorption cycles in a Sieverts apparatus confirmed the excellent cyclability of the mixed metal hexammines.

$Mg_{1-x}Ni_x(NH_3)_6Cl_2$ (x = 0.025, 0.05 and 0.1) mixed metal halide ammines. Solid solutions of $Mg_{1-x}Ni_x(NH_3)_6Cl_2$ have also been studied. Also in this case, the thermal properties were intermediate to those of $Mg(NH_3)_6Cl_2$ and $Ni(NH_3)_6Cl_2$. It was found that $Mg_{1-x}Ni_x(NH_3)_6Cl_2$ solid solutions crystallize in a cubic unit cell with space group symmetry *Fm*-3*m*, similar to the monometallic $Mg(NH_3)_6Cl_2$ and $Ni(NH_3)_6Cl_2$. The NH_3 desorption steps were studied by *in-situ* SR-PXD and TGA-DSC.

Figure 3.11. shows the DSC study on the monometallic $Mg(NH_3)_6Cl_2$ and $Ni(NH_3)_6Cl_2$ and the mixed cation $Mg_{1-x}Ni_x(NH_3)_6Cl_2$ hexammines, where three step NH_3-desorption processes are observed. For each step, *i.e.* the release of 4 NH_3, 1 NH_3 and 1 NH_3 equivalents, respectively, a change in the onset temperatures of the desorption is observed for the different solid solutions. $Ni(NH_3)_6Cl_2$ thermally releases ammonia in three steps: *i*) at 168 °C (4 moles of NH_3), *ii*) at 327 °C (1 mole of NH_3) and *iii*) at 396 °C (1 mole of NH_3), using a backpressure of 1 bar of ammonia (see Section 1.3). The NH_3 release temperatures of $Ni(NH_3)_6Cl_2$ is higher than the $Mg_{1-x}Ni_x(NH_3)_6Cl_2$ hexammines, due to the higher binding energy of Ni^{2+}-NH_3 as compared to Mg^{2+}-NH_3. For the solid solutions, the desorption temperature approaches that of $Ni(NH_3)_xCl_2$.

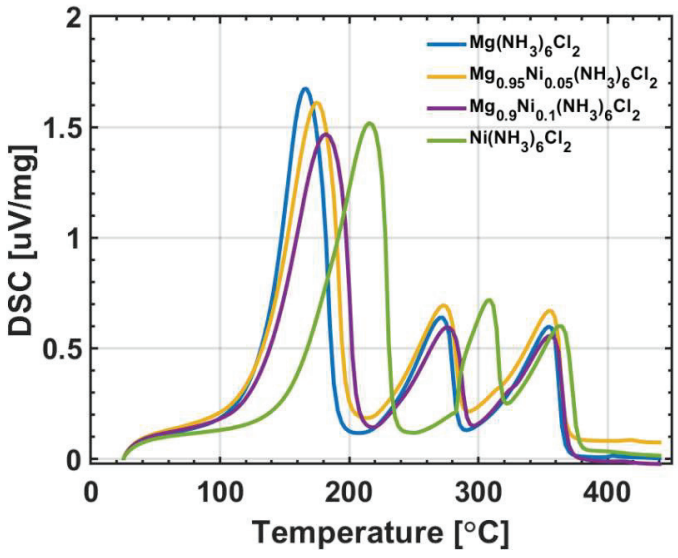

Figure 3.11. DSC study of the $Mg(NH_3)_6Cl_2$, $Ni(NH_3)_6Cl_2$ and $Mg_{1-x}Ni_x(NH_3)_6Cl_2$ (x = 0.05 and 0.1) mixed metal halide ammines.

The results on $Mg_{1-x}Ni_x(NH_3)_6Cl_2$ (x = 0.025, 0.05 and 0.1) mixed metal halide ammines are part of a manuscript in preparation. Further studies by PND are planned and Xpress beamtime was granted by ISIS neutron and muon source in the UK to provide more insight into the hydrogen positions and dynamics in the compounds using deuterated samples (ND_3). These dynamics may be linked to the kinetics of ammonia desorption of the mixed metal hexammines. However, the experiments were postponed due to the temporary shutdown of the facility amid the Covid-19 outbreak in Spring 2020.

In conclusion, $Mg(NH_3)_6Cl_2$, $Mn(NH_3)_6Cl_2$ and $Ni(NH_3)_6Cl_2$ have similar crystal structures, but different unit cell volumes in accordance with the different ionic radii of Mg^{2+}, Mn^{2+} and Ni^{2+}. The difference in charge densities of these metal ions result in different metal-NH_3 binding energies, and therefore the NH_3 desorption temperatures differ among the compounds. The similarity in the crystal structures inspired the study of these materials aiming to achieve their solid solution with tunable NH_3 storage properties. Due to the lower NH_3 release temperatures of $Mn(NH_3)_6Cl_2$ compared to $Mg(NH_3)_6Cl_2$, a decrease in NH_3 release temperatures of $Mg_{1-x}Mn_x(NH_3)_6Cl_2$ is observed. However, higher NH_3 release temperatures of $Ni(NH_3)_6Cl_2$ compared to $Mg(NH_3)_6Cl_2$ show the opposite trend, where the NH_3 release temperatures are increased in $Mg_{1-x}Ni_x(NH_3)_6Cl_2$. The binding energy for Ni^{2+}-NH_3 is higher than the Mg^{2+}-NH_3 and Mn^{2+}-NH_3, and therefore the strong contribution of Ni in $Mg_{1-x}Ni_x(NH_3)_6Cl_2$ (up to x = 0.1) gives bigger shift in the NH_3 desorption temperatures, compared to the Mn content in $Mg_{1-x}Mn_x(NH_3)_6Cl_2$ (up to x = 0.5). This observation suggests that NH_3 release temperatures are mainly affected by the presence of the metal with higher NH_3 binding energy, while the metal with lower binding energy can affect the NH_3 desorption temperatures only with high contents in the solid solution.

Chapter 4. Summary and Outlook

Thermochemical heat storage and reutilization of surplus heat can provide a significant contribution to the reduction of our carbon footprint. Several materials and reactor designs have been reported in the past decades in the pursuit for efficient thermochemical heat storage systems. Metal halide ammines have been extensively studied as indirect hydrogen storage materials. Recently these compounds have received new interest due to their potential applications for THS as they exhibit high energy densities and good NH_3 cyclability. In this dissertation, $MgCl_2$-based ammines have been studied, and the NH_3 storage properties were studied in the temperature range 20-400 °C. Understanding the correlation between the chemical and physical properties is important to tailor new functional materials towards specific applications. Here it has been demonstrated how the sorption properties of $Mg(NH_3)_xCl_2$ could be tailored by the formation of solid solutions with $MnCl_2$ and $NiCl_2$. The NH_3 release temperatures of the mixed metal hexammines were decreased by the addition of $MnCl_2$ or increased by the addition of $NiCl_2$, due to different metal-NH_3 binding energies as compared to $MgCl_2$. This study suggests that metal halides with similar crystal structures but different metal-NH_3 binding energies can be mixed, and thus the thermal stability of the compounds can be altered.

In the past decades, several advancements have been achieved in the research on THS systems, but more insight is necessary to utilize the technology on a commercial level. The overall development of THS systems is based on the development of each of the main components, such as the thermochemical heat storage material, the heat exchanger design and the reactor design. In this dissertation, all three components for the THS system were investigated using neutron imaging. This method allows for observation of NH_3 uptake and release in the powder bed due to the high sensitivity of neutrons to hydrogen. Neutron imaging was used for investigation of heat storage materials and systems for the first time within this research project, and thus providing new perspectives for THS system analysis. This research provides new approaches for investigations of thermal energy storage materials, as well as the complete reactor design.

The main aim of this dissertation was to investigate the THS reactor using neutron imaging and continuously develop the reactor design based on the results. The materials investigated are based on the $SrCl_2/Sr(NH_3)_8Cl_2$ system, which are interesting due to its high cyclability. $SrCl_2$ is

abundant, non-toxic and inexpensive, and the thermochemistry of $Sr(NH_3)_8Cl_2$ fulfills the requirements for a THS reactor aimed towards applications as waste heat recovery in the temperature range 40-80 °C. In the initial reactor design, a stainless-steel honeycomb heat exchanger with embedded $SrCl_2$ was investigated with neutron imaging. $SrCl_2$ was cycled with NH_3, and the reaction rate was investigated by performing qualitative analysis of the NH_3 content as a function of time. A significant volume expansion was observed by neutron tomography during NH_3 uptake, resulting in a distortion of the honeycomb due to mechanical stress. The THS reactor design was upgraded accordingly, making it more mechanically stabilized by welding, while the $SrCl_2$ powder was confined in an expanded natural graphite matrix to suppress powder volume expansion. The neutron imaging results showed improved NH_3 sorption kinetics of the $SrCl_2$-ENG composite material, while an improved heat conductivity was also observed. The spatio-temporal NH_3 concentration in $Sr(NH_3)_xCl_2$ was calculated to follow the ab-/desorption kinetics and the reaction advancement. The stainless-steel honeycomb did not experience mechanical stresses, but it showed too poor heat conductivity. The THS reactor prototype was subsequently upgraded to an aluminum honeycomb. Neutron imaging investigations of the $SrCl_2/Sr(NH_3)_8Cl_2$ system embedded in an aluminum honeycomb revealed an excellent performance as a heat exchanger.

A good knowledge of the THS materials' chemical and physical properties and an understanding of the fundamental features relevant for a given application, are crucial for a rational design of the THS reactor and system. Here it is demonstrated how such information can be achieved using neutron imaging. The experiments revealed new insight into the efficiency of the sorption processes by observing how heat is transferred within the honeycomb, and it is clearly observed by the change in NH_3 content. Understanding the heat conduction and the corresponding NH_3-sorption properties are crucial for an effective design of the THS reactor.

A numerical model to simulate the performance of a heat exchanger and a complete THS system to investigate their potential performance for real-scale application has been developed. The detailed numerical analysis on the heat exchanger allows to choose the heat exchanger design suitable for the application. In our study, such a 3D model of the heat exchanger, *i.e.* the honeycomb, was built in COMSOL Multiphysics, and the performance of the $SrCl_2$-NH_3 system was validated against the experimental results obtained by neutron radiography. The comparison between the numerical and the experimental results showed a good agreement, suggesting that the

numerical studies can be used for predicting of the reaction behavior. Similar numerical analysis will be performed for the $SrCl_2/Sr(NH_3)_8Cl_2$-ENG composite material embedded in the honeycomb heat exchanger.

For the $SrCl_2/Sr(NH_3)_8Cl_2$-ENG system, a compact THS reactor containing 8-10 honeycomb discs has been designed and constructed with a second container for NH_3 storage during discharge. The optimal operating temperature of the reactor can be 80-115 °C and the NH_3 pressure in the range 1-12 bar. This reactor-prototype can be operated with an energy storage capacity of 1.8-2.7 MJ. This final reactor design and complete THS system with a large-scale reactor and heat exchangers is now being built at The Royal Institute of Technology (KTH) in Sweden as part of this research project initiative.

The implementation of compact and cost-effective THS systems for either small-scale domestic heating or large-scale district heating would valorize the low-grade waste heat from industry and could lead to a significant saving of the raw energy consumption. By balancing the energy production and demand, THS systems can reduce peak demands, CO_2 emissions and energy cost, while increasing the overall efficiency of energy systems. The future of energy storage is indeed interesting, and the way human produces, stores and consumes energy are expected to change significantly in the forthcoming decades.

References

(1) Marland, G.; Rotty, R. M.; Treat, N. L. CO_2 from Fossil Fuel Burning: Global Distribution of Emissions. *Tellus B,* **1985**, *37B* (4–5), 243–258.
(2) Dignon, J. NO_x and SO_x Emissions from Fossil Fuels: A Global Distribution. *Atmos. Env. A - Gen.* **1992**, *26* (6), 1157–1163.
(3) Bader, C. R., Christian Braneon, and Daniel. Increasing resiliency to extreme weather https://climate.nasa.gov/news/2648/increasing-resiliency-to-extreme-weather (accessed May 1, 2020).
(4) Our World in Data https://ourworldindata.org (accessed Apr 27, 2020).
(5) Stocker, T. F.; Qin, D.; Plattner, G.-K.; Tignor, M. M. B.; Allen, S. K.; Boschung, J.; Nauels, A.; Xia, Y.; Bex, V.; Midgley, P. M. Working Group I Contribution to the Fifth Assessment Report of the Intergovernmental Panel on Climate Change. 14.
(6) Change, N. G. C. Carbon Dioxide Concentration | NASA Global Climate Change https://climate.nasa.gov/vital-signs/carbon-dioxide (accessed May 4, 2020).
(7) Lacis, A. A.; Schmidt, G. A.; Rind, D.; Ruedy, R. A. Atmospheric CO_2: Principal Control Knob Governing Earth's Temperature. *Science* **2010**, *330* (6002), 356–359.
(8) Mundaca, G. How Much Can CO_2 Emissions Be Reduced If Fossil Fuel Subsidies Are Removed? *Energy Econ.* **2017**, *64*, 91–104.
(9) United Nations Treaty Collection. Chapter XXVII: Environment https://treaties.un.org/pages/ViewDetails.aspx?src=TREATY&mtdsg_no=XXVII-7-d&chapter=27 (accessed Apr 16, 2020).
(10) Paris Agreement - Status of Ratification | UNFCCC https://cop23.unfccc.int/process/the-paris-agreement/status-of-ratification (accessed May 12, 2020).
(11) Aleklett, K.; Höök, M.; Jakobsson, K.; Lardelli, M.; Snowden, S.; Söderbergh, B. The Peak of the Oil Age – Analyzing the World Oil Production Reference Scenario in World Energy Outlook 2008. *Energy Policy,* **2010**, *38* (3), 1398–1414.
(12) Kaldellis, J. K.; Zafirakis, D. The Wind Energy (r)Evolution: A Short Review of a Long History. *Renew. Energy,* **2011**, *36* (7), 1887–1901.
(13) Kamran, M.; Fazal, M. R.; Mudassar, M.; Ahmed, S. R.; Adnan, M.; Abid, I.; Randhawa, F. J. S.; Shams, H. Solar Photovoltaic Grid Parity: A Review of Issues, Challenges and Status of Different PV Markets. *Int. J. Renew. Energy Res. (IJRER),* **2019**, *9* (1), 244–260.
(14) Stehly, T. J.; Beiter, P. C. *2018 Cost of Wind Energy Review*; NREL/TP-5000-74598; National Renewable Energy Lab. (NREL), Golden, CO (United States), 2020.
(15) Chinmoy, L.; Iniyan, S.; Goic, R. Modeling Wind Power Investments, Policies and Social Benefits for Deregulated Electricity Market – A Review. *Appl. Energy,* **2019**, *242*, 364–377.
(16) Bukar, A. L.; Tan, C. W. A Review on Stand-Alone Photovoltaic-Wind Energy System with Fuel Cell: System Optimization and Energy Management Strategy. *J. Clean. Prod.* **2019**, *221*, 73–88.
(17) Sherwani, A. F.; Usmani, J. A.; Varun. Life Cycle Assessment of Solar PV Based Electricity Generation Systems: A Review. *Renew. Sust. Energ. Rev.* **2010**, *14* (1), 540–544.
(18) Lewis, N. S. Toward Cost-Effective Solar Energy Use. *Science* **2007**, *315* (5813), 798–801.
(19) Considine, T. J. The Impacts of Weather Variations on Energy Demand and Carbon Emissions. *Resour. Energy Econ.* **2000**, *22* (4), 295–314.
(20) Black, M.; Strbac, G. Value of Bulk Energy Storage for Managing Wind Power Fluctuations. *IEEE Trans. Energy Convers.* **2007**, *22* (1), 197–205.

(21) Morgan, T. World Energy Outlook. **2010**.
(22) Whittingham, M. S.; Savinell, R. F.; Zawodzinski, T. Introduction: Batteries and Fuel Cells. *Chem. Rev.* **2004**, *104* (10), 4243–4244.
(23) Maurya, S.; Shin, S.-H.; Kim, Y.; Moon, S.-H. A Review on Recent Developments of Anion Exchange Membranes for Fuel Cells and Redox Flow Batteries. *RSC Adv.* **2015**, *5* (47), 37206–37230.
(24) Cano, Z. P.; Banham, D.; Ye, S.; Hintennach, A.; Lu, J.; Fowler, M.; Chen, Z. Batteries and Fuel Cells for Emerging Electric Vehicle Markets. *Nat. Energy,* **2018**, *3* (4), 279–289.
(25) Gröger, O.; Gasteiger, H. A.; Suchsland, J.-P. Review—Electromobility: Batteries or Fuel Cells? *J. Electrochem. Soc.* **2015**, *162* (14), A2605.
(26) Debe, M. K. Electrocatalyst Approaches and Challenges for Automotive Fuel Cells. *Nature,* **2012**, *486* (7401), 43–51.
(27) Zeng, X.; Li, M.; El-Hady, D. A.; Alshitari, W.; Al-Bogami, A. S.; Lu, J.; Amine, K. Commercialization of Lithium Battery Technologies for Electric Vehicles. *Adv. Energy Mater.* **2019**, *9* (27), 1900161.
(28) Freitas Gomes, I. S.; Perez, Y.; Suomalainen, E. Coupling Small Batteries and PV Generation: A Review. *Renew. Sust. Energ. Rev.* **2020**, *126*, 109835.
(29) Malhotra, A.; Battke, B.; Beuse, M.; Stephan, A.; Schmidt, T. Use Cases for Stationary Battery Technologies: A Review of the Literature and Existing Projects. *Renew. Sust. Energ. Rev.* **2016**, *56*, 705–721.
(30) May, G. J.; Davidson, A.; Monahov, B. Lead Batteries for Utility Energy Storage: A Review. *J. Energy Storage,* **2018**, *15*, 145–157.
(31) Keiner, D.; Ram, M.; Barbosa, L. D. S. N. S.; Bogdanov, D.; Breyer, C. Cost Optimal Self-Consumption of PV Prosumers with Stationary Batteries, Heat Pumps, Thermal Energy Storage and Electric Vehicles across the World up to 2050. *Solar Energy,* **2019**, *185*, 406–423.
(32) Pelay, U.; Luo, L.; Fan, Y.; Stitou, D.; Rood, M. Thermal Energy Storage Systems for Concentrated Solar Power Plants. *Renew. Sust. Energ. Rev.* **2017**, *79*, 82–100.
(33) Wagner, S. J.; Rubin, E. S. Economic Implications of Thermal Energy Storage for Concentrated Solar Thermal Power. *Renew. Energy,* **2014**, *61*, 81–95.
(34) Hailu, G. Seasonal Solar Thermal Energy Storage. *Thermal Energy Battery with Nano-enhanced PCM,* **2018**.
(35) Dincer, I.; Rosen, A. M. *Thermal Energy Storage: Systems and Applications, 2nd Edition | Wiley*; **2011**.
(36) Sarbu, I.; Sebarchievici, C. A Comprehensive Review of Thermal Energy Storage. *Sustainability,* **2018**, *10* (1), 191.
(37) Dincer, I.; Dost, S.; Li, X. Performance Analyses of Sensible Heat Storage Systems for Thermal Applications. *Int. J. Energy Res.* **1997**, *21* (12), 1157–1171.
(38) Tao, Y. B.; He, Y.-L. A Review of Phase Change Material and Performance Enhancement Method for Latent Heat Storage System. *Renew. Sust. Energ. Rev.* **2018**, *93*, 245–259.
(39) Aydin, D.; Casey, S. P.; Riffat, S. The Latest Advancements on Thermochemical Heat Storage Systems. *Renew. Sust. Energ. Rev.* **2015**, *41*, 356–367.
(40) Nallusamy, N.; Sampath, S.; Velraj, R. Experimental Investigation on a Combined Sensible and Latent Heat Storage System Integrated with Constant/Varying (Solar) Heat Sources. *Renew. Energy,* **2007**, *32* (7), 1206–1227.

(41) Parameshwaran, R.; Kalaiselvam, S.; Harikrishnan, S.; Elayaperumal, A. Sustainable Thermal Energy Storage Technologies for Buildings: A Review. *Renew. Sust. Energ. Rev.* **2012**, *16* (5), 2394–2433.
(42) Zhang, H. L.; Baeyens, J.; Degrève, J.; Cacères, G. Concentrated Solar Power Plants: Review and Design Methodology. *Renew. Sust. Energ. Rev.* **2013**, *22*, 466–481.
(43) Elliott, D. E.; Stephens, T.; Barabas, M. F.; Beckmann, G.; Bonnin, J.; Bricard, A.; Brumleve, T. D.; Delancey, G. B.; Kruissink, Ch. A.; Lane, G. A.; Laws, W. R.; Robertson, R. F. S.; Schroeder, J. Working group a - high temperature thermal energy storage. In *Thermal Energy Storage*; Kovach, E. G., Ed.; Pergamon, **2013**; pp 11–26.
(44) Abdin, Z.; Khalilpour, K. R. Chapter 4 - Single and Polystorage Technologies for Renewable-Based Hybrid Energy Systems. In *Polygeneration with Polystorage for Chemical and Energy Hubs*; Khalilpour, K. R., Ed.; Academic Press, **2019**; pp 77–131.
(45) Nomura, T.; Okinaka, N.; Akiyama, T. Technology of Latent Heat Storage for High Temperature Application: A Review. *ISIJ Int.* **2010**, *50* (9), 1229–1239.
(46) Cárdenas, B.; León, N. High Temperature Latent Heat Thermal Energy Storage: Phase Change Materials, Design Considerations and Performance Enhancement Techniques. *Renew. Sust. Energ. Rev.* **2013**, *27*, 724–737.
(47) Adinberg, R.; Zvegilsky, D.; Epstein, M. Heat Transfer Efficient Thermal Energy Storage for Steam Generation. *Energy Convers. Manag.* **2010**, *51* (1), 9–15.
(48) Khare, S.; Dell'Amico, M.; Knight, C.; McGarry, S. Selection of Materials for High Temperature Latent Heat Energy Storage. *Sol. Energy Mater. Sol.* **2012**, *107*, 20–27.
(49) Wang, X.; Liu, J.; Zhang, Y.; Di, H.; Jiang, Y. Experimental Research on a Kind of Novel High Temperature Phase Change Storage Heater. *Energy Convers. Manag.* **2006**, *47* (15), 2211–2222.
(50) Sun, J. Q.; Zhang, R. Y.; Liu, Z. P.; Lu, G. H. Thermal Reliability Test of Al–34%Mg–6%Zn Alloy as Latent Heat Storage Material and Corrosion of Metal with Respect to Thermal Cycling. *Energy Convers. Manag.* **2007**, *48* (2), 619–624.
(51) Felderhoff, M.; Urbanczyk, R.; Peil, S. Thermochemical Heat Storage for High Temperature Applications – A Review. *Green,* **2013**, *3* (2), 113–123.
(52) Donkers, P. A. J.; Sogutoglu, L. C.; Huinink, H. P.; Fischer, H. R.; Adan, O. C. G. A Review of Salt Hydrates for Seasonal Heat Storage in Domestic Applications. *Appl. Energy,* **2017**, *199*, 45–68.
(53) Carrillo, A. J.; González-Aguilar, J.; Romero, M.; Coronado, J. M. Solar Energy on Demand: A Review on High Temperature Thermochemical Heat Storage Systems and Materials. *Chem. Rev.* **2019**, *119* (7), 4777–4816.
(54) Harries, D. N.; Paskevicius, M.; Sheppard, D. A.; Price, T. E. C.; Buckley, C. E. Concentrating Solar Thermal Heat Storage Using Metal Hydrides. *Proc. IEEE,* **2012**, *100* (2), 539–549.
(55) Møller, K. T.; Sheppard, D.; Ravnsbæk, D. B.; Buckley, C. E.; Akiba, E.; Li, H.-W.; Jensen, T. R. Complex Metal Hydrides for Hydrogen, Thermal and Electrochemical Energy Storage. *Energies,* **2017**, *10* (10), 1645.
(56) Jarimi, H.; Aydin, D.; Yanan, Z.; Ozankaya, G.; Chen, X.; Riffat, S. Review on the Recent Progress of Thermochemical Materials and Processes for Solar Thermal Energy Storage and Industrial Waste Heat Recovery. *Int. J. Low-Carbon Tec.* **2019**, *14* (1), 44–69.

(57) Sogutoglu, L. C.; Donkers, P. A. J.; Fischer, H. R.; Huinink, H. P.; Adan, O. C. G. In-Depth Investigation of Thermochemical Performance in a Heat Battery: Cyclic Analysis of K_2CO_3, $MgCl_2$ and Na_2S. *Appl. Energy,* **2018**, *215*, 159–173.
(58) Yan, T.; Kuai, Z. H.; Wu, S. F. Experimental Investigation on a $MnCl_2$–$SrCl_2$/NH_3 Thermochemical Resorption Heat Storage System. *Renew. Energy,* **2020**, *147*, 874–883.
(59) Casey, S. P.; Aydin, D.; Elvins, J.; Riffat, S. Salt Impregnated Desiccant Matrices for 'Open' Thermochemical Energy Conversion and Storage – Improving Energy Density Utilisation through Hygrodynamic & Thermodynamic Reactor Design. *Energy Convers. Manag.* **2017**, *142*, 426–440.
(60) Aydin, D.; Casey, S. P.; Chen, X.; Riffat, S. Novel "Open-Sorption Pipe" Reactor for Solar Thermal Energy Storage. *Energy Convers. Manag.* **2016**, *121*, 321–334.
(61) Michel, B.; Mazet, N.; Neveu, P. Experimental Investigation of an Innovative Thermochemical Process Operating with a Hydrate Salt and Moist Air for Thermal Storage of Solar Energy: Global Performance. *Appl. Energy,* **2014**, *129*, 177–186.
(62) Tatsidjodoung, P.; Le Pierrès, N.; Heintz, J.; Lagre, D.; Luo, L.; Durier, F. Experimental and Numerical Investigations of a Zeolite 13X/Water Reactor for Solar Heat Storage in Buildings. *Energy Convers. Manag.* **2016**, *108*, 488–500.
(63) Zettl, B.; Englmair, G.; Somitsch, W. An Open Sorption Heat Storage Concept and Materials for Building Heat Supply. In *Energy Procedia*; Elsevier, **2015**; Vol. 73, pp 297–304.
(64) Haije, W. G.; Veldhuis, J. B. J.; Smeding, S. F.; Grisel, R. J. H. Solid/Vapour Sorption Heat Transformer: Design and Performance. *Appl. Therm. Eng.* **2007**, *27* (8), 1371–1376.
(65) van der Pal, M.; de Boer, R.; Veldhuis, J. B. J.; Smeding, S. F. Thermally Driven Ammoniasalt Type II Heat Pump: Development and Test of a Prototype; Berlin, 7-9 September.
(66) van der Pal, M.; Critoph, R. E. Performance of $CaCl_2$-Reactor for Application in Ammonia-Salt Based Thermal Transformers. *Appl. Therm. Eng.* **2017**, *126*, 518–524.
(67) Fopah-Lele, A.; Rohde, C.; Neumann, K.; Tietjen, T.; Rönnebeck, T.; N'Tsoukpoe, K. E.; Osterland, T.; Opel, O.; Ruck, W. K. L. Lab-Scale Experiment of a Closed Thermochemical Heat Storage System Including Honeycomb Heat Exchanger. *Energy,* **2016**, *114*, 225–238.
(68) Liu, H.; Nagano, K.; Sugiyama, D.; Togawa, J.; Nakamura, M. Honeycomb Filters Made from Mesoporous Composite Material for an Open Sorption Thermal Energy Storage System to Store Low-Temperature Industrial Waste Heat. *Int. J. Heat Mass Transf.* **2013**, *65*, 471–480.
(69) Yamamoto, H.; Sanga, S.; Tokunaga, J.; Sakamoto, Y. Performance of Thermal Energy Storage Unit Using $CaCl_2$-NH_3 System Mixed with Ti. *Can. J. Chem. Eng.* **1990**, *68* (6), 948–951.
(70) Sakamoto, Y.; Yamamoto, H. Performance of Thermal Energy Storage Unit Using Solid Ammoniated Salt ($CaCl_2$-NH_3 System). *Nat. Resour.* **2014**, *05* (08), 337.
(71) Khartchenko, N. V.; Kharchenko, V. M. *Advanced Energy Systems, 2nd Edition*; CRC Press, **2013**.
(72) Kiyabu, S.; Lowe, J. S.; Ahmed, A.; Siegel, D. J. Computational Screening of Hydration Reactions for Thermal Energy Storage: New Materials and Design Rules. *Chem. Mater.* **2018**, *30* (6), 2006–2017.
(73) E. Bird, J.; D. Humphries, T.; Paskevicius, M.; Poupin, L.; E. Buckley, C. Thermal Properties of Thermochemical Heat Storage Materials. *Phys. Chem. Chem. Phys.* **2020**, *22* (8), 4617–4625.

(74) Jensen, P. B. *Computational Design of New Materials for Ammonia Storage*; PhD-thesis, Department of Energy Conversion and Storage, Technical University of Denmark, **2014**.
(75) Klerke, A.; Christensen, C. H.; Nørskov, J. K.; Vegge, T. Ammonia for Hydrogen Storage: Challenges and Opportunities. *J. Mater. Chem.* **2008**, *18* (20), 2304–2310.
(76) Christensen, C. H.; Sørensen, R. Z.; Johannessen, T.; Quaade, U. J.; Honkala, K.; Elmøe, T. D.; Køhler, R.; Nørskov, J. K. Metal Ammine Complexes for Hydrogen Storage. *J. Mater. Chem.* **2005**, *15* (38), 4106–4108.
(77) Sørensen, R. Z.; Hummelshøj, J. S.; Klerke, A.; Reves, J. B.; Vegge, T.; Nørskov, J. K.; Christensen, C. H. Indirect, Reversible High-Density Hydrogen Storage in Compact Metal Ammine Salts. *J. Am. Chem. Soc.* **2008**, *130* (27), 8660–8668.
(78) He, T.; Pachfule, P.; Wu, H.; Xu, Q.; Chen, P. Hydrogen Carriers. *Nat. Rev. Mater.* **2016**, *1* (12), 1–17.
(79) Biltz, W. Beiträge zur systematischen Verwandtschaftslehre XXIV. Über das Vermögen kristallisierter Salze, Ammoniak zu binden. *Z. Anorg. Allg. Chem.* **1923**, *130* (1), 93–139.
(80) Tekin, A.; S. Hummelshøj, J.; S. Jacobsen, H.; Sveinbjörnsson, D.; Blanchard, D.; K. Nørskov, J.; Vegge, T. Ammonia Dynamics in Magnesium Ammine from DFT and Neutron Scattering. *Energy Environ. Sci.* **2010**, *3* (4), 448–456.
(81) Jacobsen, H. S.; Hansen, H. A.; Andreasen, J. W.; Shi, Q.; Andreasen, A.; Feidenhans'l, R.; Nielsen, M. M.; Ståhl, K.; Vegge, T. Nanoscale Structural Characterization of $Mg(NH_3)_6Cl_2$ during NH_3 Desorption: An in Situ Small Angle X-Ray Scattering Study. *Chem. Phys. Lett.* **2007**, *441* (4), 255–260.
(82) Bjerre Jensen, P.; Lysgaard, S.; J. Quaade, U.; Vegge, T. Designing Mixed Metal Halide Ammines for Ammonia Storage Using Density Functional Theory and Genetic Algorithms. *Phys. Chem. Chem. Phys.* **2014**, *16* (36), 19732–19740.
(83) Jensen, P. B.; Bialy, A.; Blanchard, D.; Lysgaard, S.; Reumert, A. K.; Quaade, U. J.; Vegge, T. Accelerated DFT-Based Design of Materials for Ammonia Storage. *Chem. Mater.* **2015**, *27* (13), 4552–4561.
(84) Lepinasse, E.; Spinner, B. Cold Production Through Coupling of Solid-Gas Reactors .1. Performance Analysis. *Int. J. Refrig.-Rev. Int. Froid* **1994**, *17* (5), 309–322.
(85) Biltz, W.; Rahlfs, E. Beiträge Zur Systematischen Verwandtschaftslehre. XLV. Über Reaktionsermöglichung Durch Gitterweitung Und Über Ammoniakate Der Fluoride. *Z. Anorg. Allg. Chem.* **1927**, *166* (1), 351–376.
(86) Wentworth, W. E.; Raldow, W. M.; Corbett, G. E. Correlation of Thermodynamic Properties for Dissociation of Ammines of Divalent Metal Halides. *Inorg. Chim. Acta,* **1978**, *30*, L299–L301.
(87) Clark, G. L. Secondary Valence in the Light of Recent Researches; I, Inorganic Ammines. *Am. J. Sci.* **1924**, *7* (37), 1–23.
(88) Hart, A. B.; Partington, J. R. 36. Dissociation Pressures of Compounds of Ammonia and Trideuterammonia with Some Metallic Salts. *J. Chem. Soc.* **1943**, 104–118.
(89) Biltz, W.; Hüttig, G. F. Über die Auswertung von Dissoziationsmessungen bei Ammoniakaten nach dem Theorem von Nernst mit Hilfe von Nomogrammen. *Z. Anorg. Allg. Chem.* **1919**, *109* (1), 111–125.
(90) Biltz, W.; Hüttig, G. F. Beiträge Zur Systematischen Verwandtschaftslehre. XII. Über Die Verbindungen von Ammoniak Mit Metallischem Calcium, Strontium Und Barium. *Z. Anorg. Allg. Chem.* **1920**, *114* (1), 241–265.
(91) Cotton, F. A. Bond energies in transition metal complexes. *Acta Chem. Scand.,* **1956**, *10*.

(92) Vegge, T.; Sørensen, R. Z.; Klerke, A.; Hummelshøj, J. S.; Johannessen, T.; Nørskov, J. K.; Christensen, C. H. 19 - Indirect Hydrogen Storage in Metal Ammines. In *Solid-State Hydrogen Storage*; Walker, G., Ed.; Woodhead Publishing Series in Electronic and Optical Materials; Woodhead Publishing, **2008**; pp 533–564.
(93) Makepeace, J. W.; He, T.; Weidenthaler, C.; Jensen, T. R.; Chang, F.; Vegge, T.; Ngene, P.; Kojima, Y.; de Jongh, P. E.; Chen, P.; David, W. I. F. Reversible Ammonia-Based and Liquid Organic Hydrogen Carriers for High-Density Hydrogen Storage: Recent Progress. *Int. J. Hydrog. Energy,* **2019**, *44* (15), 7746–7767.
(94) Hirscher, M.; Yartys, V. A.; Baricco, M.; Bellosta von Colbe, J.; Blanchard, D. *et. al.* Materials for Hydrogen-Based Energy Storage – Past, Recent Progress and Future Outlook. *J. Alloys Compd.* **2020**, *827*, 153548.
(95) Lan, R.; Irvine, J. T. S.; Tao, S. Ammonia and Related Chemicals as Potential Indirect Hydrogen Storage Materials. *Int. J. Hydrog. Energy,* **2012**, *37* (2), 1482–1494.
(96) Westman, S.; Werner, P.-E.; Schuler, T.; Raldow, W. X-Ray Investigations of Ammines of Alkaline Earth Metal Halides. I. The Structures of $CaCl_2(NH_3)_8$, $CaCl_2(NH_3)_2$ and the Decomposition Product CaClOH. **1981**, *35*, 467–472.
(97) Fournier, G. G. M.; Cumming, I. W.; Hellgardt, K. High Performance Direct Ammonia Solid Oxide Fuel Cell. *J. Power Sources,* **2006**, *162* (1), 198–206.
(98) Maffei, N.; Pelletier, L.; McFarlan, A. A High Performance Direct Ammonia Fuel Cell Using a Mixed Ionic and Electronic Conducting Anode. *J. Power Sources,* **2008**, *175* (1), 221–225.
(99) Boggs, B. K.; Botte, G. G. On-Board Hydrogen Storage and Production: An Application of Ammonia Electrolysis. *J. Power Sources,* **2009**, *192* (2), 573–581.
(100) Wang, Y.; Chen, K. S.; Mishler, J.; Cho, S. C.; Adroher, X. C. A Review of Polymer Electrolyte Membrane Fuel Cells: Technology, Applications, and Needs on Fundamental Research. *Appl. Energy,* **2011**, *88* (4), 981–1007.
(101) Halseid, R.; Vie, P. J. S.; Tunold, R. Effect of Ammonia on the Performance of Polymer Electrolyte Membrane Fuel Cells. *J. Power Sources,* **2006**, *154* (2), 343–350.
(102) Elmøe, T. D.; Sørensen, R. Z.; Quaade, U.; Christensen, C. H.; Nørskov, J. K.; Johannessen, T. A High-Density Ammonia Storage/Delivery System Based on $Mg(NH_3)_6Cl_2$ for SCR–DeNO_x in Vehicles. *Chem. Eng. Sci.* **2006**, *61* (8), 2618–2625.
(103) Liu, C. Y.; Aika, K. Ammonia Absorption into Alkaline Earth Metal Halide Mixtures as an Ammonia Storage Material. *Ind. Eng. Chem. Res.* **2004**, *43* (23), 7484–7491.
(104) Lai, S.; Meng, D.; Zhan, W.; Guo, Y.; Guo, Y.; Zhang, Z.; Lu, G. The Promotional Role of Ce in Cu/ZSM-5 and in Situ Surface Reaction for Selective Catalytic Reduction of NO_x with NH_3. *RSC Advances,* **2015**, *5* (110), 90235–90244.
(105) Fritz, A.; Pitchon, V. The Current State of Research on Automotive Lean NO_x Catalysis. *Appl. Catal. B.* **1997**, *13* (1), 1–25.
(106) Peters, A.; Langer, H.-J.; Jokl, B.; Müller, W.; Klein, H.; Ostgathe, K. Catalytic NO_x Reduction on a Passenger Car Diesel Common Rail Engine. *SAE Transactions,* **1998**, *107*, 381–391.
(107) Lepinasse, E.; Spinner, B. Production de froid par couplage de réacteurs solide-gaz I: Analyse des performances de tels systèmes. *Int. J. Refrig.* **1994**, *17* (5), 309–322.
(108) Lepinasse, E.; Spinner, B. Production de froid par couplage de réacteurs solide-gaz II: Performance d'un pilote de 1 à 2 kW. *Int. J. Refrig.* **1994**, *17* (5), 323–328.

(109) Aoki, T.; Ichikawa, T.; Miyaoka, H.; Kojima, Y. Thermodynamics on Ammonia Absorption of Metal Halides and Borohydrides. *J. Phys. Chem. C,* **2014**, *118* (32), 18412–18416.
(110) Zhang, T.; Miyaoka, H.; Miyaoka, H.; Ichikawa, T.; Kojima, Y. Review on Ammonia Absorption Materials: Metal Hydrides, Halides, and Borohydrides. *ACS Appl. Energy Mater.* **2018**, *1* (2), 232–242.
(111) Jones, M. O.; Royse, D. M.; Edwards, P. P.; David, W. I. F. The Structure and Desorption Properties of the Ammines of the Group II Halides. *Chem. Phys.* **2013**, *427*, 38–43.
(112) Laios, M. *Ammonia Metal Halides Thermochemical Heat Storage System Design*, Master thesis **2017**.
(113) Gunasekara, S. N.; Laios, M.; Karabanova, A.; Martin, V.; Blanchard, D. Design of a Bench-Scale Ammonia-$SrCl_2$ Thermochemical Storage System Using Numerical Modelling. *Seminar: Advances in Thermal Energy Storage*, Lleida, **2019**, 10.
(114) Shannon, R. D. Revised Effective Ionic Radii and Systematic Studies of Interatomic Distances in Halides and Chalcogenides. *Acta Cryst. A,* **1976**, *32* (5), 751–767.
(115) Olovsson, I. Packing Principles in the Structures of Metal Ammine Salts. *Acta Cryst.* **1965**, *18* (5), 889–893.
(116) Eßmann, R.; Kreiner, G.; Niemann, A.; Rechenbach, D.; Schmieding, A.; Sichla, T.; Zachwieja, U.; Jacobs, H. Isotype Strukturen einiger Hexaamminmetall(II)-halogenide von 3d-Metallen: $[V(NH_3)_6]I_2$, $[Cr(NH_3)_6]I_2$, $[Mn(NH_3)_6]Cl_2$, $[Fe(NH_3)_6]Cl_2$, $[Fe(NH_3)_6]Br_2$, $[Co(NH_3)_6]Br_2$ und $[Ni(NH_3)_6]Cl_2$. *Z. Anorg. Allg. Chem.* **1996**, *622* (7), 1161–1166.
(117) Hwang, I.-C.; Drews, T.; Seppelt, K. $Mg(NH_3)_6Hg_{22}$, a Mercury Intercalation Compound. *J. Am. Chem. Soc.* **2000**, *122* (35), 8486–8489.
(118) Song, X.; Liu, G.; Sun, Z.; Yu, J. Comparative Study on the Molecular and Electronic Structure of $MgCl_2{\cdot}6NH_3$ and $MgCl_2{\cdot}6H_2O$. *Asia-Pac. J. Chem. Eng.* **2012**, *7* (2), 221–226.
(119) Zhu, H.; Gu, X.; Yao, K.; Gao, L.; Chen, J. Large-Scale Synthesis of $MgCl_2{\cdot}6NH_3$ as an Ammonia Storage Material. *Ind. Eng. Chem. Res.* **2009**, *48* (11), 5317–5320.
(120) Walker, G. *Solid-State Hydrogen Storage: Materials and Chemistry*; Elsevier, **2008**.
(121) Bialy, A.; Jensen, P. B.; Blanchard, D.; Vegge, T.; Quaade, U. J. Solid Solution Barium–Strontium Chlorides with Tunable Ammonia Desorption Properties and Superior Storage Capacity. *J. Solid State Chem.* **2015**, *221*, 32–36.
(122) Leineweber, A.; Friedriszik, M. W.; Jacobs, H. Preparation and Crystal Structures of $Mg(NH_3)_2Cl_2$, $Mg(NH_3)_2Br_2$, and $Mg(NH_3)_2I_2$. *J. Solid State Chem.* **1999**, *147* (1), 229–234.
(123) Leineweber, A.; Jacobs, H.; Ehrenberg, H. Crystal Structure of $Ni(NH_3)Cl_2$ and $Ni(NH_3)Br_2$. *Z. Anorg. Allg. Chem.* **2000**, *626* (10), 2146–2152.
(124) Pauling, L. On the Crystal Structure of the Chlorides of Certain Bivalent Elements. *PNAS,* **1929**, *15* (9), 709–712.
(125) Tornero, J. D.; Fayos, J. Single Crystal Structure Refinement of $MnCl_2$. *Z. Krist - Cryst. Mater.* **2015**, *192* (1–4), 147–148.
(126) Ferrari, A.; Braibanti, A.; Bigliardi, G. Refinement of the Crystal Structure of $NiCl_2$ and of Unit-Cell Parameters of Some Anhydrous Chlorides of Divalent Metals. *Acta Cryst.* **1963**, *16* (8), 846–847.
(127) Lysgaard, S.; Ammitzbøll, A. L.; Johnsen, R. E.; Norby, P.; Quaade, U. J.; Vegge, T. Resolving the Stability and Structure of Strontium Chloride Amines from Equilibrium Pressures, XRD and DFT. *Int. J. Hydrog. Energy,* **2012**, *37* (24), 18927–18936.

(128) Johnsen, R. E.; Jensen, P. B.; Norby, P.; Vegge, T. Temperature- and Pressure-Induced Changes in the Crystal Structure of $Sr(NH_3)_8Cl_2$. *J. Phys. Chem. C,* **2014**, *118* (42), 24349–24356.
(129) Gunasekara, S. N.; Soprani, S.; Karabanova, A.; Martin, V.; Blanchard, D. Numerical Design of a Reactor-Heat Exchanger Combined Unit for Ammonia-$SrCl_2$ Thermochemical Storage System. Seminar paper at *ISES SWC2019*, **2019**, pp 1–12.
(130) Kresse, R.; Baudis, U.; Jäger, P.; Riechers, H. H.; Wagner, H.; Winkler, J.; Wolf, H. U. Barium and Barium Compounds. In *Ullmann's Encyclopedia of Industrial Chemistry*; American Cancer Society, **2007**.
(131) Khan, A. A.; Deshpande, V. T. Thermal Expansion of Strontium Sulphide, SrS, and Strontium Chloride, $SrCl_2$. *Acta Cryst. A,* **1968**, *24* (3), 402–402.
(132) Mark, H.; Tolksdorf, S. Über das Beugungsvermögen der Atome für Röntgenstrahlen. *Z. Phys.* **1925**, *33* (1), 681–687.
(133) Kishida, Y.; Aoki, M.; Yamauchi, T. Crystal Structure and NH_3 Desorption Properties of Complex Metal Ammine Chloride. *J. Chem. Eng. Japan,* **2019**, *52* (2), 239–242.
(134) Lasocha, W.; Eick, H. A. The Structure of $Ca_{0.3}Sr_{0.7}Cl_2$ and $Ca_{0.46}Sr_{0.54}Cl_2$ by the X-Ray Rietveld Refinement Procedure. *J. Solid State Chem.* **1988**, *75* (1), 175–182.
(135) King, H. W. Quantitative Size-Factors for Metallic Solid Solutions. *J. Mater. Sci.* **1966**, *1* (1), 79–90.
(136) Hodorowicz, S. A.; Eick, H. A. Phase Relationships in the System $SrBr_2$-$SrCl_2$. *J. Solid State Chem.* **1982**, *43* (3), 271–277.
(137) Hodorowicz, S. A.; Eick, H. A. An X-Ray Diffraction Study of the $SrBr_xI_{2-x}$ System. *J. Solid State Chem.* **1983**, *46* (3), 313–320.
(138) Huot, J.; Cuevas, F.; Deledda, S.; Edalati, K.; Filinchuk, Y.; Grosdidier, T.; Hauback, B. C.; Heere, M.; Jensen, T. R.; Latroche, M.; Sartori, S. Mechanochemistry of Metal Hydrides: Recent Advances. *Materials,* **2019**, *12* (17), 2778.
(139) Iwasaki, T.; Yabuuchi, T.; Nakagawa, H.; Watano, S. Scale-up Methodology for Tumbling Ball Mill Based on Impact Energy of Grinding Balls Using Discrete Element Analysis. *Adv. Powder Technol.* **2010**, *21* (6), 623–629.
(140) Kissinger, H. E. Variation of Peak Temperature With Heating Rate in Differential Thermal Analysis. *J. Res. Natl. Inst. Stand.* **1956**, *57*, 217–221.
(141) Pathak, P. D.; Vasavada, N. G. Thermal Expansion of NaCl, KCl and CsBr by X-Ray Diffraction and the Law of Corresponding States. *Acta Cryst. A,* **1970**, *26* (6), 655–658.
(142) Hansen, B. R. S.; Møller, K. T.; Paskevicius, M.; Dippel, A.-C.; Walter, P.; Webb, C. J.; Pistidda, C.; Bergemann, N.; Dornheim, M.; Klassen, T.; Jørgensen, J.-E.; Jensen, T. R. In Situ X-Ray Diffraction Environments for High-Pressure Reactions. *J. Appl. Cryst.* **2015**, *48* (4), 1234–1241.
(143) Neutron scattering lengths and cross sections. https://www.ncnr.nist.gov/resources/n-lengths/ (accessed May 10, 2020).
(144) Neutron Imaging for the Hydrogen Economy. https://slideplayer.com/slide/9791719/ (accessed Apr 17, 2020).
(145) Hellenbrandt, M. The Inorganic Crystal Structure Database (ICSD)—Present and Future. *Crystallogr. Rev.* **2004**, *10* (1), 17–22.
(146) Kabekkodu, S. N.; Faber, J.; Fawcett, T. New Powder Diffraction File (PDF-4) in Relational Database Format: Advantages and Data-Mining Capabilities. *Acta Cryst. B,* **2002**, *58* (3), 333–337.

(147) Favre-Nicolin, V.; Černý, R. FOX, `free Objects for Crystallography': A Modular Approach to Ab Initio Structure Determination from Powder Diffraction. *J. Appl. Cryst.* **2002**, *35* (6), 734–743.
(148) Favre-Nicolin, V.; Černý, R. A Better FOX: Using Flexible Modelling and Maximum Likelihood to Improve Direct-Space Ab Initio Structure Determination from Powder Diffraction. *Z. Kristal. - Crystal. Mater.* **2004**, *219* (12), 847–856.
(149) Will, G. *Powder Diffraction: The Rietveld Method and the Two Stage Method to Determine and Refine Crystal Structures from Powder Diffraction Data*; Springer Science & Business Media, **2006**.
(150) Dinnebier, R. E.; Leineweber, A.; Evans, J. S. O. *Rietveld Refinement: Practical Powder Diffraction Pattern Analysis Using TOPAS*; Walter de Gruyter GmbH & Co KG, **2018**.
(151) Coelho, A. A. TOPAS and TOPAS-Academic: An Optimization Program Integrating Computer Algebra and Crystallographic Objects Written in C++. *J. Appl. Cryst.* **2018**, *51* (1), 210–218.
(152) Lefmann, K. *Neutron Scattering: Theory, Instrumentation, and Simulation*. Niels Bohr Institute, University of Copenhagen, **2017**.
(153) Cousin, F. Small Angle Neutron Scattering. *EPJ Web of Conferences,* **2015**, *104*, 01004.
(154) Cousin, F.; Gummel, J.; Clemens, D.; Grillo, I.; Boué, F. Multiple Scale Reorganization of Electrostatic Complexes of Poly(Styrenesulfonate) and Lysozyme. *Langmuir,* **2010**, *26* (10), 7078–7085.
(155) Glinka, C. J.; Barker, J. G.; Hammouda, B.; Krueger, S.; Moyer, J. J.; Orts, W. J. The 30 m Small-Angle Neutron Scattering Instruments at the National Institute of Standards and Technology. *J. Appl. Cryst.* **1998**, *31* (3), 430–445.
(156) Geerits, N.; Parnell, S. R.; Thijs, M. A.; van Well, A. A.; Franz, C.; Washington, A. L.; Raspino, D.; Dalgliesh, R. M.; Plomp, J. Time of Flight Modulation of Intensity by Zero Effort on Larmor. *Rev. Sci. Instrum.* **2019**, *90* (12), 125101.
(157) Banhart, J.; Borbély, A.; Dzieciol, K.; Garcia-Moreno, F.; Manke, I.; Kardjilov, N.; Kaysser-Pyzalla, A. R.; Strobl, M.; Treimer, W. X-Ray and Neutron Imaging – Complementary Techniques for Materials Science and Engineering. *IJMR,* **2010**, *101* (9), 1069–1079.
(158) Banhart, J. *Advanced Tomographic Methods in Materials Research and Engineering*; Monographs on the Physics and Chemistry of Materials; Oxford University Press: Oxford, New York, **2008**.
(159) Strobl, M.; Manke, I.; Kardjilov, N.; Hilger, A.; Dawson, M.; Banhart, J. Advances in Neutron Radiography and Tomography. *J. Phys. D: Appl. Phys.* **2009**, *42* (24), 243001.
(160) Hassanein, R.; de Beer, F.; Kardjilov, N.; Lehmann, E. Scattering Correction Algorithm for Neutron Radiography and Tomography Tested at Facilities with Different Beam Characteristics. *Physica B Condens. Matter,* **2006**, *385–386*, 1194–1196.
(161) Bücherl, T.; Söllradl, S. NECTAR: Radiography and Tomography Station Using Fission Neutrons. *J. large-scale res. facilities JLSRF,* **2015**, *1* (0), 19.
(162) Berdiyeva, P.; Karabanova, A.; Makowska, M. G.; Johnsen, R. E.; Blanchard, D.; Hauback, B. C.; Deledda, S. In-Situ Neutron Imaging Study of NH_3 Absorption and Desorption in $SrCl_2$ within a Heat Storage Prototype Reactor. *J. Energy Storage,* **2020**, *29*, 101388.
(163) Tötzke, C.; Kardjilov, N.; Lenoir, N.; Lenoir, N.; Manke, I.; Oswald, S. E.; Tengattini, A.; Tengattini, A. What Comes NeXT? High-Speed Neutron Tomography at ILL. *Opt. Express, OE* **2019**, *27* (20), 28640–28648.

(164) Schneider, C. A.; Rasband, W. S.; Eliceiri, K. W. NIH Image to ImageJ: 25 Years of Image Analysis. *Nat. Methods,* **2012**, *9* (7), 671–675.
(165) Rueden, C. T.; Schindelin, J.; Hiner, M. C.; DeZonia, B. E.; Walter, A. E.; Arena, E. T.; Eliceiri, K. W. ImageJ2: ImageJ for the next Generation of Scientific Image Data. *BMC Bioinformatics,* **2017**, *18* (1), 529.
(166) Radioscopy & Tomography systems | RX Solutions https://www.rxsolutions.fr/x-act (accessed May 11, 2020).
(167) Kaestner, A. P. MuhRec—A New Tomography Reconstructor. *Nuclear Instruments and Methods in Physics Research Section A: Accelerators, Spectrometers, Detectors and Associated Equipment,* **2011**, *651* (1), 156–160.
(168) Hanwell, M. D.; Harris, C. J.; Genova, A.; Schwartz, J.; Jiang, Y.; Hovden, R. Tomviz: Open Source Platform Connecting Image Processing Pipelines to GPU Accelerated 3D Visualization. *Microsc. Microanal.* **2019**, *25* (S2), 408–409.
(169) VGSTUDIO MAX: High-End Software for CT Data https://www.volumegraphics.com/en/products/vgstudio-max.html (accessed May 11, 2020).
(170) Kardjilov, N.; Manke, I.; Hilger, A.; Strobl, M.; Banhart, J. Neutron Imaging in Materials Science. *Mater. Today,* **2011**, *14* (6), 248–256.
(171) Kardjilov, N.; Manke, I.; Woracek, R.; Hilger, A.; Banhart, J. Advances in Neutron Imaging. *Mater. Today,* **2018**, *21* (6), 652–672.
(172) Herwig, K. W. Introduction to the Neutron. In *Neutron Imaging and Applications: A Reference for the Imaging Community*; Bilheux, H. Z., McGreevy, R., Anderson, I. S., Eds.; Neutron Scattering Applications and Techniques; Springer US: Boston, MA, **2009**; pp 3–12.
(173) Kardjilov, N.; Alii, E. Neutron Tomography in Modern Archaeology. *Notiziario: neutroni e luce di sincrotrone,* **2008**, *13* (2), 6–9.
(174) Fedrigo, A.; Strobl, M.; Williams, A. R.; Lefmann, K.; Lindelof, P. E.; Jørgensen, L.; Pentz, P.; Bausenwein, D.; Schillinger, B.; Kovyakh, A.; Grazzi, F. Neutron Imaging Study of 'Pattern-Welded' Swords from the Viking Age. *Archaeol. Anthropol. Sci.* **2018**, *10* (6), 1249–1263.
(175) Watkin, K. L.; Bilheux, H. Z.; Ankner, J. F. Probing the Potential of Neutron Imaging for Biomedical and Biological Applications. In *Neutron Imaging and Applications: A Reference for the Imaging Community*; Bilheux, H. Z., McGreevy, R., Anderson, I. S., Eds.; Neutron Scattering Applications and Techniques; Springer US: Boston, MA, **2009**; pp 253–264.
(176) Matsushima, U.; Herppich, W. B.; Kardjilov, N.; Graf, W.; Hilger, A.; Manke, I. Estimation of Water Flow Velocity in Small Plants Using Cold Neutron Imaging with D_2O Tracer. *Nuclear Instruments and Methods in Physics Research Section A: Accelerators, Spectrometers, Detectors and Associated Equipment,* **2009**, *605* (1), 146–149.
(177) Griesche, A.; Dabah, E.; Kannengiesser, T.; Kardjilov, N.; Hilger, A.; Manke, I. Three-Dimensional Imaging of Hydrogen Blister in Iron with Neutron Tomography. *Acta Mater.* **2014**, *78*, 14–22.
(178) Griesche, A.; Dabah, E.; Kannengiesser, T.; Hilger, A.; Kardjilov, N.; Manke, I.; Schillinger, B. Measuring Hydrogen Distributions in Iron and Steel Using Neutrons. *Phys. Procedia,* **2015**, *69*, 445–450.
(179) Gondek, Ł.; Selvaraj, N. B.; Czub, J.; Figiel, H.; Chapelle, D.; Kardjilov, N.; Hilger, A.; Manke, I. Imaging of an Operating $LaNi_{4.8}Al_{0.2}$–Based Hydrogen Storage Container. *Int. J. Hydrog. Energy,* **2011**, *36* (16), 9751–9757.

(180) Herbrig, K.; Pohlmann, C.; Gondek, Ł.; Figiel, H.; Kardjilov, N.; Hilger, A.; Manke, I.; Banhart, J.; Kieback, B.; Röntzsch, L. Investigations of the Structural Stability of Metal Hydride Composites by In-Situ Neutron Imaging. *J. Power Sources,* **2015**, *293*, 109–118.
(181) Pohlmann, C.; Herbrig, K.; Gondek, Ł.; Kardjilov, N.; Hilger, A.; Figiel, H.; Banhart, J.; Kieback, B.; Manke, I.; Röntzsch, L. In Operando Visualization of Hydride-Graphite Composites during Cyclic Hydrogenation by High-Resolution Neutron Imaging. *J. Power Sources,* **2015**, *277*, 360–369.
(182) Hartnig, C.; Roth, C. *Polymer Electrolyte Membrane and Direct Methanol Fuel Cell Technology: Volume 2: In Situ Characterization Techniques for Low Temperature Fuel Cells*; Elsevier, **2012**.
(183) Arlt, T.; Lüke, W.; Kardjilov, N.; Banhart, J.; Lehnert, W.; Manke, I. Monitoring the Hydrogen Distribution in Poly(2,5-Benzimidazole)-Based (ABPBI) Membranes in Operating High-Temperature Polymer Electrolyte Fuel Cells by Using H-D Contrast Neutron Imaging. *J. Power Sources,* **2015**, *299*, 125–129.
(184) Schröder, A.; Wippermann, K.; Arlt, T.; Sanders, T.; Baumhöfer, T.; Kardjilov, N.; Mergel, J.; Lehnert, W.; Stolten, D.; Banhart, J.; Manke, I. In-Plane Neutron Radiography for Studying the Influence of Surface Treatment and Design of Cathode Flow Fields in Direct Methanol Fuel Cells. *Int. J. Hydrog. Energy,* **2013**, *38* (5), 2443–2454.
(185) Satija, R.; Jacobson, D. L.; Arif, M.; Werner, S. A. In Situ Neutron Imaging Technique for Evaluation of Water Management Systems in Operating PEM Fuel Cells. *J. Power Sources,* **2004**, *129* (2), 238–245.
(186) Kramer, D.; Zhang, J.; Shimoi, R.; Lehmann, E.; Wokaun, A.; Shinohara, K.; Scherer, G. G. In Situ Diagnostic of Two-Phase Flow Phenomena in Polymer Electrolyte Fuel Cells by Neutron Imaging: Part A. Experimental, Data Treatment, and Quantification. *Electrochim. Acta,* **2005**, *50* (13), 2603–2614.
(187) Mauran, S.; Coudevylle, O.; Lu, H. B. Optimization of Porous Reactive Media for Solid Sorption Heat Pumps | ETDEWEB. In *Proc. Int. Sorption Heat Pump Conference*; Canada, Montreal, **1996**; pp 3–8.
(188) Tamainot-Telto, Z.; Critoph, R. E. Monolithic Carbon for Sorption Refrigeration and Heat Pump Applications. *Appl. Therm. Eng.* **2001**, *21* (1), 37–52.
(189) Jiang, L.; Wang, L. W.; Jin, Z. Q.; Wang, R. Z.; Dai, Y. J. Effective Thermal Conductivity and Permeability of Compact Compound Ammoniated Salts in the Adsorption/Desorption Process. *Int. J. Therm. Sci.* **2013**, *71*, 103–110.
(190) Tian, B.; Jin, Z. Q.; Wang, L. W.; Wang, R. Z. Permeability and Thermal Conductivity of Compact Chemical and Physical Adsorbents with Expanded Natural Graphite as Host Matrix. *Int. J. Heat Mass Transf.* **2012**, *55* (15), 4453–4459.
(191) Wang, L. W.; Tamainot-Telto, Z.; Metcalf, S. J.; Critoph, R. E.; Wang, R. Z. Anisotropic Thermal Conductivity and Permeability of Compacted Expanded Natural Graphite. *Appl. Therm. Eng.* **2010**, *30* (13), 1805–1811.
(192) Han, J. H.; Lee, K.-H. Gas Permeability of Expanded Graphite–Metallic Salt Composite. *Appl. Therm. Eng.* **2001**, *21* (4), 453–463.
(193) Wang, K.; Wu, J. Y.; Wang, R. Z.; Wang, L. W. Effective Thermal Conductivity of Expanded Graphite–$CaCl_2$ Composite Adsorbent for Chemical Adsorption Chillers. *Energy Convers. Manag.* **2006**, *47* (13), 1902–1912.

(194) Sanchez-Fernandez, A.; J. Edler, K.; Arnold, T.; K. Heenan, R.; Porcar, L.; J. Terrill, N.; E. Terry, A.; J. Jackson, A. Micelle Structure in a Deep Eutectic Solvent: A Small-Angle Scattering Study. *Phys. Chem. Chem. Phys.* **2016**, *18* (20), 14063–14073.
(195) Sanchez-Fernandez, A.; L. Moody, G.; C. Murfin, L.; Arnold, T.; J. Jackson, A.; M. King, S.; E. Lewis, S.; J. Edler, K. Self-Assembly and Surface Behaviour of Pure and Mixed Zwitterionic Amphiphiles in a Deep Eutectic Solvent. *Soft Matter,* **2018**, *14* (26), 5525–5536.
(196) Cavallaro, G.; Chiappisi, L.; Gradzielski, M.; Lazzara, G. Effect of the Supramolecular Interactions on the Nanostructure of Halloysite/Biopolymer Hybrids: A Comprehensive Study by SANS, Fluorescence Correlation Spectroscopy and Electric Birefringence. *Phys. Chem. Chem. Phys.* **2020**, *22* (15), 8193–8202.
(197) Huang, A.; Yao, H.; D. Olsen, B. SANS Partial Structure Factor Analysis for Determining Protein–Polymer Interactions in Semidilute Solution. *Soft Matter,* **2019**, *15* (37), 7350–7359.
(198) Hattendorff, J.; Seidlmayer, S.; Gasteiger, H. A.; Gilles, R. Li-Ion Half-Cells Studied Operando during Cycling by Small-Angle Neutron Scattering. *J. Appl. Cryst.* **2020**, *53* (1), 210–221.
(199) Aslan, N.; Horstmann, C.; Metz, O.; Kotlyar, O.; Dornheim, M.; Pistidda, C.; Busch, S.; Lohstroh, W.; Müller, M.; Pranzas, K. High-Pressure Cell for in Situ Neutron Studies of Hydrogen Storage Materials. *J. Neutron Res.* **2019**, *21* (3–4), 125–135.
(200) Lai, S. Y.; Knudsen, K. D.; Sejersted, B. T.; Ulvestad, A.; Mæhlen, J. P.; Koposov, A. Y. Silicon Nanoparticle Ensembles for Lithium-Ion Batteries Elucidated by Small-Angle Neutron Scattering. *ACS Appl. Energy Mater.* **2019**, *2* (5), 3220–3227.
(201) Paul, N.; Wetjen, M.; Busch, S.; Gasteiger, H.; Gilles, R. Contrast Matched SANS for Observing SEI and Pore Clogging in Silicon-Graphite Anodes. *J. Electrochem. Soc.* **2019**, *166* (6), A1051–A1054.
(202) Wang, H.; Downing, R. G.; Dura, J. A.; Hussey, D. S. In Situ Neutron Techniques for Studying Lithium Ion Batteries. In *Polymers for Energy Storage and Delivery: Polyelectrolytes for Batteries and Fuel Cells*; ACS Symposium Series; American Chemical Society, **2012**; Vol. 1096, pp 91–106.
(203) Ren, Y.; Zuo, X. Synchrotron X-Ray and Neutron Diffraction, Total Scattering, and Small-Angle Scattering Techniques for Rechargeable Battery Research. *Small Methods* **2018**, *2* (8), 1800064.
(204) Fratzl, P.; IUCr. Small-angle scattering in materials science. https://scripts.iucr.org/cgi-bin/paper?ks7206 (accessed May 12, 2020).
(205) Berdiyeva, P.; Karabanova, A.; Grinderslev, J. B.; Johnsen, R. E.; Blanchard, D.; Hauback, B. C.; Deledda, S. Synthesis, Structure and NH_3 Sorption Properties of Mixed $Mg_{1-x}Mn_x(NH_3)_6Cl_2$ Ammines. *Energies,* **2020**, *13* (11), 2746.
(206) Reardon, H.; Hanlon, J. M.; Grant, M.; Fullbrook, I.; Gregory, D. H. Ammonia Uptake and Release in the MnX_2–NH_3 (X = Cl, Br) Systems and Structure of the $Mn(NH_3)_nX_2$ (n = 6, 2) Ammines. *Crystals* **2012**, *2* (2), 193–212.

Publications

Publication I

In-situ neutron imaging study of NH_3 absorption and desorption in $SrCl_2$ within a heat storage prototype reactor

P. Berdiyeva, A. Karabanova, M. G. Makowska, R. E. Johnsen, D. Blanchard, B. C. Hauback and S. Deledda

Journal of Energy Storage, **2020**, 29, 101388.

Graphical abstract

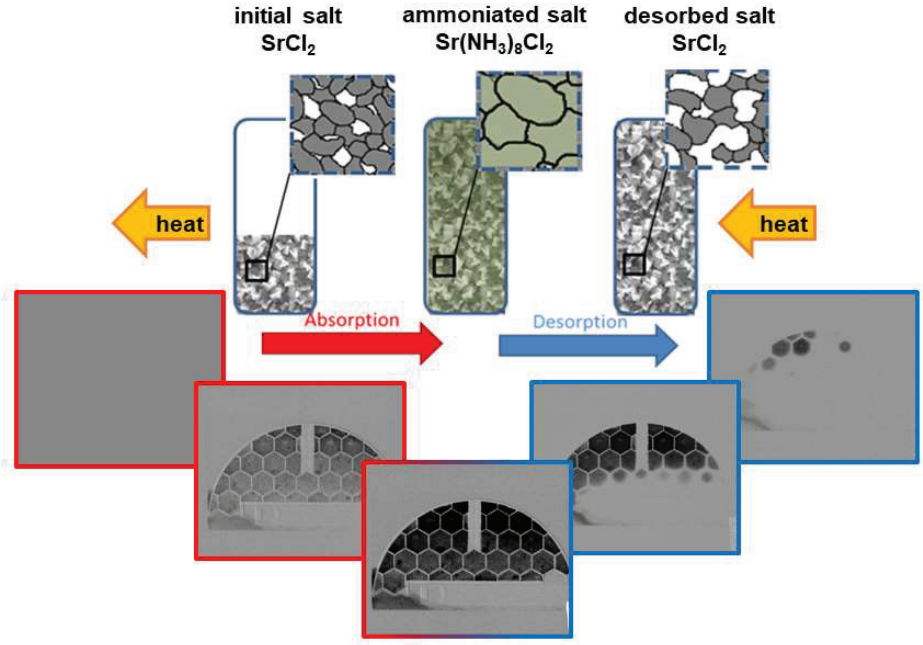

Journal of Energy Storage 29 (2020) 101388

Contents lists available at ScienceDirect

Journal of Energy Storage

journal homepage: www.elsevier.com/locate/est

In-situ neutron imaging study of NH_3 absorption and desorption in $SrCl_2$ within a heat storage prototype reactor

Perizat Berdiyeva[a], Anastasiia Karabanova[b], Malgorzata G. Makowska[c], Rune E. Johnsen[b], Didier Blanchard[b], Bjørn C. Hauback[a], Stefano Deledda[a,*]

[a] Department for Neutron Materials Characterization, Institute for Energy Technology, P.O. Box 40, NO-2027, Kjeller, Norway
[b] Department of Energy Conversion and Storage, Technical University of Denmark, Fysikvej, DK-2800, Lyngby, Denmark
[c] Photon Science Division, Paul-Scherrer Institute, Forschungsstrasse 111, 5232-Villigen, Switzerland

ARTICLE INFO

Keywords:
Metal halides
Heat storage
Ammonia absorption/desorption
Neutron radiography
Neutron tomography

ABSTRACT

Strontium chloride octaammine $Sr(NH_3)_8Cl_2$ offers high volumetric and gravimetric NH_3 densities and can store and release heat upon exo-/endothermal absorption and desorption of NH_3. Thus, it is a promising material for thermochemical heat storage (THS) applications.

In the present work, *in-situ* neutron imaging was applied to analyze spatio-temporal development of $Sr(NH_3)_8Cl_2$ powder in a thermochemical heat storage prototype reactor during NH_3 absorption and desorption processes. The powder was embedded in a stainless steel honeycomb for the efficient heat transfer during the NH_3 desorption process. 2D radiography images were obtained during NH_3 ab-/desorption cycles at selected temperatures. The swelling and formation of the porous structure in $SrCl_2$ is monitored during the first cycles. A powder bed expansion of up to 10% upon NH_3 absorption was observed. Neutron tomography experiment were also performed to acquire 3D information which revealed the deformation of the honeycomb. This neutron imaging experiment brought crucial information for optimizing the design of efficient and safe THS systems.

1. Introduction

To support the transition from conventional fossil fuel energy sources to decarbonized sources, a number of technologies have been identified and are expected to have major impacts. The technologies range from renewable energy sources to efficient energy use, where the excess of energy can be first stored and later supplied to meet the demands. The effective use of energy requires efficient storage, which can be achieved using different methods one of them being thermal energy storage [1]. Seasonal heat storage materials such as hydrates [2] and ammines have been studied as thermochemical heat storage materials for domestic heating applications [3]. However, most hydrates were found to have poor cyclability and degrade over multiple cycles at temperature higher than 50 °C [4]. Meanwhile sorption metal chloride and ammonia working pairs are reported to have a very good cyclability and high energy density [5].

Metal ammines have for more than 15 years been studied as an indirect storage of hydrogen due to their high volumetric and gravimetric hydrogen capacities [6–8]. $Sr(NH_3)_8Cl_2$ is one of the best metal halide ammines for NH_3 storage due to its high hydrogen density [9] and high theoretical volumetric NH_3 density of 642 kg m^{-3} at RT [10]. It is obtained via absorption of NH_3 into $SrCl_2$. The absorption reaction is exothermic, while the endothermic desorption is achieved by applying heat. These exothermic and endothermic absorption and desorption reactions are associated with good kinetics and make the $SrCl_2$/$Sr(NH_3)_8Cl_2$ an interesting system for thermochemical heat storage (THS) applications [10,11]. In these applications, heat provided by an external source decomposes $Sr(NH_3)_8Cl_2$ into NH_3 gas and $SrCl_2$. The NH_3 gas can then be condensed into liquid NH_3 in a separate reservoir. In storage mode the connection between liquid NH_3 and $SrCl_2$ is closed. To recover the heat, NH_3 is transferred back to the container with $SrCl_2$, where heat is released upon the absorption process and formation of $Sr(NH_3)_8Cl_2$. By controlling the applied pressure of the NH_3 gas, the heat release can be controlled and varied. Ideally, the exothermal and endothermal absorption and desorption of NH_3 in $SrCl_2$ / $Sr(NH_3)_8Cl_2$ can be employed for handling waste heat (40–80 °C) from industry and be reused for district heating [1]. The $SrCl_2/NH_3$ working pair was selected due to its high energy density and very good cyclability. $SrCl_2$ is rather cheap and non-toxic. Its working temperature corresponds to the target application, i.e. residential heating, taking advantage of low-price renewable electricity (heat-pump + heat storage) and / or low-grade waste heat recovery (<100 °C) readily available at most

* Corresponding author.
E-mail address: stefano.deledda@ife.no (S. Deledda).

https://doi.org/10.1016/j.est.2020.101388
Received 12 December 2019; Received in revised form 24 February 2020; Accepted 19 March 2020

industrial production lines.

The crystal structures of $Sr(NH_3)_8Cl_2$, $SrCl_2$ and their intermediates have already been extensively studied and characterized [9,10]. However, the spatio-temporal evolution of the $Sr(NH_3)_8Cl_2$ and NH_3 transport in the system have not yet been investigated in detail. Neutrons are very well suited to determine the distribution of NH_3 molecules in the $SrCl_2/Sr(NH_3)_8Cl_2$ system due to their unique properties of "seeing" hydrogen atoms and to the high hydrogen content in this system.

Neutron imaging is a powerful characterization technique which can provide 2D and 3D information about the inner structure of objects [12]. It is used as a characterization method for various energy storage materials and systems. The strong interaction of neutrons with hydrogen makes neutrons an attractive probe within hydrogen storage, where neutron radiography and tomography techniques can be used not only for qualitative, but also quantitative studies [13–16]. Furthermore, energy storage devices such as fuel cells or batteries are studied extensively by neutron imaging. The sensitivity of neutrons to hydrogen in water molecules allows detecting and visualizing water distribution in fuel cells [17–20]. Neutrons are also sensitive to lithium, which is a key element in commercial rechargeable batteries [21–25]. Further details about neutron imaging techniques, its accuracy, sensitivity, and its applications in various fields of research can be found in several review papers published in the last decade [12,26,27].

In this work, NH_3 uptake and release in the $SrCl_2/Sr(NH_3)_8Cl_2$ system within a THS prototype reactor, was studied by neutron imaging. The specially designed THS prototype reactor contained $SrCl_2$ embedded in a stainless steel honeycomb structure. The designed THS reactor contains several honeycomb discs filled with $SrCl_2$ powder, which are placed on top of each other. In this work only the half of one whole disc was employed in order to examine the local NH_3 absorption and desorption. The honeycomb structure of the disc is used to provide an efficient heat transfer within the volume of the disc during the NH_3 desorption process, when heat is provided to the system. The high neutron scattering cross-section of hydrogen present in ammonia molecule allowed observation of the uptake and release of NH_3 within $SrCl_2$. Absorption and desorption profiles for different regions of the honeycomb were obtained for each absorption and desorption cycle by *in-situ* neutron radiography. The results of image analysis are discussed with respect to the homogeneity of the absorption and desorption processes over the volume of the THS reactor and how it is affected by the degree of the compaction of the powder, as well as how efficiently the stainless-steel honeycomb structure conducts the heat during NH_3 desorption.

To the best of our knowledge this is the first time that neutron imaging is used to characterize a THS reactor, allowing a real-time visualization of the changes that the sorption material undergoes during charging and discharging. The neutron radiography data presented here will be used to validate results from numerical simulations. A COMSOL Multiphysics modelling was developed for the heat reactor, integrating, with a high degree of accuracy, the thermochemistry, the ammonia flow, the heat transfer to optimize the reactor design and achieve high heat power and maximum use of the heat generated [28]. Neutron imaging will help, on one hand, to validate the simulation model, and, on the other hand, to validate or invalidate our first assumption on the honeycomb effect on heat transfer and diffusion to the salt.

2. Experimental

2.1. The THS reactor prototype set-up

A special transportable THS reactor prototype (118 mm in length, 20 mm in width and 85 mm in height) was designed for the neutron imaging experiment (Fig. 1). The THS reactor is made of 2 mm thick aluminum, in order to be as transparent as possible for neutrons to study the interior of the reactor. The THS reactor is tightly closed with a stainless-steel lid of 85 mm in diameter and an o-ring ensured the sealing. The lid had two gas inlets (only one of them was used during this experiment) and a cylindrical inlet which housed a heating element and a thermocouple.

A honeycomb with the dimensions of 100 × 50 × 10 mm was filled with 10 g of $SrCl_2$ salt and placed inside the THS reactor in an inert argon gas filled glove box (<1 ppm of O_2 and H_2O). Two absorption and desorption cycles were performed on the $SrCl_2$ prior to the neutron imaging experiment in order to confirm the cyclability and suitability of the sample. The THS reactor was then connected through a stainless-steel tube to a reservoir, which contained 100 g of $Sr(NH_3)_8Cl_2$ powder that served as NH_3 source and reservoir during the experiment. Manual valves and a pressure reader (Fig. 2) were included in the connection between the THS reactor and the reservoir. The reservoir and the prototype reactor were connected to a heating element and a thermocouple for controlling and monitoring the temperature.

The $Sr(NH_3)_8Cl_2$ in the reservoir was heated up to 70 °C during the experiment which then released NH_3 gas that was absorbed by the $SrCl_2$ salt in the honeycomb at RT. Upon heating the honeycomb in the THS reactor, NH_3 was released from the $Sr(NH_3)_8Cl_2$ powder and reabsorbed in the reservoir. The pressure of the system was remotely monitored and logged.

2.2. Neutron imaging set-up

The neutron radiography and tomography experiments were performed at the NECTAR instrument, at the FRM-II research reactor in Garching, Germany using a white beam of thermal neutrons (mean energy 28 meV) [29]. The sample was mounted on a stage allowing translation along *x, y* and *z*-axes about 3 cm in case of radiography and about 10 cm for tomography from the scintillator screen. The thermal neutron beam transmitted through the sample impinged on a scintillator screen $ZnS/^6LiF$, which converted the neutrons into light. The light was then reflected by a mirror in a light-tight box and captured by CCD camera (Andor iKon-L-BV) with a 2048 × 2048 pixels resolution. The experiment did not require high spatial resolution, thus the collimation ratio L/D, which was about 230, provided sufficient image quality. Prior to each experiment open beam and dark current images were collected for normalization of the raw images using ImageJ [30]. The total acquisition time for each image including camera readout was 27 s and overall three absorption and two desorption processes were performed. Each absorption step, except the last one, was followed by desorption allowing us to investigate not only the absorption and desorption processes themselves, but also the difference between the first and next cycles. The honeycomb with $SrCl_2$ powder was open in the front side for free NH_3 and $SrCl_2$ powder interaction.

Neutron tomography measurements were carried out by placing the THS reactor in a vertical position and by rotating it over a 360° range. During the tomography experiment the THS reactor was disconnected from the reservoir. Several tomography scans, each with 1083 projections, were performed for different degrees of saturation of NH_3 in $Sr(NH_3)_8Cl_2$ and then 3D volume of the sample was reconstructed using MuhRec software [31] and visualized using Tomviz software [32].

The formation of $Sr(NH_3)_8Cl_2$, thus NH_3 concentration in the sample was defined by the normalized transmission $I(\lambda)$ (greyscale values between 0 and 1) in selected areas of the images, where I is the normalized intensity and λ is the neutron wavelength. The lower transmission $I(\lambda)$ represents the higher concentration of NH_3 while the higher transmission $I(\lambda)$ means lower NH_3 content in the sample.

3. Results and discussion

3.1. Absorption process

In-situ transmission images were obtained during NH_3 absorption and desorption processes in the $SrCl_2$ powder. The series of images in Fig. 3 show the honeycomb at the end of absorption-1 (a), absorption-2

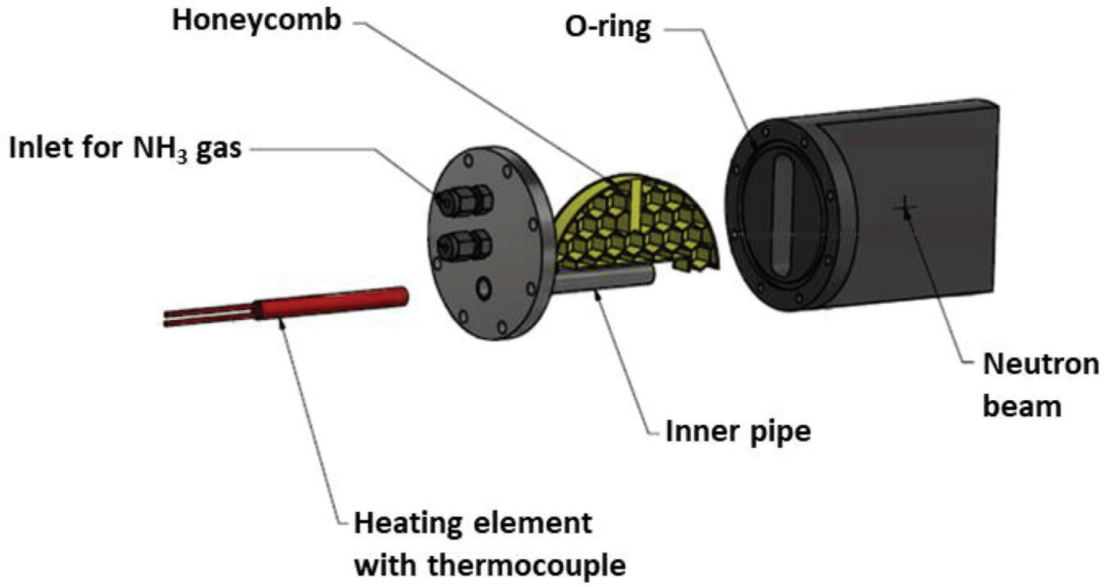

Fig. 1. Detailed view of the THS prototype reactor with the honeycomb inside.

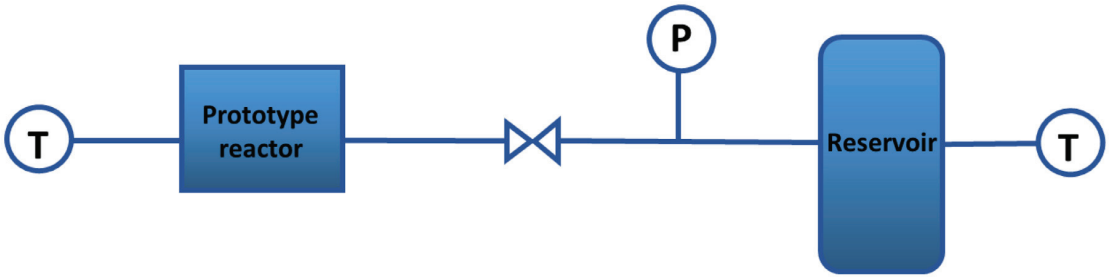

Fig. 2. Schematic view of the setup used for the neutron imaging experiment. The letters P and T indicate the points where pressure and temperature were measured.

(b) and absorption-3 (c). These images were obtained by normalization of corresponding images by the image of the sample in the initial state. Therefore, the images show only the changes that occurred in the sample due to NH_3 absorption. The formation of $Sr(NH_3)_8Cl_2$ appears as dark areas during NH_3 uptake due to the high neutron attenuation of hydrogen atoms [19] contained in ammonia molecules.

The different transmission $I(\lambda)$ at the end of each NH_3 absorption process suggests a different extent of NH_3 uptake (see Fig. 3). Transmission values $I(\lambda)$ were obtained by marking a hexagonal area in one cell of the honeycomb (cell-1, Fig. 4a) and calculating the mean value over the selected area. Fig. 4a presents the mean $I(\lambda)$ change over time in this cell. The graph shows a clear difference in transmission between the absorption-1, absorption-2 and absorption-3. During absorption-3, a lower greyscale value of 0.357 was reached compared to the absorption-1 and absorption-2, where the greyscale values were 0.622 and 0.551 at the end of absorption, respectively. This is the result of powder expansion during the NH_3 absorption processes and formation of macroporous structure [9], which creates paths for more NH_3 to diffuse into the powder bed during the following absorption processes. For this reason, absorption-2 and absorption-3 resulted in more ammoniated areas in the radiography images than those observed in absorption-1 (Fig. 3). However, as seen in Fig. 4, the change in the transmission $I(\lambda)$ with time, for a given absorption, does not stabilize to minimal values suggesting that the absorption processes were not completed.

The pressure in the system was monitored during the NH_3 absorption (see Fig. 4b). As the reservoir was heated and NH_3 was released

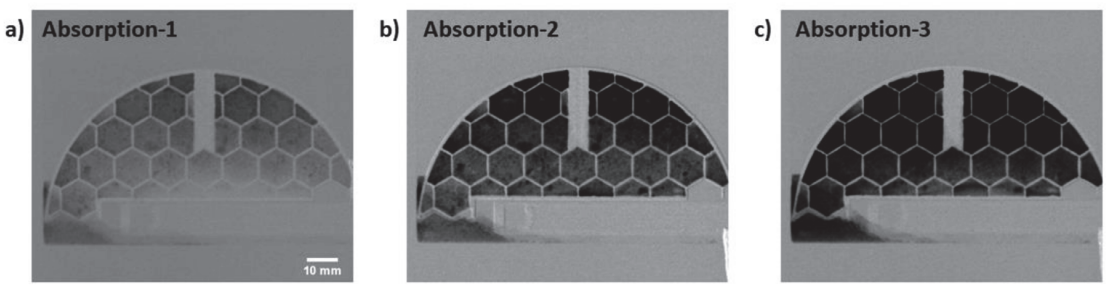

Fig. 3. Neutron radiography images. The series of normalized images representing the sample after each absorption process (**a)** absorption-1, (**b)** absorption-2 and (**c)** absorption-3.

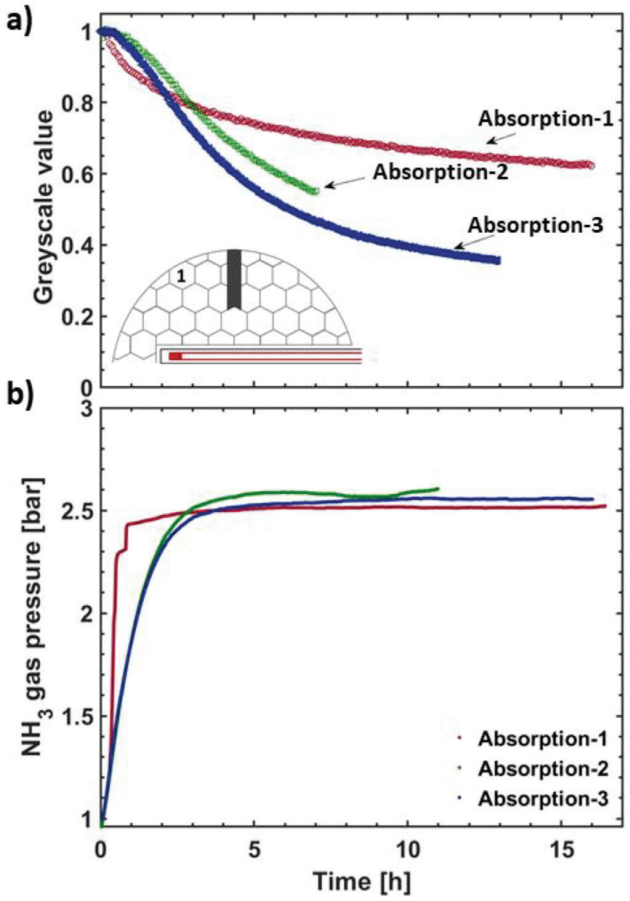

Fig. 4. NH_3 gas absorption in $SrCl_2$ contained in the THS reactor. (**a**) the change in transmission $I(\lambda)$ in the cell-1 and (**b**) NH_3 gas pressure during the absorption processes.

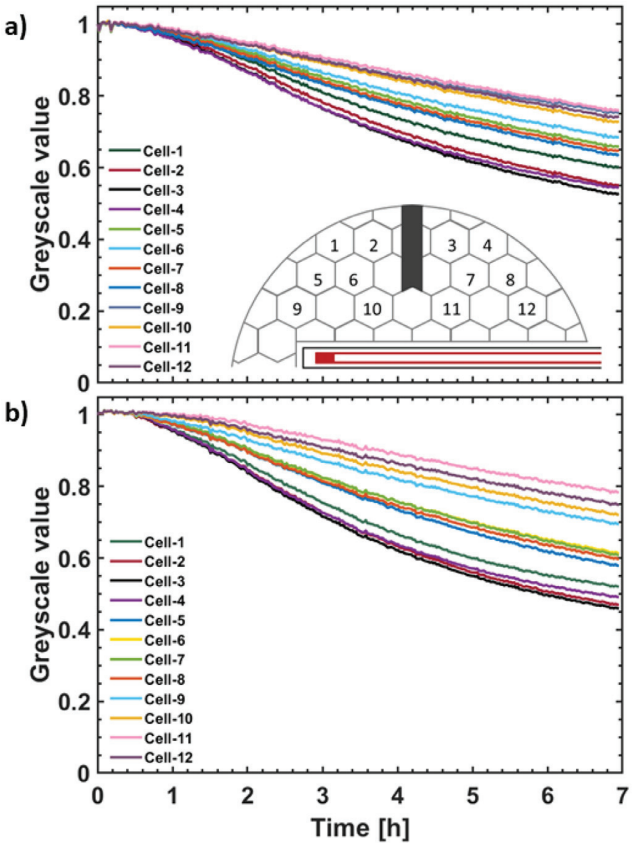

Fig. 5. The change in transmission $I(\lambda)$ through the powder during (**a**) absorption-2 and (**b**) absorption-3. The schematic view of the honeycomb with selected and numbered cells is included in graph a.

from the $Sr(NH_3)_8Cl_2$ salt in the reservoir, the pressure of the system increased to 2.5 bar, which is the equilibrium pressure of $Sr(NH_3)_8Cl_2$ at 70 °C. Once the NH_3 absorption process started in the THS reactor, the pressure was stabilized due to the equal rate of NH_3 release from Sr $(NH_3)_8Cl_2$ in the reservoir and the NH_3 absorption by $SrCl_2$ in the THS honeycomb structure.

A more detailed analysis of the $Sr(NH_3)_8Cl_2$ formation during absorption-2 and absorption-3 was performed on selected cells of the honeycomb. Mean transmission values $I(\lambda)$ were calculated by averaging over the area of the selected cells during the first 7 h of absorption. The results are plotted in Fig. 5 for absorption-2 (a) and absorption-3 (b), respectively. It can be observed that the formation of Sr $(NH_3)_8Cl_2$ is inhomogeneous over the honeycomb volume. The NH_3 distribution in the different cells of the honeycomb differs depending on their position within the honeycomb. Fig. 5a shows that the topmost cells have the lowest mean greyscale value (higher concentration of NH_3) between 0.603 and 0.528 (cell-1, -2, -3 and -4) whereas the cells in the bottom (cell-9, -10, -11 and -12) have higher mean greyscale values (lower concentration of NH_3) between 0.756 and 0.744. The same trend can be seen during the third absorption process (Fig. 5b). The lowest mean greyscale value calculated was 0.459 in the cell-3, whereas the highest value was 0.783 in the cell-11. Cell-5, -6, -7 and -8 located in the middle of the honeycomb show intermediate mean greyscale value between 0.579 and 0.613, which means that the NH_3 concentration in those cells is the intermediate between the NH_3 concentration in the top and bottom cells.

Several reasons might contribute to these results. Firstly, it should be noted that the NH_3 gas inlet was placed at the top right of the THS reactor, letting the powder particles on top cells absorb NH_3 gas earlier than the powder contained in the lower cells. Secondly, the free space between the THS reactor inner walls and the honeycomb allowed some powder to fall out of the honeycomb. Therefore, the powder thickness over the honeycomb was inhomogeneous, providing different amount of $SrCl_2$ salt in the different cells of the honeycomb and resulting in different NH_3 concentration. Finally, the honeycomb with the salt was prepared in an inert argon atmosphere, which filled the THS reactor prior to the start of the experiment. The THS reactor was not evacuated before the first NH_3 absorption process, so Ar gas was still present inside the reactor during absorption. The different densities of Ar and NH_3 gases, 1.661 kg/m^3 and 0.717 kg/m^3 at RT, respectively, might have created layers of NH_3 gas on the top and Ar on the bottom, preventing a homogeneous NH_3 gas flow towards the bottom of the THS reactor.

The expansion of $Sr(NH_3)_8Cl_2$ over time during the NH_3 uptake was studied by placing the honeycomb horizontally so that powder thickness change is perpendicular to the neutron beam. Side-view images were obtained while performing a NH_3 absorption process. The volume expansion of the $Sr(NH_3)_8Cl_2$ powder within the honeycomb is shown in Fig. 6. The expansion of the $Sr(NH_3)_8Cl_2$ in axial direction with time can be observed. The packing within the honeycomb prevented the Sr $(NH_3)_8Cl_2$ powder from expanding in the radial direction, while free space between the honeycomb and THS reactor wall allowed the axial expansion. During this process NH_3 absorption over time produced a gradual expansion of the salt by up to 10% in height.

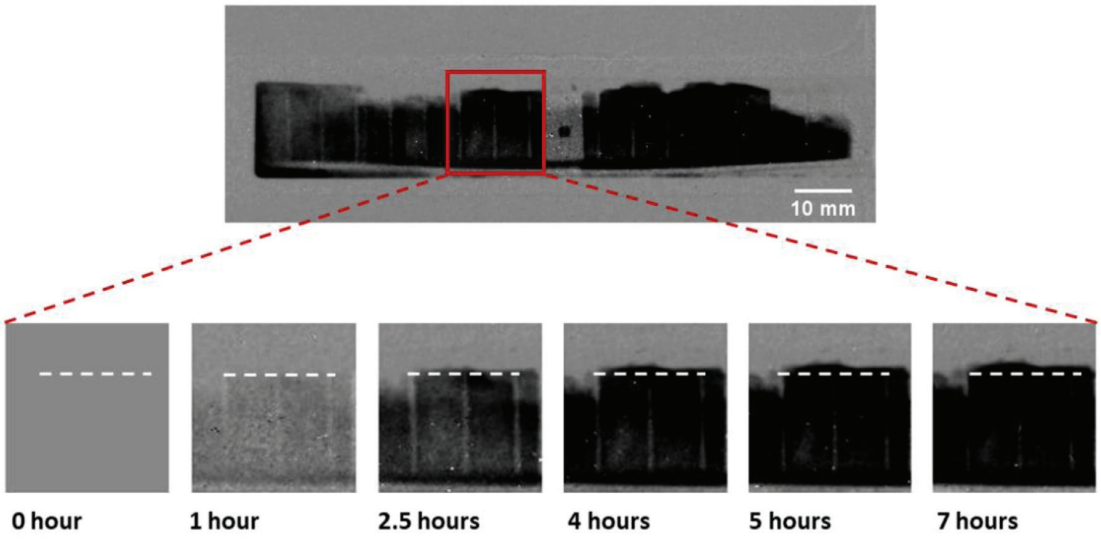

Fig. 6. Series of images showing the expansion of the salt during the NH_3 absorption process with time in selected area of the honeycomb. The white dashed line shows the initial height of the powder. (Full-size image above the series was acquired at the 4th hour of absorption-4).

3.2. Desorption process

Neutron radiography was carried out on the THS reactor during the desorption processes at selected temperatures. The two desorption processes were performed at 220 °C and 100 °C at 1 bar of ammonia pressure, and full release of NH_3 was observed after 46 min and 3 h 45 min, respectively. During desorption at 220 °C $Sr(NH_3)_8Cl_2$ was decomposed into $SrCl_2$ and NH_3, while at 100 °C the end products were $Sr(NH_3)Cl_2$ and NH_3. This is due to two-step desorption occurring in Sr $(NH_3)_8Cl_2$ at the given temperatures and ammonia pressure of 1 bar [6,9,10].

Fig. 7a and b show the change in transmission $I(\lambda)$ in the cell-1 and the pressure profile of the system during desorption processes. At 220 °C, the pressure increased drastically because of the large amount of NH_3 gas released in a short time and started decreasing after few minutes as NH_3 is absorbed in the reservoir. Fig. 7c and d show the transmission images of the honeycomb 20 min after the start of the desorption processes. The decomposition of $SrCl_2(NH_3)_8$ into $SrCl_2$ and NH_3 is almost complete after 20 min at 220 °C. The powder in the cells closer to the heat source desorbed NH_3 faster than the powder in cells further away from the heating source. It should be mentioned that the special stainless-steel honeycomb was prepared to provide a higher heat transfer. The hexagon-shaped cells should provide efficient heat transmission from cell to cell and thus improving the NH_3 desorption efficiency of the whole plate. The images in Fig. 7 show that heat conductivity of the stainless-steel was not sufficient for ensuring homogeneous NH_3 release. The NH_3 desorption process within all 12 cells was analyzed and included in the supplementary information (Fig. A.1).

In order to observe the NH_3 release in detail, selected cells of the honeycomb were analyzed. The rate of desorption in each cell volume was studied by drawing lines parallel to the hexagon edges and measuring the transmission $I(\lambda)$ integrated along those lines and plotted as a function of time (see Fig. 8). The lines are at distance of 2 mm from each edge of the hexagon. The NH_3 gas release over time at the sides of the cells gives us information about the heat efficiency of the total stainless-steel net since NH_3 release takes place only when $Sr(NH_3)_8Cl_2$ salt is heated.

Fig. 8a shows a schematic view of the honeycomb and three cells selected for investigation of the change of NH_3 concentration during the desorption process at 100 °C. Fig. 8b, c and d illustrate the drop of NH_3 content along the lines in the cell-2, 6 and 10, respectively.

In all three cells we see that the release of NH_3 is not uniform, and it changes according to the heat direction. The transmission through the absorbed NH_3 along the lines also strongly depends on the position of the analyzed area with respect to the relative distance from the heating element. The bottom-right edges, i.e. closer to the heat source (B, C and D) are those where NH_3 is released earlier, indicating that they are the first to be heated. On the other hand, the top-left ones (A, E and F) are those where NH_3 is released later, pointing out they are heated later. Overall, the desorption of NH_3 from powder in the top parts of one cell happens mainly because of the heat is transferred through the salt inside the cell rather than from the cell walls. Besides, full NH_3 release happened within 1.5 h in cell-10, which is the closest to the heating element, whereas NH_3 desorption was completed after about 3 and 3.5 h in cell-6 and cell-2, the furthest from the heat source, respectively. The different time for NH_3 release in different areas of the honeycomb indicates that the stainless steel is not an ideal material for the efficient heat transfer, as the desorption process is inhomogeneous both along the honeycomb and within each cell. Similar calculations for other cells were performed and are included as supplementary information (Fig. A.2).

3.3. Neutron tomography

Ex-situ tomography studies were performed on the THS reactor, which was disconnected from the reservoir and placed vertically in front of the neutron beam. 3D images of the THS reactor after one absorption and desorption cycle (Fig. 9a), after NH_3 absorption (Fig. 9b) and after partial NH_3 desorption (Fig. 9c) were obtained and visualized. A clear contrast between $Sr(NH_3)_8Cl_2$ and $SrCl_2$ can be observed. To visualize the partially desorbed state of the salt a desorption process during *in-situ* neutron radiography measurements was terminated after 30 min and the scan over 360° was performed on the sample.

In all 3D visualizations sample powders outside the honeycomb can be noticed. This was also observed in the series of images acquired during absorption and shown in the Fig. 3. The sample thickness irregularity in the honeycomb cells confirms that the powder was initially inside the cells. Each radiography/tomography switch during the experiments required the movement of the THS reactor from horizontal to vertical positions causing loose powder to fall from the honeycomb and movement of the honeycomb itself loosing contact with the heating element.

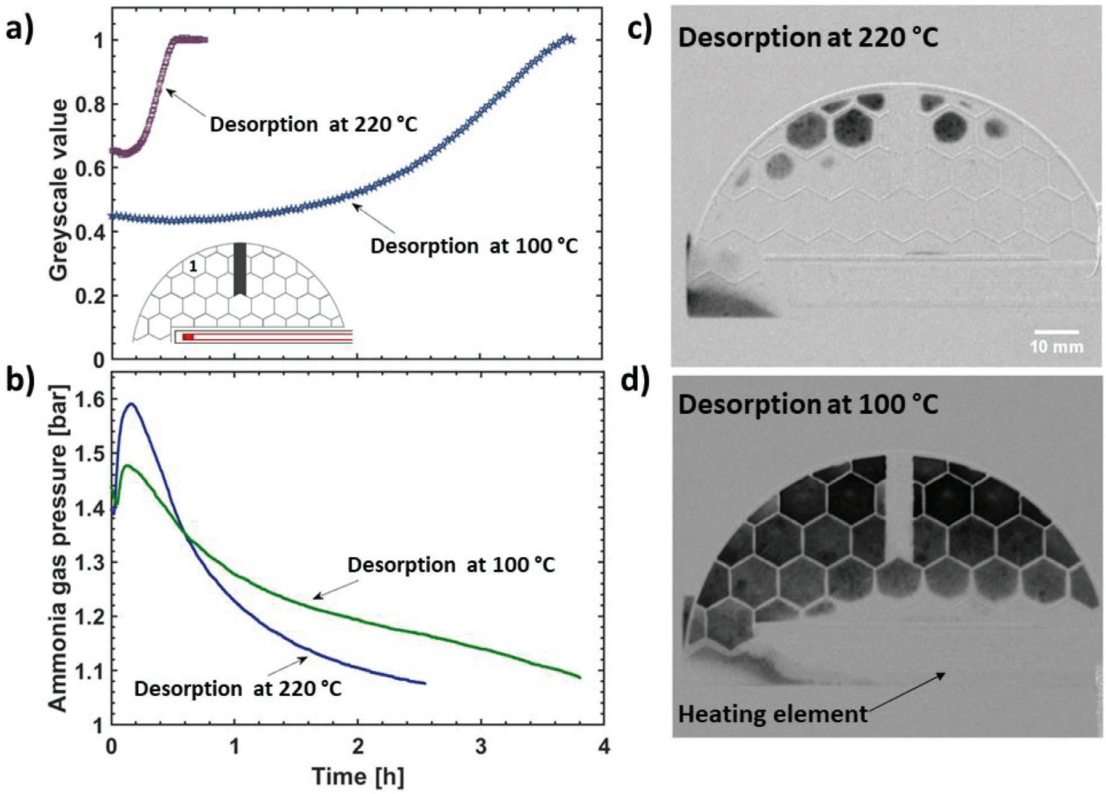

Fig. 7. The desorption processes of $SrCl_2(NH_3)_8$ at 220 °C and 100 °C: **(a)** changes of the transmission *I(λ)* and **(b)** corresponding pressure profile. Transmission images obtained after 20 min of NH_3 desorption processes performed at (**c**) 220 °C and (**d**) 100 °C.

$Sr(NH_3)_8Cl_2$ in the Fig. 9b shows that the powder occupies a slightly bigger volume in the cells compared to $SrCl_2$ (a), due to the $SrCl_2$ powder expansion during NH_3 absorption and shrinkage after NH_3 desorption. The 3D visualization of the partially desorbed state in Fig. 9c confirms the direction of the desorption reaction discussed above (Fig. 8) and that the $Sr(NH_3)_8Cl_2$ powder in the cells close to the heating element started releasing NH_3 first.

The 3D visualization of the $Sr(NH_3)_8Cl_2$ in Fig. 9b was further analyzed by cutting orthogonal slices and studying the reactor in different planes. This allowed for a detailed view "inside" the investigated sample. This is shown in Fig. 10, which displays the $Sr(NH_3)_8Cl_2$ powder in the honeycomb viewed through the XY and YZ-planes. The powder separated by the cell walls can be recognized and the irregular height of the powder both within each cell and over the honeycomb is confirmed. Additionally, a significant deformation of the honeycomb is observed by viewing the sample through two different planes.

In Fig. 10 the red dashed line represents the original position of the honeycomb back plate, being flat before the experiments, but is found bended after the NH_3 absorption. This is likely caused by the $SrCl_2$ expansion occurring during NH_3 absorption and formation of $Sr(NH_3)_8Cl_2$. The stainless steel cell walls kept the powder from expanding in the radial direction, while the open front of the honeycomb allowed the powder to expand in the axial direction as displayed in Fig. 6. This volume expansion caused stresses on the honeycomb back plate pushing it away from the honeycomb net. It should be noted that the back plate was welded to the honeycomb only along outer edges, but not to the entire net, making it vulnerable to potential stresses.

3.4. Feasibility of quantitative analysis of the acquired neutron imaging data

This work was focused only on the qualitative analysis of the obtained neutron imaging data. While it is generally possible to perform quantitative analysis from neutron imaging data, several uncertainties prevented us from quantifying in a reliable manner the NH_3 content in the investigated sample. In principle, the NH_3 content in the powder can be calculated from the neutron attenuation coefficient of NH_3. When neutrons pass through the sample, they are attenuated according the Beer-Lambert's law:

$$I(\lambda) = I_0 e^{-\mu(\lambda)x}$$

where I is an attenuated beam intensity, I_0 is an intensity behind a sample, μ is the neutron attenuation coefficient, λ is the neutron wavelength and x is the thickness of the sample. Here the dependence on neutron wavelength is neglected since the variation of the neutron attenuation coefficient of NH_3 and $SrCl_2$ for the herein used thermal spectrum does not affect the presented qualitative results. For a precise quantitative analysis, it would be proper to use monochromatic beam, which on the other hand would result in worse time resolution. Thus, for the presented experiment, using whole available spectrum was advantageous. The small sample thickness allows to neglect the beam hardening effect [33].

As seen from the 2D and 3D images, some amount of powder fell off the honeycomb causing irregularities in the powder thickness over the volume. The honeycomb was open on one side for facilitating the interaction between NH_3 and $SrCl_2$. This allowed for some of the $SrCl_2$ to be displaced outside the honeycomb while mounting the reactor on the sample stage. As a result, the initial thickness of the powder in the honeycomb changed and could not be determined accurately for further calculation of the NH_3 wt.%.

Finally, it should also be noted that the incoherent scattering from hydrogen contained in the NH_3 molecule results in additional errors. In particular, incoherent scattering causes the transmission behind the sample values to appear higher than the real values [34]. This can lead

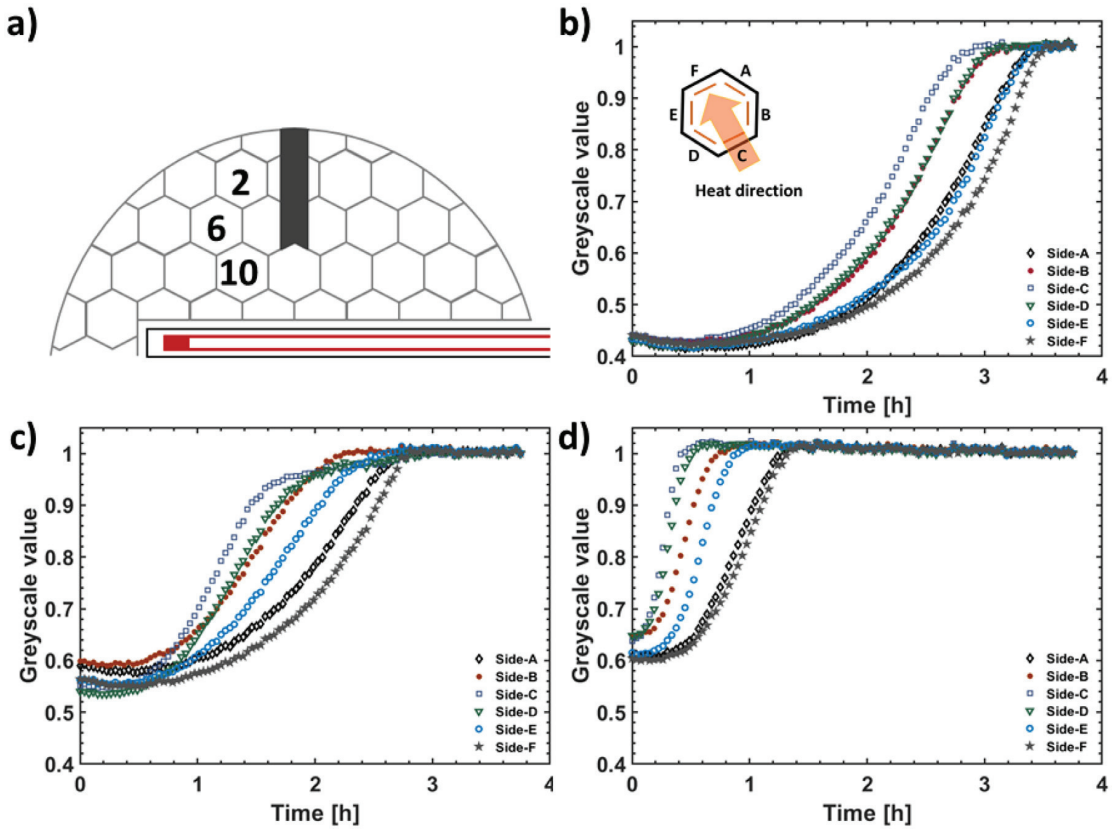

Fig. 8. The change of transmission *I(λ)* integrated along the selected volumes of the powder during desorption process at 100 °C (**a**) a schematic view of the honeycomb with the selected cells and the changes in transmission I(λ) along the lines drawn in cell-2 **(b)**, cell-6 **(c)** and cell-10 **(d)**. The heat direction is shown in the graph and is approximately the same in all three cases **(b)**.

to underestimate the thickness of the volume occupied by NH_3 and, in turn, the NH_3 concentration. A method for improving the quantification of neutron imaging measurements with scintillator-camera based detectors by correcting for biases introduced by scattered neutrons using reference measurement with a grid of neutron absorbers called black bodies (BB) was developed [35–37]. However, this method was not applied during the neutron imaging experiment discussed in this work.

4. Summary

Neutron imaging is an excellent method for evaluating NH_3 distribution in the $SrCl_2/Sr(NH_3)_8Cl_2$ system. It offers a unique possibility to study simultaneously NH_3 spatial distribution and the structural changes in the sample such as volume expansion of the powder during NH_3 absorption, which in turn might produce mechanical stresses on the THS reactor. In this work, we showed the inhomogeneous formation of $Sr(NH_3)_8Cl_2$ during NH_3 absorption processes which was possibly due to the location of the NH_3 gas inlet in the reactor and the presence of Ar in the cell at the beginning of the experiment. The latter remained at the bottom of the cell preventing NH_3 absorption in some parts of the powder. It was also shown that the stainless-steel honeycomb structure was not efficient for transferring the heat from the heating element to the edges of the honeycomb during the NH_3 desorption processes, as slower desorption kinetics are observed in the regions farthest away

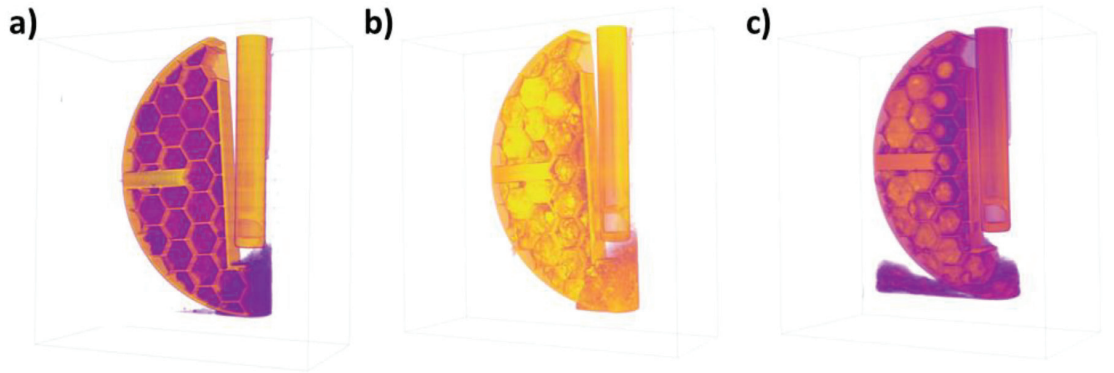

Fig. 9. 3D visualization of the honeycomb created with Tomviz software **(a)** fully desorbed $SrCl_2$ salt, **(b)** $Sr(NH_3)_8Cl_2$ and **(c)** the salt with partially desorbed NH_3. The colors of the different states are arbitrary and represented by the transmission through the absorbed NH_3 intensities.

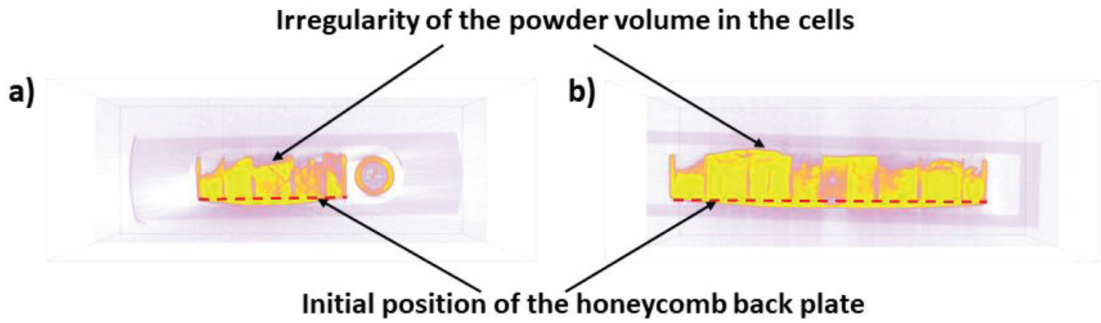

Fig. 10. Deformation of the honeycomb back plate after the NH_3 absorption process (**a)** *XY*-plane, slice $z = 394$ and (**b)** *YZ*-plane, slice $x = 310$. The red dashed lines represent the position of the back plate before the absorption process.

from the heater. Additional investigations by neutron tomography showed that the back plate supporting the honeycomb structure was deformed after the volume expansion during NH_3 absorption in the powder.

The results presented here demonstrate that neutron imaging techniques are ideal and powerful tools for investigating thermochemical heat storage prototype systems and provided critical information on $SrCl_2$ powder behavior upon NH_3 absorption and desorption reactions. Based on these results, some improvements – e.g. a honeycomb disc made of a material with better heat conductivity than stainless steel – will be implemented and tested. The outcome of those tests will be crucial for designing a safe and efficient THS reactor.

CRediT authorship contribution statement

Perizat Berdiyeva: Formal analysis, Investigation, Data curation, Visualization, Writing - original draft. **Anastasiia Karabanova:** Methodology, Formal analysis, Investigation, Resources, Writing - review & editing. **Malgorzata G. Makowska:** Formal analysis, Investigation, Writing - review & editing. **Rune E. Johnsen:** Conceptualization, Methodology, Investigation, Writing - review & editing. **Didier Blanchard:** Conceptualization, Methodology, Investigation, Resources, Project administration, Writing - review & editing, Funding acquisition. **Bjørn C. Hauback:** Writing - review & editing, Supervision. **Stefano Deledda:** Conceptualization, Investigation, Resources, Writing - review & editing, Supervision, Funding acquisition.

Declaration of Competing Interest

X The authors declare that they have no known competing financial interests or personal relationships that could have appeared to influence the work reported in this paper.

Acknowledgements

This work is funded by NordForsk Nordic Neutron Science Programme through the Neutrons for Heat Storage (NHS) project (No. 82206). The authors thank the Heinz Maier-Leibnitz Zentrum for neutron radiation beam time allocation and particularly Thomas Buecherl for experimental assistance. Furthermore, the Danish Research Council is greatly acknowledged for the financial support of the neutron measurements via DANSCATT (Grant number: 7055-00007B).

Supplementary materials

Supplementary material associated with this article can be found, in the online version, at doi:10.1016/j.est.2020.101388.

References

[1] D. Aydin, S.P. Casey, S. Riffat, The latest advancements on thermochemical heat storage systems, Renew. Sustain. Energy Rev. 41 (2015) 356–367, https://doi.org/10.1016/j.rser.2014.08.054.
[2] P.A.J. Donkers, L.C. Sogutoglu, H.P. Huinink, H.R. Fischer, O.C.G. Adan, A review of salt hydrates for seasonal heat storage in domestic applications, Appl. Energy 199 (2017) 45–68, https://doi.org/10.1016/j.apenergy.2017.04.080.
[3] H. Jarimi, D. Aydin, Z. Yanan, G. Ozankaya, X. Chen, S. Riffat, Review on the recent progress of thermochemical materials and processes for solar thermal energy storage and industrial waste heat recovery, Int. J. Low-Carbon Technol. 14 (2019) 44–69, https://doi.org/10.1093/ijlct/cty052.
[4] L.C. Sogutoglu, P.A.J. Donkers, H.R. Fischer, H.P. Huinink, O.C.G. Adan, In-depth investigation of thermochemical performance in a heat battery: cyclic analysis of K_2CO_3, $MgCl_2$ and Na_2S, Appl. Energy 215 (2018) 159–173, https://doi.org/10.1016/j.apenergy.2018.01.083.
[5] T. Yan, Z.H. Kuai, S.F. Wu, Experimental investigation on a $MnCl_2$–$SrCl_2$/NH_3 thermochemical resorption heat storage system, Renew. Energy 147 (2020) 874–883, https://doi.org/10.1016/j.renene.2019.09.033.
[6] T. Vegge, R.Z. Sørensen, A. Klerke, J.S. Hummelshøj, T. Johannessen, J.K. Nørskov, C.H. Christensen, 19 - Indirect hydrogen storage in metal ammines, in: G. Walker (Ed.), Solid-State Hydrog. Storage, Woodhead Publishing, 2008, pp. 533–564, , https://doi.org/10.1533/9781845694944.4.533.
[7] C.H. Christensen, R.Z. Sørensen, T. Johannessen, U.J. Quaade, K. Honkala, T.D. Elmøe, R. Køhler, J.K. Nørskov, Metal ammine complexes for hydrogen storage, J. Mater. Chem. 15 (2005) 4106–4108, https://doi.org/10.1039/B511589B.
[8] A. Klerke, C.H. Christensen, J.K. Nørskov, T. Vegge, Ammonia for hydrogen storage: challenges and opportunities, J. Mater. Chem. 18 (2008) 2304–2310, https://doi.org/10.1039/B720020J.
[9] S. Lysgaard, A.L. Ammitzbøll, R.E. Johnsen, P. Norby, U.J. Quaade, T. Vegge, Resolving the stability and structure of strontium chloride amines from equilibrium pressures, XRD and DFT, Int. J. Hydrog. Energy 37 (2012) 18927–18936, https://doi.org/10.1016/j.ijhydene.2012.09.129.
[10] R.E. Johnsen, P.B. Jensen, P. Norby, T. Vegge, Temperature- and pressure-induced changes in the crystal structure of $Sr(NH_3)8Cl_2$, J. Phys. Chem. C. 118 (2014) 24349–24356, https://doi.org/10.1021/jp508076c.
[11] A. Bialy, P.B. Jensen, D. Blanchard, T. Vegge, U.J. Quaade, Solid solution barium–strontium chlorides with tunable ammonia desorption properties and superior storage capacity, J. Solid State Chem. 221 (2015) 32–36, https://doi.org/10.1016/j.jssc.2014.09.014.
[12] M. Strobl, I. Manke, N. Kardjilov, A. Hilger, M. Dawson, J. Banhart, Advances in neutron radiography and tomography, J. Phys. Appl. Phys. 42 (2009) 243001, , https://doi.org/10.1088/0022-3727/42/24/243001.
[13] A. Baruj, M. Ardito, J. Marín, F. Sánchez, E.M. Borzone, G. Meyer, Design and characterization of a hydride-based hydrogen storage container for neutron imaging studies, Phys. Procedia 69 (2015) 491–495, https://doi.org/10.1016/j.phpro.2015.07.069.
[14] Ł. Gondek, N.B. Selvaraj, J. Czub, H. Figiel, D. Chapelle, N. Kardjilov, A. Hilger, I. Manke, Imaging of an operating $LaNi_4$.8Al0.2–based hydrogen storage container, Int. J. Hydrog. Energy. 36 (2011) 9751–9757, https://doi.org/10.1016/j.ijhydene.2011.05.089.
[15] F. Heubner, A. Hilger, N. Kardjilov, I. Manke, B. Kieback, Ł. Gondek, J. Banhart, L. Röntzsch, In-operando stress measurement and neutron imaging of metal hydride composites for solid-state hydrogen storage, J. Power Sources 397 (2018) 262–270, https://doi.org/10.1016/j.jpowsour.2018.06.093.
[16] M.G. Makowska, L.T. Kuhn, H.L. Frandsen, E.M. Lauridsen, S. De Angelis, L.N. Cleemann, M. Morgano, P. Trtik, M. Strobl, Coupling between creep and redox behavior in nickel - yttria stabilized zirconia observed in-situ by monochromatic neutron imaging, J. Power Sources 340 (2017) 167–175, https://doi.org/10.1016/j.jpowsour.2016.11.059.
[17] P. Boillat, E.H. Lehmann, P. Trtik, M. Cochet, Neutron imaging of fuel cells – recent trends and future prospects, Curr. Opin. Electrochem. 5 (2017) 3–10, https://doi.org/10.1016/j.coelec.2017.07.012.
[18] J. Zhang, D. Kramer, R. Shimoi, Y. Ono, E. Lehmann, A. Wokaun, K. Shinohara, G.G. Scherer, In situ diagnostic of two-phase flow phenomena in polymer

electrolyte fuel cells by neutron imaging: Part B. material variations, Electrochim. Acta 51 (2006) 2715–2727, https://doi.org/10.1016/j.electacta.2005.08.010.
[19] M. Siegwart, R.P. Harti, V. Manzi-Orezzoli, J. Valsecchi, M. Strobl, C. Grünzweig, T.J. Schmidt, P. Boillat, Selective visualization of water in fuel cell gas diffusion layers with neutron dark-field imaging, J. Electrochem. Soc. 166 (2019) F149–F157, https://doi.org/10.1149/2.1011902jes.
[20] D.S. Hussey, D.L. Jacobson, M. Arif, K.J. Coakley, D.F. Vecchia, In situ fuel cell water metrology at the NIST neutron imaging facility, J. Fuel Cell Sci. Technol. (2010) 7, https://doi.org/10.1115/1.3007898.
[21] I. Manke, H. Markötter, C. Tötzke, N. Kardjilov, R. Grothausmann, M. Dawson, C. Hartnig, S. Haas, D. Thomas, A. Hoell, C. Genzel, J. Banhart, Investigation of energy-relevant materials with synchrotron x-rays and neutrons, Adv. Eng. Mater. 13 (2011) 712–729, https://doi.org/10.1002/adem.201000284.
[22] A. Senyshyn, M.J. Mühlbauer, K. Nikolowski, T. Pirling, H. Ehrenberg, "In-operando" neutron scattering studies on Li-ion batteries, J. Power Sources 203 (2012) 126–129, https://doi.org/10.1016/j.jpowsour.2011.12.007.
[23] G.V. Riley, D.S. Hussey, D. Jacobson, In situ neutron imaging of alkaline and lithium batteries, ECS Trans. 25 (2010) 75–83, https://doi.org/10.1149/1.3414005.
[24] Z. Nie, P. McCormack, H.Z. Bilheux, J.C. Bilheux, J.P. Robinson, J. Nanda, G.M. Koenig, Probing lithiation and delithiation of thick sintered lithium-ion battery electrodes with neutron imaging, J. Power Sources 419 (2019) 127–136, https://doi.org/10.1016/j.jpowsour.2019.02.075.
[25] K. Kino, M. Yonemura, Y. Kiyanagi, Y. Ishikawa, Joseph.Don. Parker, T. Tanimori, T. Kamiyama, First imaging experiment of a lithium ion battery by a pulsed neutron beam at J-PARC/MLF/BL09, Phys. Procedia. 69 (2015) 612–618, https://doi.org/10.1016/j.phpro.2015.07.087.
[26] N. Kardjilov, I. Manke, A. Hilger, M. Strobl, J. Banhart, Neutron imaging in materials science, Mater. Today 14 (2011) 248–256, https://doi.org/10.1016/S1369-7021(11)70139-0.
[27] N. Kardjilov, I. Manke, R. Woracek, A. Hilger, J. Banhart, Advances in neutron imaging, Mater. Today 21 (2018) 652–672, https://doi.org/10.1016/j.mattod.2018.03.001.
[28] S.N. Gunasekara, M. Laios, A. Karabanova, V. Martin, D. Blanchard, Numerical Design of a Reactor-Heat Exchanger Combined Unit for Ammonia-SrCl2 Thermochemical Storage System, (2019), pp. 1–12.
[29] T. Bücherl, S. Söllradl, NECTAR: radiography and tomography station using fission neutrons, J. Large-Scale Res. Facil. 1 (2015) 19, https://doi.org/10.17815/jlsrf-1-45.
[30] ImageJ2: ImageJ for the next generation of scientific image data | BMC Bioinformatics | Full Text, (n.d.). https://bmcbioinformatics.biomedcentral.com/articles/10.1186/s12859-017-1934-z(accessed October 23, 2019).
[31] A.P. Kaestner, MuhRec—a new tomography reconstructor, Nucl. Instrum. Methods Phys. Res. Sect. 651 (2011) 156–160, https://doi.org/10.1016/j.nima.2011.01.129.
[32] M.D. Hanwell, C.J. Harris, A. Genova, J. Schwartz, Y. Jiang, R. Hovden, Tomviz: open source platform connecting image processing pipelines to GPU accelerated 3D visualization, Microsc. Microanal. 25 (2019) 408–409, https://doi.org/10.1017/S1431927619002770.
[33] E.H. Lehmann, P. Vontobel, N. Kardjilov, Hydrogen distribution measurements by neutrons, Appl. Radiat. Isot. 61 (2004) 503–509, https://doi.org/10.1016/j.apradiso.2004.03.075.
[34] R. Hassanein, F. de Beer, N. Kardjilov, E. Lehmann, Scattering correction algorithm for neutron radiography and tomography tested at facilities with different beam characteristics, Phys. B Condens. Matter. 385–386 (2006) 1194–1196, https://doi.org/10.1016/j.physb.2006.05.406.
[35] P. Boillat, C. Carminati, F. Schmid, C. Grünzweig, J. Hovind, A. Kaestner, D. Mannes, M. Morgano, M. Siegwart, P. Trtik, P. Vontobel, E.H. Lehmann, Chasing quantitative biases in neutron imaging with scintillator-camera detectors: a practical method with black body grids, Opt. Express. 26 (2018) 15769–15784, https://doi.org/10.1364/OE.26.015769.
[36] P. Trtik, E.H. Lehmann, Progress in high-resolution neutron imaging at the Paul Scherrer Institut - the neutron microscope project, J. Phys. Conf. Ser. 746 (2016) 012004, , https://doi.org/10.1088/1742-6596/746/1/012004.
[37] C. Carminati, P. Boillat, F. Schmid, P. Vontobel, J. Hovind, M. Morgano, M. Raventos, M. Siegwart, D. Mannes, C. Gruenzweig, P. Trtik, E. Lehmann, M. Strobl, A. Kaestner, Implementation and assessment of the black body bias correction in quantitative neutron imaging, PLOS ONE 14 (2019) e0210300, , https://doi.org/10.1371/journal.pone.0210300.

In-situ neutron imaging study of NH_3 absorption and desorption in $SrCl_2$ within a heat storage prototype reactor

Perizat Berdiyeva[a], Anastasiia Karabanova[b], Malgorzata G. Makowska[c], Rune E. Johnsen[b], Didier Blanchard[b], Bjørn C. Hauback[a] and Stefano Deledda[a]*

a) Department for Neutron Materials Characterization, Institute for Energy Technology, P.O. Box 40, NO-2027, Kjeller, Norway
b) Department of Energy Conversion and Storage, Technical University of Denmark, Fysikvej, DK-2800, Lyngby, Denmark
c) Photon Science Division, Paul-Scherrer Institute, Forschungsstrasse 111, 5232-Villigen, Switzerland

SUPPLEMENTARY INFORMATION

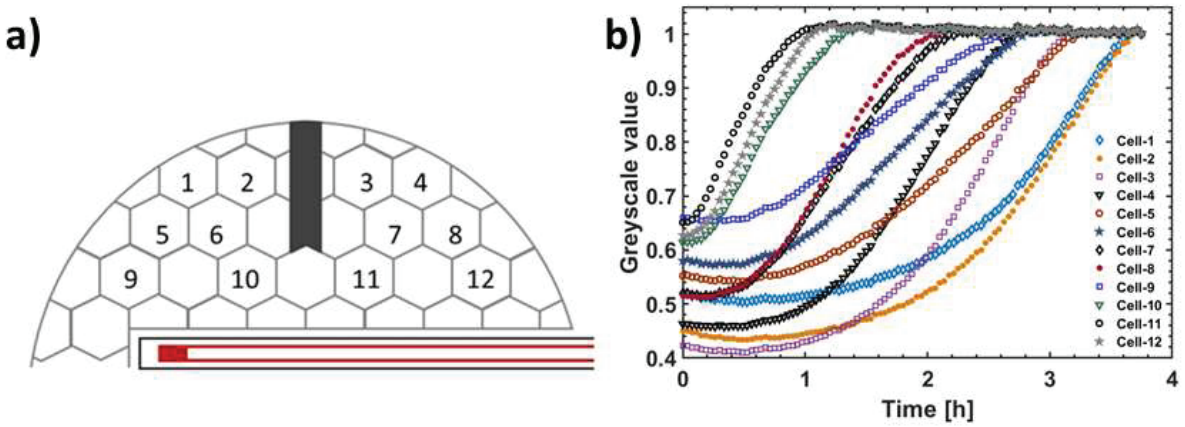

Figure A.1. The transmission I(λ) change over time during NH_3 desorption at 100 °C. The mean greyscale values are taken from the area of each selected cell.

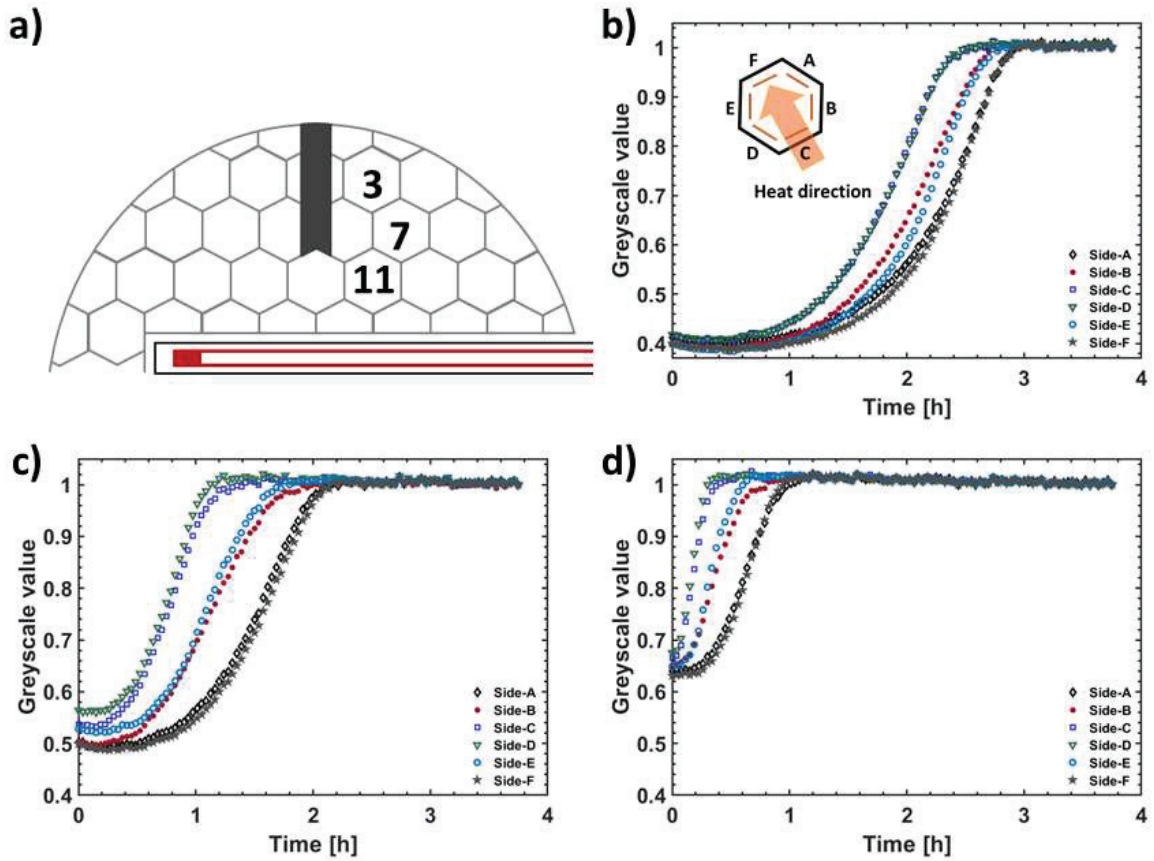

Figure A.2. The transmission I(λ) change integrated along the selected volumes of the powder during desorption process at 100 °C ***a)*** *a schematic view of the honeycomb with selected three cells and the transmission I(λ) change along the lines drawn in cell-3* ***(b)****, cell-7* ***(c)*** *and* ***d)*** *cell-11 The heat direction is shown in the graph and is the same in all three cases* ***(b)****.*

Publication IV

Synthesis, structure and NH_3 sorption properties of mixed $Mg_{1-x}Mn_x(NH_3)_6Cl_2$ ammines

P. Berdiyeva, A. Karabanova, J. B. Grinderslev, R. E. Johnsen, D. Blanchard, B. C. Hauback and S. Deledda

Energies, **2020**, 13, 2746.

Graphical abstract

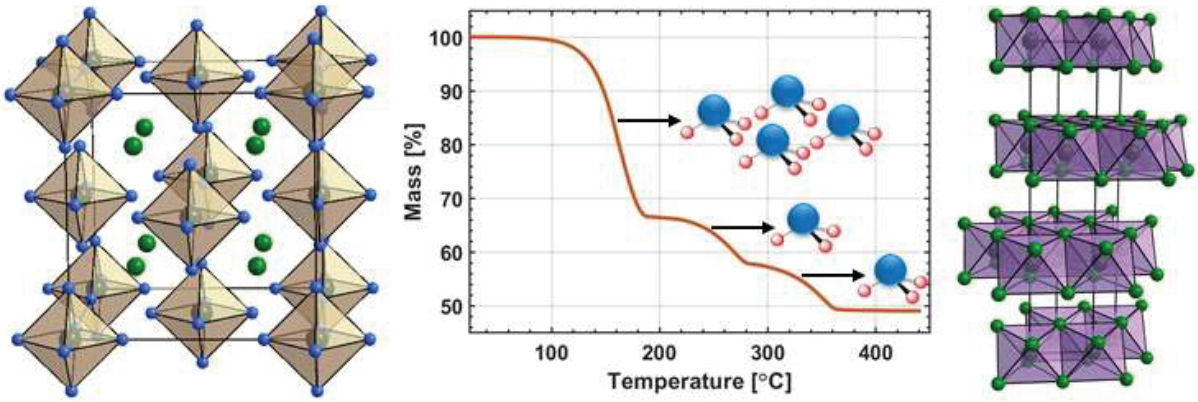

energies

MDPI

Article

Synthesis, Structure and NH_3 Sorption Properties of Mixed $Mg_{1-x}Mn_x(NH_3)_6Cl_2$ Ammines

Perizat Berdiyeva [1], Anastasiia Karabanova [2], Jakob B. Grinderslev [3], Rune E. Johnsen [2], Didier Blanchard [2], Bjørn C. Hauback [1] and Stefano Deledda [1,*]

[1] Department for Neutron Materials Characterization, Institute for Energy Technology, P.O. Box 40, NO-2027 Kjeller, Norway; perizat.berdiyeva@ife.no (P.B.); Bjorn.Hauback@ife.no (B.C.H.)
[2] Department of Energy Conversion and Storage, Technical University of Denmark, Fysikvej, DK-2800 Lyngby, Denmark; anaka@dtu.dk (A.K.); runeejohnsen@gmail.com (R.E.J.); dibl@dtu.dk (D.B.)
[3] Center for Materials Crystallography, Interdisciplinary Nanoscience Center (iNANO) and Department of Chemistry, Aarhus University, Langelandsgade 140, 8000 Aarhus C, Denmark; jakobg@inano.au.dk
* Correspondence: Stefano.deledda@ife.no; Tel.: +47-407-26-921

Received: 29 April 2020; Accepted: 28 May 2020; Published: 30 May 2020

Abstract: This paper describes the synthesis, crystal structure, and NH_3 sorption properties of $Mg_{1-x}Mn_x(NH_3)_6Cl_2$ (x = 0–1) mixed metal halide ammines, with reversible NH_3 storage capacity in the temperature range 20–350 °C. The stoichiometry (x) dependent NH_3 desorption temperatures were monitored using in situ synchrotron radiation powder X-ray diffraction, thermogravimetric analysis, and differential scanning calorimetry. The thermal analyses reveal that the NH_3 release temperatures decrease in the mixed metal halide ammines in comparison to pure $Mg(NH_3)_6Cl_2$, approaching the values of $Mn(NH_3)_6Cl_2$. Desorption occurs in three steps of four, one and one NH_3 moles, with the corresponding activation energies of 54.8 kJ·mol^{-1}, 73.2 kJ·mol^{-1} and 91.0 kJ·mol^{-1} in $Mg_{0.5}Mn_{0.5}(NH_3)_6Cl_2$, which is significantly lower than the NH_3 release activation energies of $Mg(NH_3)_6Cl_2$ (E_a = 60.8 kJ·mol^{-1}, 74.8 kJ·mol^{-1} and 91.8 kJ·mol^{-1}). This work shows that $Mg_{1-x}Mn_x(NH_3)_yCl_2$ (x = 0 to 1, y = 0 to 6) is stable within the investigated temperature range (20–350 °C) and also upon NH_3 cycling.

Keywords: metal chlorides; solid solution; mixed hexammines; ammonia storage; in situ powder X-ray diffraction

1. Introduction

Energy storage materials and methods have gained high interest to ensure the transition to carbon-free future. Hydrogen, as a high-density energy carrier alternative to fossil fuels, is one of the promising solutions for energy storage systems via solid storage of hydrogen [1–4]. Several studies have highlighted the potential of ammonia for hydrogen-based energy systems [5–8].

Metal halide ammines have been studied as indirect hydrogen and ammonia storage materials [9–11]. Particularly $Mg(NH_3)_6Cl_2$ has received significant attention due to its high gravimetric NH_3 and H_2 capacity of 51.8 wt% and 9.2 wt%, respectively [12–17]. $Mg(NH_3)_6Cl_2$ crystallizes in the cubic space group *Fm*-3*m* with a K_2PtCl_6-structure type and a = 10.1899(4) Å [18]. NH_3 is thermally released in three steps at the temperatures of 142 °C (4 moles of NH_3), 230 °C (1 mole of NH_3) and 375 °C (1 mole of NH_3), respectively against an ammonia pressure of 1 bar [15]. The phase-formation and thermodynamic properties of $Mg(NH_3)_6Cl_2$, $Mg(NH_3)_2Cl_2$ and $Mg(NH_3)Cl_2$ have been thoroughly studied, and the high temperatures necessary to release the two last moles of NH_3 hampers the application of $Mg(NH_3)_6Cl_2$ as an effective energy storage system [19–22]. However, the desorption temperatures of NH_3 may be tailored toward lower NH_3 desorption temperatures via the formation of solid solutions, e.g., mixed cation metal halide ammines. $Mn(NH_3)_6Cl_2$ also exhibits a high gravimetric capacity of ammonia (44.8 wt%), and is isostructural to $Mg(NH_3)_6Cl_2$ with a slightly larger

unit cell parameter: a = 10.249(3) Å [23]. Similar to $Mg(NH_3)_6Cl_2$, NH_3 is released from $Mn(NH_3)_6Cl_2$ in three steps with desorption temperatures of 80 °C, 180 °C, and 354 °C, respectively, and thus lower than the desorption temperatures of $Mg(NH_3)_6Cl_2$ [13,15]. However, only the sorption cyclability of the four first moles of NH_3 in $Mn(NH_3)_6Cl_2$ has been considered for ammonia storage applications, which is found to be reversible for at least 10 cycles [10].

The ammonia release temperatures are associated with the binding energy of NH_3 with its surrounding ions, which depends on the elements and crystal structures of the metal halides as elucidated in a recent study [24]. Formation of solid solutions has been suggested as an approach to tailor the NH_3 desorption temperatures and kinetics [25–27]. The NH_3 binding energies were investigated in $SrCl_2$-$CaCl_2$ solid solutions, and they were found to be intermediate those of the two precursors [28]. This led to studies on solid solutions of $Sr_{1-x}Ba_x(NH_3)_8Cl_2$ and $Sr_{1-x}Ca_x(NH_3)_8Cl_2$, and their respective NH_3 release properties. $Sr_{1-x}Ba_x(NH_3)_8Cl_2$ solid solutions showed that varying the relative ratios of metal allowed tuning of the desorption temperature of ammonia. The gradual effect on the ammonia release temperature was observed with the optimal mixing condition of 37.5 % of $BaCl_2$ in $Sr_{1-x}Ba_x(NH_3)_8Cl_2$ showing the full release of ammonia at temperature T < 100 °C of the final mixed metal halide ammine [25]. Similarly, it was demonstrated for $Sr_{1-x}Ca_xCl_2$ solid solutions and the corresponding $Sr_{1-x}Ca_x(NH_3)_8Cl_2$ ammines that the NH_3 absorption and desorption properties could be enhanced by tuning the mixing ratio [26,27]. Additionally, the ammonia storage properties and crystal structures of the $CaCl_2$-$CaBr_2$, $SrCl_2$-$SrBr_2$ and $SrCl_2$-SrI_2 solid solutions have also been investigated, and intermediate ammonia storage properties of the mixed anion metal halides were observed [28–30]. These studies show the possibility of forming mixed metal halides with tunable ammonia sorption properties. Solid solutions of borohydride-based ammines have also been investigated as potential solid-state hydrogen storage materials. The solid solutions of $Mg_{1-x}Mn_x(BH_4)_2{\cdot}6NH_3$ and structural similarities of $Mg(BH_4)_2$ and $Mn(BH_4)_2$ and their corresponding ammines were studied [31,32]. Similar to the present study it revealed temperature changes for ammonia release when compared to those of the pristine samples.

Inspired by the structural similarities between $Mg(NH_3)_6Cl_2$ and $Mn(NH_3)_6Cl_2$, this work addresses an investigation of solid solutions of $Mg_{1-x}Mn_x(NH_3)_6Cl_2$. Here we show the synthesis of these novel series of mixed metal halide ammines with tunable properties for the NH_3 desorption. We present the $Mg_{1-x}Mn_x(NH_3)_6Cl_2$ (x = 0.025, 0.05, 0.1, 0.3 and 0.5) solid solutions obtained by mechanical mixing of $MgCl_2$ and $MnCl_2$, followed by annealing and subsequent exposure to anhydrous NH_3 gas. The mixed metal halide ammines were systematically investigated with in situ powder X-ray diffraction, thermogravimetric analysis, differential scanning calorimetry and volumetric Sieverts techniques. The thermally induced ammonia release for the mixed metal halide ammines is discussed: three NH_3 desorption events are observed and the crystal structures of the intermediate ammine phases are identified and structurally characterized. The kinetics, absorption, and desorption properties of NH_3 are studied. The results presented in this work show that by changing the relative Mg/Mn ratio the NH_3 sorption properties can be tuned and optimized depending on the application.

2. Materials and Methods

2.1. Sample Preparation

Anhydrous $MgCl_2$ and $MnCl_2$ powders with a purity of 99.999% were purchased from Alfa Aesar and Sigma-Aldrich, respectively. $Mg_{1-x}Mn_xCl_2$ solid solutions (x = 0.025, 0.05, 0.1, 0.3 and 0.5) were obtained using a SPEX SamplePrep 8000D Dual Mixer high-energy ball mill. The powders were placed in a 25 mL hardened steel vial together with hardened steel balls (10 mm diameter) in a ball-to-powder mass ratio of 16:1 and sealed in an Ar-filled glove box (< 1 ppm of O_2 and H_2O). The ball milling program was for one hour.

The as-milled powders were annealed to increase the crystallinity. Batches of ~0.5 g of the as-milled powders were sealed in a stainless-steel cylinder inside a glove box, and subsequently heated to 350 °C with a heating rate of 1 °C·sec^{-1} and kept isothermal at 350 °C for 24 hours. These samples

are denoted "as-synthesized" samples. Subsequently, the as-synthesized samples were placed in a high temperature stainless-steel cylinder and connected to an in-house built Sieverts apparatus. The samples were then exposed to an NH_3 gas pressure of 2.5 bar at room temperature (RT) for at least 3 hours. $MnCl_2$ was ammoniated for 3 hours at T = −20 °C and 1 bar NH_3. It was then stored in a glovebox freezer at −34 °C prior to the experiments, due to instability of the $Mn(NH_3)_6Cl_2$ at ambient conditions. These samples are denoted "ammoniated" samples.

2.2. Thermal Analysis

Combined thermogravimetric analysis (TGA) and differential scanning calorimetry (DSC) of the monometallic and mixed metal halide ammines were measured using a Netzsch STA 449 F3 Jupiter apparatus. The powders (~40 mg) were placed in an alumina crucible with a pierced lid under protective Ar atmosphere in a glove box. The alumina crucibles were shortly exposed to air (ca. 1 min) during mounting in the TGA-DSC apparatus. The powders were heated from RT to 455 °C with a heating rate of 5 °C·min^{-1} in an Ar flow of 50 mL·min^{-1}. Additionally, the batches of $Mg(NH_3)_6Cl_2$, $Mg_{0.5}Mn_{0.5}(NH_3)_6Cl_2$ and $Mn(NH_3)_6Cl_2$ powder (~10 mg) were measured at six different heating rates of 1, 2, 5, 10, 20 and 40 °C·min^{-1} for Kissinger analyses [33].

2.3. Synchrotron Radiation Powder X-Ray Diffraction

High resolution in situ temperature varied synchrotron radiation powder X-ray diffraction (SR-PXD) experiments were performed at the Swiss Light Source (SLS), Switzerland and at the Diamond Light Source, Oxford, UK. At SLS, data were obtained at the Material Science powder diffraction beamline X04SA [34] using a monochromatic beam in Debye–Scherrer geometry with a Mythen microstrip detector with a wavelength of λ = 0.709396 Å. At Diamond, data were obtained at the I11 beamline [35] using a wide angle position sensitive detector and a wavelength of λ = 0.82646 Å. In both cases, the samples were loaded into 0.5 mm borosilicate glass capillaries in an Ar-filled glove box (< 1 ppm of O_2 and H_2O), sealed with grease and rotated during data acquisition. The samples were heated at 5 °C·min^{-1} from RT to 500 °C using a heat blower. The temperature was calibrated using a NaCl standard prior to diffraction runs [36]. The powder diffraction data were normalized and reduced, then modeled and refined according to the Rietveld method as implemented in the TOPAS software [37].

The structural models of $Mg(NH_3)_6Cl_2$, $Mg(NH_3)_2Cl_2$ and $Ni(NH_3)Cl_2$ were used as starting points for Rietveld refinements of the hexammine, diammine, and monoammine phases of the mixed metal halide ammines, respectively. The diffraction peaks were modeled by a Thompson-Cox-Hastings pseudo-Voigt function. The scale factor, zero-shift, unit cell parameters, atomic positions and background were refined. The N-H and H-H distances were restrained using soft restraints function during the Rietveld refinements.

2.4. Sorption Kinetics and Cycling

The two pristine materials $MgCl_2$ and $MnCl_2$ and the mixed metal halides $Mg_{0.9}Mn_{0.1}Cl_2$ and $Mg_{0.5}Mn_{0.5}Cl_2$ (m ~ 0.1 g) were studied with regards to their NH_3 absorption and desorption kinetics. The absorption process was conducted under 2.5 bar of NH_3 at RT, while the desorption reaction was achieved by heating the samples up to 350 °C with a heating rate of 2 °C·min^{-1} under 1 bar of NH_3. A calibrated volume consisting of a reference volume (V = 482.9 mL) and a sample chamber (V = 23.25 mL) was used during the experiments and the moles of absorbed and desorbed NH_3 were calculated according ideal gas law using the formula below:

$$\Delta n = \frac{\Delta PV}{RT}, \quad (1)$$

where Δn is the number of NH_3 moles absorbed or desorbed, ΔP is the pressure change in the system occurring due to absorption or desorption of NH_3, V is the volume, R is the gas constant and T is the temperature. In all cases, the number of absorbed or desorbed moles was normalized by the molar weight of the corresponding compound. Each NH_3 desorption was followed by evacuation of the

released NH_3 from the cylinder to avoid reabsorption of the NH_3 gas during cooling to RT. The NH_3 desorption/absorption was cycled four times for each sample.

3. Results and Discussion

3.1. Structural Characterization of the As-Synthesized and Ammoniated Samples at RT

SR-PXD data were collected for the pristine samples, $MgCl_2$ and $MnCl_2$, and for the as-synthesized $Mg_{1-x}Mn_xCl_2$, (x = 0.025, 0.05, 0.1, 0.3 and 0.5) samples. The unit cell parameters are presented in Table S1 in the Supporting Information. The diffraction patterns in Figure 1 confirm the formation of a $MgCl_2$-$MnCl_2$ solid solutions, as only a single set of Bragg diffraction peaks belonging to $Mg_{1-x}Mn_xCl_2$ are observed, which is positioned in between that of $MgCl_2$ and $MnCl_2$. $MgCl_2$ and $MnCl_2$ are isostructural and crystallize in the trigonal $CdCl_2$-type structure with space group symmetry *R*-3*m* [38,39].

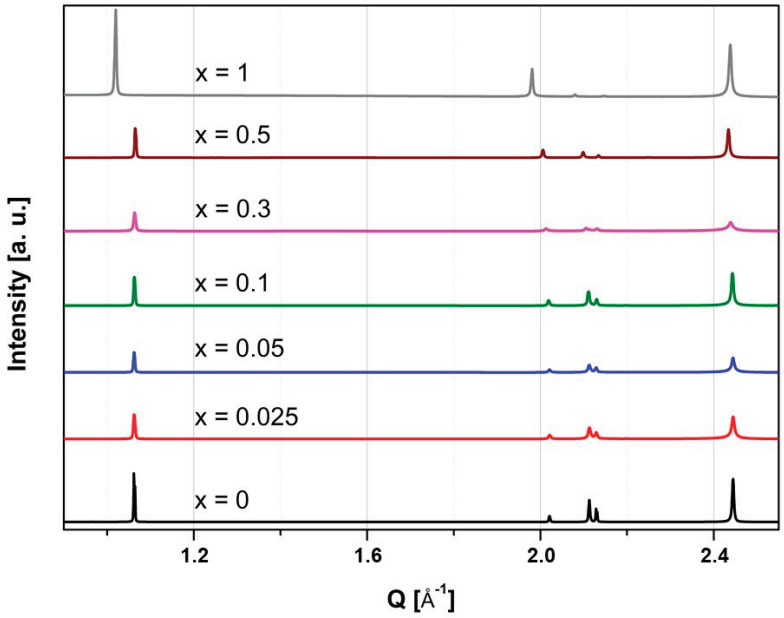

Figure 1. SR-PXD patterns of $Mg_{1-x}Mn_xCl_2$ (x = 0, 0.025, 0.05, 0.1, 0.3, 0.5 and 1) obtained at RT. All peaks belong to the same $CdCl_2$-type phase.

The $MgCl_2$-$MnCl_2$ solid solution follows Vegard's law approximately, as the volume is a function of the relative content of cations and in between that of the two pristine compounds, see Figure 2a. The larger ionic radius of Mn^{2+} (0.83 Å) as compared to Mg^{2+} (0.72 Å) results in an increase of the unit cell volume [40]. The deviation from Vegard's law might be due to a localized strain field caused by difference in Mg and Mn sizes, as well as to the different outer electronic structures of the mixing components (Mg and Mn in our case) [41]. The solid solution is maintained after ammoniation and the deviation from Vegard's law remains. It should be noted that a negative deviation from Vegard's law should be also expected if contamination from iron contained in the milling media results in the form $Mg_{1-x-y}Mn_xFe_yCl_2$. Indeed, the ionic radius for Fe^{2+} (0.63 Å) is smaller than the radii of both Mg^{2+} and Mn^{2+} [40]. However, even if slight contaminations from the milling media and metallic Fe cannot be ruled out, they are expected to be very limited due to the relatively short milling time (1 hour) used in this work. Additionally, metallic Fe must be oxidized to Fe^{2+} in order to substitute Mg^{2+}/Mn^{2+} and form $Mg_{1-x-y}Mn_xFe_yCl_2$. Therefore, it is most likely that the deviation from Vegard's law observed here might be due to the different outer electronic structures of Mg and Mn. Rietveld refinement and structural characterization of the ammoniated samples confirm the cubic $Mg(NH_3)_6Cl_2$ structure for all mixed cation hexammines (Supporting Information, Figures S1–S5). Figure 2b illustrate Vegard's

law (blue dotted line) for $Mg_{1-x}Mn_x(NH_3)_6Cl_2$. Surprisingly, the unit cell volume for samples with $x < 0.05$ are lower than that of $Mg(NH_3)_6Cl_2$.

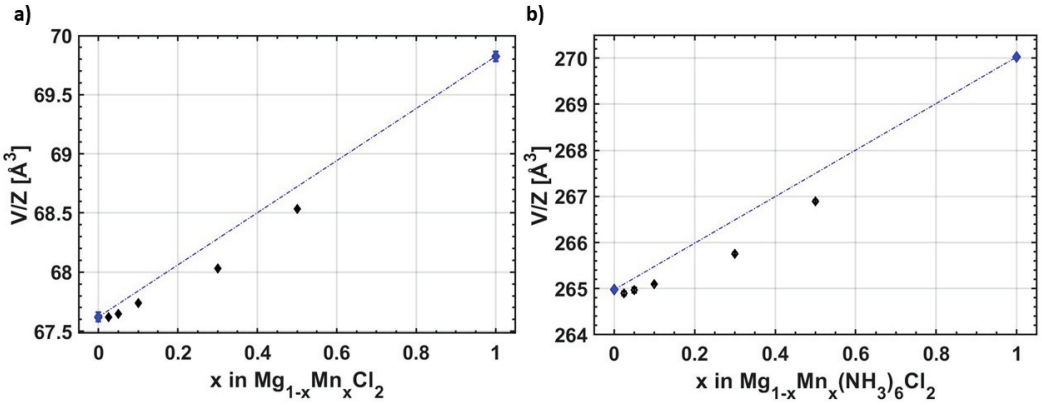

Figure 2. Unit cell volumes (V) of (**a**) $Mg_{1-x}Mn_xCl_2$ and (**b**) $Mg_{1-x}Mn_x(NH_3)_6Cl_2$ at RT divided by the number of formula units (Z), plotted as a function of the Mn amount in the formula unit (x = 0, 0.025, 0.05, 0.1, 0.3, 0.5 and 1). The blue dotted line represents Vegard's law. The standard deviations are within the data points.

The atomic positions of the monometallic and mixed hexammines obtained from Rietveld refinement are presented in Table 1. During the Rietveld refinements Mg and Cl atoms are fixed in the 4*a* and 8*c* positions, respectively, while the x-coordinate of N atom (24*e* position) is refined. N-H and H-H distances are restrained at ~ 1.107 Å and ~ 1.345 Å, respectively. Mg-N and Mn-N bond distances for the monometallic hexammines are 2.1564(7) Å and 2.2100(14) Å and thus similar to the previously reported values (2.197(5) [18] and 2.270(15) [23], respectively). $Mg_{1-x}Mn_x$-N bond distances are intermediate between the Mg-N and Mn-N bond distances. The unit cell parameters of the monometallic $Mg(NH_3)_6Cl_2$ and $Mn(NH_3)_6Cl_2$ obtained in this study are a = 10.19579(9) Å and a = 10.26017(2) Å which correspond to the values reported previously [18,23]. The unit cell parameters for $Mg_{1-x}Mn_x(NH_3)_6Cl_2$ are also intermediate between the unit cell parameters of the monometallic hexammines.

Table 1. Atomic positions of the monometallic and mixed hexammines: $Mg_{1-x}Mn_x$ (x = 0 to 1) in (0, 0, 0), Cl in (1/4, 1/4, 1/4) and N in (x, 0, 0)*.

Compound	N (x-coordinate)
$Mg(NH_3)_6Cl_2$	0.21150(7), 0, 0
$Mg_{0.975}Mn_{0.025}(NH_3)_6Cl_2$	0.21268(15), 0, 0
$Mg_{0.95}Mn_{0.05}(NH_3)_6Cl_2$	0.2132(2), 0, 0
$Mg_{0.9}Mn_{0.1}(NH_3)_6Cl_2$	0.21363(8), 0, 0
$Mg_{0.7}Mn_{0.3}(NH_3)_6Cl_2$	0.21269(9), 0, 0
$Mg_{0.5}Mn_{0.5}(NH_3)_6Cl_2$	0.21267(10), 0, 0
$Mn(NH_3)_6Cl_2$	0.21540(14), 0, 0

* The data are obtained at RT.

3.2. Thermal Analysis

Figure 3 shows the TGA-DSC measurements performed on $Mg(NH_3)_6Cl_2$, $Mn(NH_3)_6Cl_2$ and $Mg_{0.5}Mn_{0.5}(NH_3)_6Cl_2$. The DSC measurements for the other mixed ammines are shown in the Supporting Information (Figure S6). All the hexammine compounds are relatively stable at RT, except for $Mn(NH_3)_6Cl_2$, which slowly releases NH_3 in the glove box at RT. Thus, $Mn(NH_3)_6Cl_2$ was kept at T = −34 °C in a glovebox freezer prior to the TGA-DSC measurements.

TGA-DSC data shows the desorption process of the monometallic and mixed chloride ammines which consists of three events. With a heating rate of 5 °C·min^{-1}, the onset temperatures of the initial

ammonia desorption of 4 NH_3 moles from $Mg(NH_3)_6Cl_2$ and $Mn(NH_3)_6Cl_2$ are observed at 121 °C and 79 °C, respectively. For the solid solution $Mg_{0.5}Mn_{0.5}(NH_3)_6Cl_2$, the onset temperature for the first desorption is 116 °C. The onset temperature for the next NH_3 release is at 179 °C for $Mg_{0.5}Mn_{0.5}(NH_3)_2Cl_2$, significantly lower as compared to 211 °C in $Mg(NH_3)_2Cl_2$ and similar to 179 °C in $Mn(NH_3)_2Cl_2$. The onset temperature of the last NH_3 desorption of $Mg_{0.5}Mn_{0.5}(NH_3)Cl_2$ is 276 °C, which is lower than the last desorption event onset temperature of $Mg(NH_3)Cl_2$ – 289 °C. $Mn(NH_3)Cl_2$ starts desorbing the last mole of NH_3 at 257 °C.

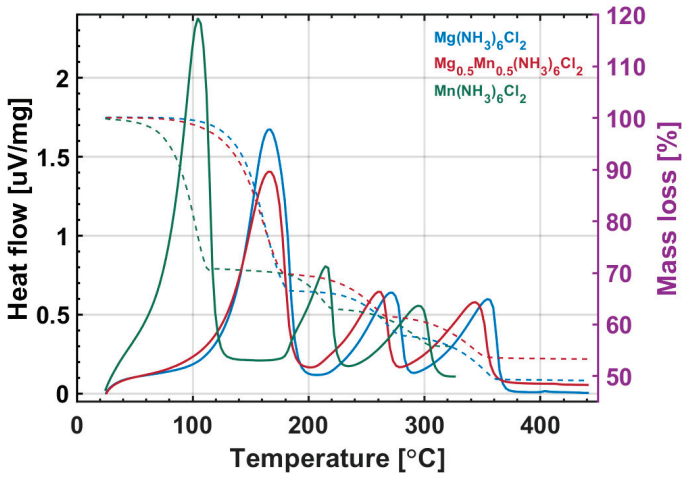

Figure 3. TGA-DSC of $Mg(NH_3)_6Cl_2$, $Mg_{0.5}Mn_{0.5}(NH_3)_6Cl_2$ and $Mn(NH_3)_6Cl_2$ measured from RT to 450 °C, $\Delta T/\Delta t = 5$ °C·min^{-1}.

Each NH_3 desorption step is followed by mass loss. In the first desorption step, 4 NH_3 moles are released and $Mg_{0.5}Mn_{0.5}(NH_3)_6Cl_2$ experience a 30.2% mass loss, while the next two desorption events reduce the mass of the sample by 8.3% and 8.1%, respectively. The mass loss ratio 4:1:1 of the monometallic and mixed hexammines (Supporting Information, Table S2) corresponds to the moles of NH_3 desorbed in each desorption event, i.e., four moles of NH_3 released in the first desorption step, and 1 mole of NH_3 released in the second and third step, respectively, and agrees well with the theoretical weight loss expected from the NH_3 desorption. The gravimetric NH_3 capacities for the monometallic and the mixed cation hexammines are presented in Table S3. SR-PXD data measured of $Mg_{1-x}Mn_x(NH_3)_6Cl_2$, (x = 0, 0.025, 0.05, 0.1, 0.3 and 0.5) after the TGA-DSC measurements confirm the reformation of $Mg_{1-x}Mn_xCl_2$ after full NH_3 release, thus confirming the stability of the solid solution (Supporting Information, Figure S7).

Kissinger analysis was performed on the DSC heat flow signals for the three desorption events measured for $Mg(NH_3)_6Cl_2$, $Mn(NH_3)_6Cl_2$ and $Mg_{0.5}Mn_{0.5}(NH_3)_6Cl_2$ to determine the activation energy and investigate their NH_3 desorption kinetics. Kissinger plots for the three endothermic events with the release of 4, 1 and 1 moles of NH_3 are shown in Figure 4a–c. The corresponding activation energies were calculated for each desorption event and are presented in Figure 4d-f. The activation energy of the first four moles of NH_3 desorption from $Mg_{0.5}Mn_{0.5}(NH_3)_6Cl_2$ is 54.8 kJ·mol^{-1}, which is approximately in between that of $Mg(NH_3)_6Cl_2$ (E_a = 60.8 kJ·mol^{-1}) and $Mn(NH_3)_6Cl_2$ (E_a = 43.5 kJ·mol^{-1}). For the second NH_3 desorption step, the activation energy for $Mg_{0.5}Mn_{0.5}(NH_3)_2Cl_2$ is 73.2 kJ·mol^{-1}, in between that of $Mg(NH_3)_2Cl_2$ (E_a = 74.8 kJ·mol^{-1}) and $Mn(NH_3)_2Cl_2$ (E_a = 67.7 kJ·mol^{-1}). The final desorption event of $Mg_{0.5}Mn_{0.5}(NH_3)Cl_2$ has an activation energy of 91.0 kJ·mol^{-1}, as compared to $Mg(NH_3)Cl_2$ (E_a = 91.8 kJ·mol^{-1}) and $Mn(NH_3)Cl_2$ (E_a = 90.9 kJ·mol^{-1}).

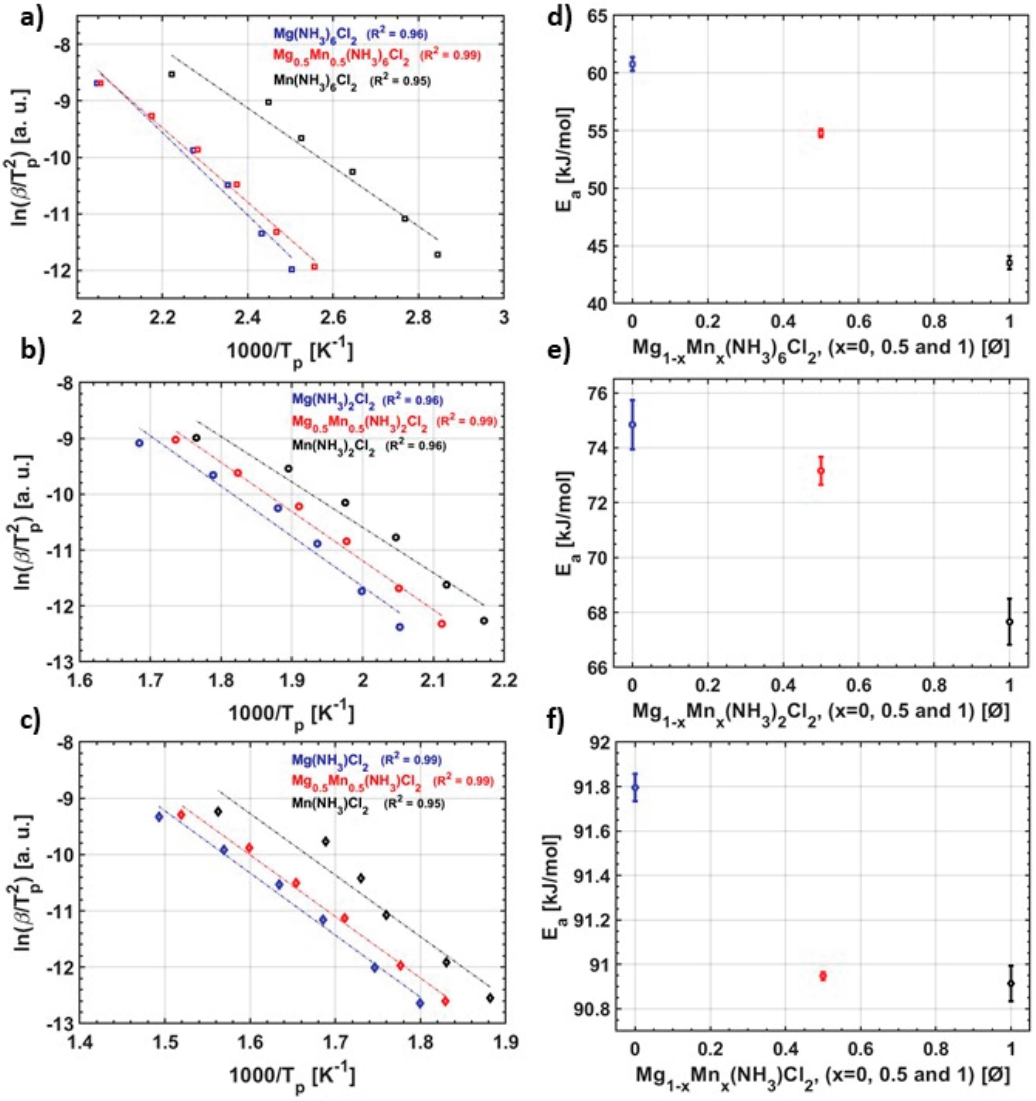

Figure 4. Kissinger analysis of the three desorption events occurring in $Mg(NH_3)_6Cl_2$ (blue), $Mg_{0.5}Mn_{0.5}(NH_3)_6Cl_2$ (red) and $Mn(NH_3)_6Cl_2$ (black). The left column (**a**–**c**) shows the Kissinger plot which corresponds to the release of a) 4 NH_3 b) 1 NH_3 and c) 1 NH_3. β is the heating rate and T_p is the corresponding peak temperature. The right column (**d**–**f**) shows the corresponding activation energies (E_a) for the three desorption events as determined by the Kissinger method. The R-values for each linear fit are included in the graphs.

The activation energies for $Mg_{0.5}Mn_{0.5}(NH_3)_6Cl_2$ in all three desorption events are significantly lower as compared to monometallic $Mg(NH_3)_6Cl_2$. Therefore, by obtaining the mixed metal halide ammines, it is possible to tailor the desorption temperature and kinetics of the mixed metal halide ammines compared to the monometallic halide ammines.

3.3. In Situ SR-PXD

The in situ SR-PXD data for $Mg_{0.5}Mn_{0.5}(NH_3)_6Cl_2$ in the temperature range RT to 402 °C, with a heating rate of 5 °C·min^{-1}, are shown in Figure 5a, while Figure 5b shows diffraction patterns at selected temperatures for each of the ammoniated compounds observed during heating. Rietveld refinements of the mixed metal hexammines are presented in the supporting material (Figures S1-S5). The in situ SR-PXD data from RT for monometallic $Mg(NH_3)_6Cl_2$ is shown in the supporting material (Figure S6). SR-PXD data at RT contain Bragg peaks from $Mg_{0.5}Mn_{0.5}(NH_3)_6Cl_2$ (97.6(6) wt%) and $Mg_{0.5}Mn_{0.5}(NH_3)_2Cl_2$ (2.4(5) wt%). Upon heating, the Bragg peaks corresponding to $Mg_{0.5}Mn_{0.5}(NH_3)_6Cl_2$ disappear between 115 and 125 °C, while peaks corresponding to

$Mg_{0.5}Mn_{0.5}(NH_3)_2Cl_2$ increase significantly in intensity. Upon further heating, the Bragg peaks corresponding to $Mg_{0.5}Mn_{0.5}(NH_3)_2Cl_2$ decrease in intensity from ~230 °C and peaks from $Mg_{0.5}Mn_{0.5}(NH_3)Cl_2$ appear at ~246 °C. The peaks from $Mg_{0.5}Mn_{0.5}(NH_3)Cl_2$ disappear at 325 °C and some Bragg peaks from an unknown compound appear at 328 °C (Figure 5b, yellow diffraction pattern) before the full desorption of NH_3 and formation of the $Mg_{0.5}Mn_{0.5}Cl_2$ solid solution. The appearance of unknown diffraction peaks might be due to a non-stoichiometric transition from the $Mg_{0.5}Mn_{0.5}(NH_3)Cl_2$ monoammine to the $Mg_{0.5}Mn_{0.5}Cl_2$ chloride. Such behavior was previously reported for $Mn(NH_3)Cl_2$, which was observed to release the last NH_3 via two or more desorption events [13,42]. This is also observed in our data from the Sieverts measurements and will be discussed later in Section 3.4.

In situ SR-PXD data for $Mn(NH_3)_6Cl_2$ in the temperature range RT to 406 °C, with a heating rate of 5 °C·min^{-1} confirms the presence of such intermediate phase at 307 °C (Figure S9). However, due to the fast heating rate and, therefore, dominant peaks from $Mn(NH_3)Cl_2$ and $MnCl_2$ phases in the diffraction pattern, it was challenging to index it and extract the unit cell parameters for $Mn(NH_3)_{1-\delta}Cl_2$. The same applies for the diffraction pattern of possible $Mg_{0.5}Mn_{0.5}(NH_3)_{1-\delta}Cl_2$ phase at 328 °C from the in situ data for $Mg_{0.5}Mn_{0.5}(NH_3)_6Cl_2$ (Figure 5), where the dominant diffraction peaks from $Mg_{0.5}Mn_{0.5}(NH_3)Cl_2$ make the indexing challenging. Observation of these intermediate diffraction patterns suggests that the transition of $Mn(NH_3)Cl_2$ to $MnCl_2$ and $Mg_{0.5}Mn_{0.5}(NH_3)Cl_2$ to $Mg_{0.5}Mn_{0.5}Cl_2$, which was described as non-stoichiometric process [42], in our study undergoes by stoichiometric NH_3 releases of δ moles.

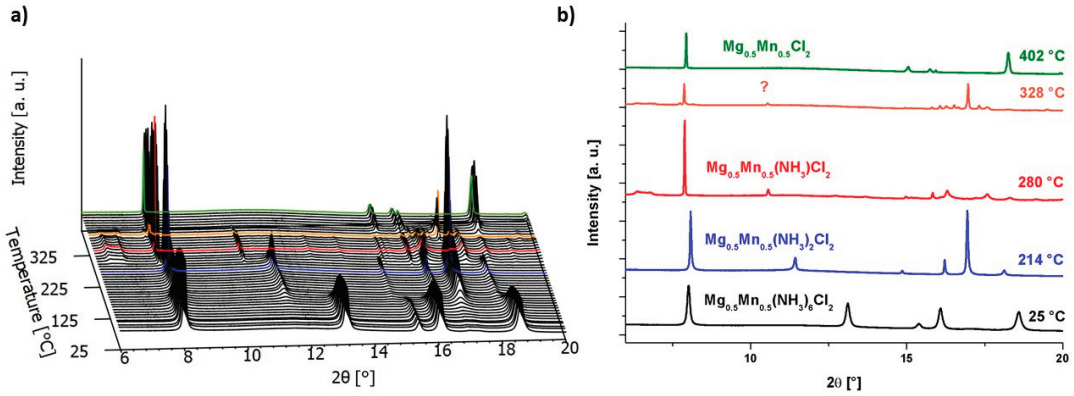

Figure 5. (a) In situ SR-PXD of $Mg_{0.5}Mn_{0.5}(NH_3)_6Cl_2$ measured from RT to 402 °C with a heating rate of 5 °C·min^{-1}and λ = 0.82646 Å and (**b**) SR-PXD data at specific temperatures.

The NH_3 desorption temperatures are decreased significantly for $Mg_{0.5}Mn_{0.5}(NH_3)_6Cl_2$ as compared to monometallic $Mg(NH_3)_6Cl_2$ (Figure S8), confirming the results from TGA-DSC analysis. The first NH_3 desorption step of $4NH_3$ moles and transformation from $Mg_{0.5}Mn_{0.5}(NH_3)_6Cl_2$ to $Mg_{0.5}Mn_{0.5}(NH_3)_2Cl_2$ (T = 125 °C) is 20 °C lower than observed for $Mg(NH_3)_6Cl_2$ (T = 146 °C). All NH_3 is desorbed from $Mg_{0.5}Mn_{0.5}(NH_3)_6Cl_2$ at T = 337 °C, significantly lower than reported for $Mg(NH_3)Cl_2$ (T = 375 °C) [15]. The first desorption step of $Mg(NH_3)_6Cl_2$ at 146 °C is similar to the temperature reported in the literature (T = 142 °C) [15].

Rietveld refinements of the hexa-, di-, monoammine and chloride are shown in Figure 6, and Table 2 summarizes their structural information.

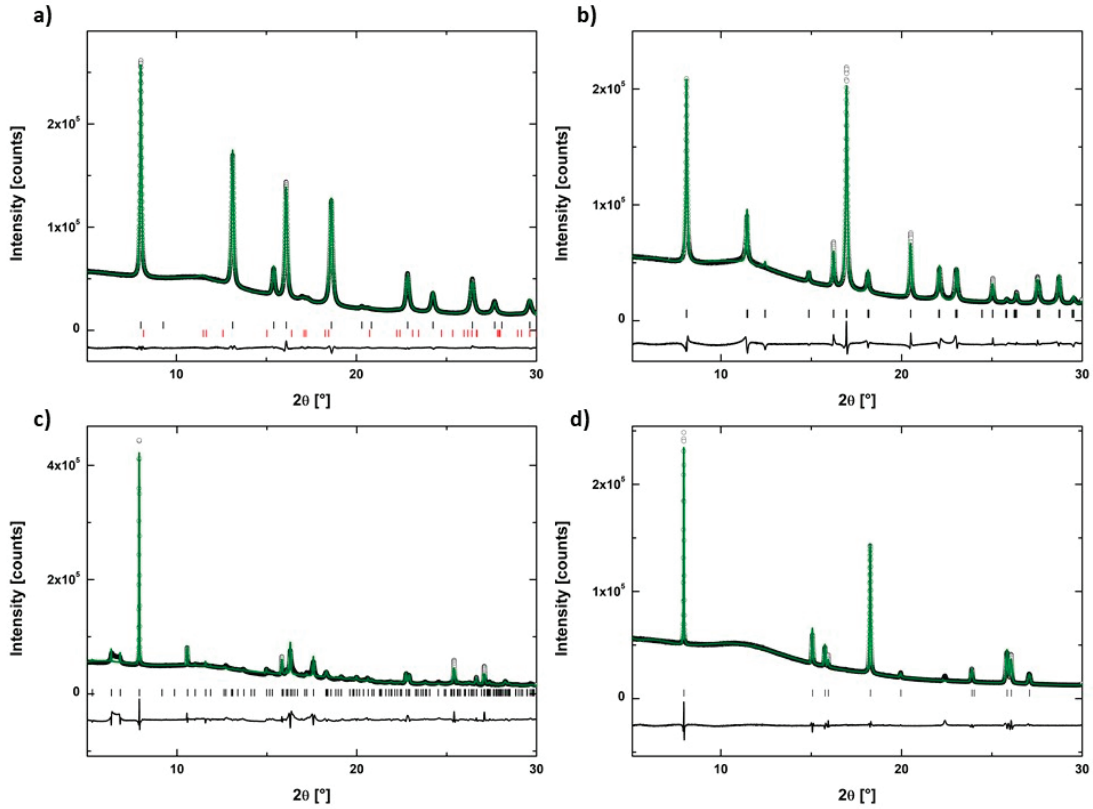

Figure 6. Rietveld refinements of the SR-PXD data for (**a**) $Mg_{0.5}Mn_{0.5}(NH_3)_6Cl_2$ at RT (R_{wp} = 1.48 %), (**b**) $Mg_{0.5}Mn_{0.5}(NH_3)_2Cl_2$ at 214 °C (R_{wp} = 3.17 %), (**c**) $Mg_{0.5}Mn_{0.5}(NH_3)Cl_2$ at 280 °C (R_{wp} = 5.02 %), and (**d**) $Mg_{0.5}Mn_{0.5}Cl_2$ at 402 °C (R_{wp} = 3.19 %); showing the experimental (black circles), calculated (solid green line) and the difference plot (solid black line). The vertical ticks mark the Bragg peak positions for the corresponding compounds. λ=0.82646 Å. In (a) vertical ticks mark $Mg_{0.5}Mn_{0.5}(NH_3)_6Cl_2$ (97.6(6) wt%, black) and $Mg_{0.5}Mn_{0.5}(NH_3)_2Cl_2$ (2.4(5) wt%, red).

Rietveld refinement of $Mg_{0.5}Mn_{0.5}(NH_3)_6Cl_2$ at RT is performed using the structural model of $Mg(NH_3)_6Cl_2$ (Figure 6a). Two phases are present in the sample, which are identified as $Mg_{0.5}Mn_{0.5}(NH_3)_6Cl_2$ and $Mg_{0.5}Mn_{0.5}(NH_3)_2Cl_2$ with the refined phase fractions to 97.6(6) wt% and 2.4(5) wt%, respectively, which might be resulted from partial NH_3 release at RT. $Mg_{0.5}Mn_{0.5}(NH_3)_6Cl_2$ crystallizes in a cubic unit cell, a = 10.22037(8) Å at RT with space group *Fm*-3*m* and is isostructural to $Mg(NH_3)_6Cl_2$. Octahedral $Mg_{0.5}Mn_{0.5}(NH_3)_6$ complexes are contained in a cubic lattice of Cl atoms, with each $Mg_{0.5}Mn_{0.5}$ atom octahedrally coordinated by six N atoms.

$Mg_{0.5}Mn_{0.5}(NH_3)_2Cl_2$ was refined using the $Mg(NH_3)_2Cl_2$ structure as a starting point. Figure 6b shows the Rietveld refinement of the SR-PXD data for $Mg_{0.5}Mn_{0.5}(NH_3)_2Cl_2$ at 214 °C. For the diammine $Mg_{0.5}Mn_{0.5}(NH_3)_2Cl_2$, space group *Cmmm* [43], each Cl atom is shared by two neighboring $Mg_{0.5}Mn_{0.5}$ atoms in edge-sharing octahedral chains.

The monoammine $Mg_{0.5}Mn_{0.5}(NH_3)Cl_2$ is isostructural to $Ni(NH_3)Cl_2$, which crystallizes in a monoclinic unit cell with space group *I*2/*m* [44] where each Cl atom is shared by three $Mg_{0.5}Mn_{0.5}$ atoms in edge-sharing double octahedral chains. Both broad and narrow diffraction peaks are observed for the monoammine phase (see Figure 6c), indicating the presence of structural disorder or stacking faults in the structure, resulting in a marked difference between the experimental and calculated patterns.

The Rietveld refinement of the fully desorbed $Mg_{0.5}Mn_{0.5}Cl_2$ at 402 °C is shown in Figure 6d. $Mg_{0.5}Mn_{0.5}Cl_2$ structure, space group *R*-3*m*, is formed by the octahedra of Cl atoms with central $Mg_{0.5}Mn_{0.5}$ atoms sharing half of their edges, and thus resulting in layers of $Mg_{0.5}Mn_{0.5}Cl_2$.

Table 2. Structural parameters for the present $Mg_{0.5}Mn_{0.5}(NH_3)_yCl_2$ (y = 6, 2, 1 and 0) phases investigated in this study.

Chemical Formula	**$Mg_{0.5}Mn_{0.5}(NH_3)_6Cl_2$**	**$Mg_{0.5}Mn_{0.5}(NH_3)_2Cl_2$**	**$Mg_{0.5}Mn_{0.5}(NH_3)Cl_2$**	**$Mg_{0.5}Mn_{0.5}Cl_2$**
T (°C)	RT	214	280	402
Crystal system	Cubic	Orthorhombic	Monoclinic	Trigonal*
Space group	*Fm-3m*	*Cmmm*	*I2/m*	*R-3m*
a (Å)	10.22037(8)	8.258(5)	15.575(1)	3.69494(3) Å
b (Å)	-	8.290(4)	3.756(1)	-
c (Å)	-	3.812(2)	14.453(1)	17.8698(4)
β (°)	-	-	106.55(3)	-
V (Å^3)	1067.58(3)	261.0(2)	810.6(9)	211.28(6)
Z	4	2	8	3

* Hexagonal parameters are used in this work.

3.4. NH_3 Cycling and Kinetics

Studies of the NH_3 sorption kinetics and cyclability of the pristine and mixed metal halides with the lower and higher Mn contents ($Mg_{0.9}Mn_{0.1}Cl_2$ and $Mg_{0.5}Mn_{0.5}Cl_2$) were performed using a Sieverts apparatus. The results from the desorption cycles performed on $Mg_{0.9}Mn_{0.1}(NH_3)_6Cl_2$ are presented in the supporting information (Figure S10). The fifth NH_3 absorption process (after four cycles) of pristine $MgCl_2$, $MnCl_2$ and $Mg_{0.5}Mn_{0.5}Cl_2$ are presented in Figure 7. For absorption, the applied NH_3 gas pressure was ~2.5 bar and the processes were conducted at RT. The moles of absorbed NH_3 were calculated (see Equation 1), where Δn is calculated from the pressure drop, ΔP, occurring during NH_3 absorption. The observed pressure drop was ΔP = 0.33 bar and the final pressures at the end of absorption were 2.21 and 2.22 bar for $MgCl_2$ and $Mg_{0.5}Mn_{0.5}Cl_2$, respectively. $MnCl_2$ only absorbed 5.5 moles of NH_3, which corresponds to a pressure drop of only ΔP = 0.29 bar reaching a final pressure P = 2.23 bar. This indicated that not all the $MnCl_2$ powder had reacted with NH_3, despite the still relatively high value of the final pressure of absorption. Indeed, due to the large volume expansion of the metal chloride during ammonia absorption, some clogging may occur and prevent ammonia from reaching all the salt crystals [16]. On the other, it cannot be excluded that that the absorption reaction stops because the equilibrium pressure for $Mn(NH_3)_6Cl_2$ at RT is higher than the final pressure reached during absorption (P = 2.23 bar). A more detailed thermodynamic study using pressure-composition-isotherms is needed to clarify this in detail. $MgCl_2$ absorbed 6 moles of NH_3 in less than 1000 seconds, while $Mg_{0.5}Mn_{0.5}Cl_2$ absorbed 6 moles of NH_3 in 6000 seconds. Similarly, the NH_3 absorption rate for the pristine halides are very different: Four moles of NH_3 is absorbed in $MgCl_2$ in about 200 seconds, while it took about 800 seconds to absorb the similar amount of NH_3 in $MnCl_2$. The rate of absorption for $Mg_{0.5}Mn_{0.5}Cl_2$ is similar to that of $MnCl_2$, indicating that Mn plays a predominant role for governing the kinetics of the hexammine formation.

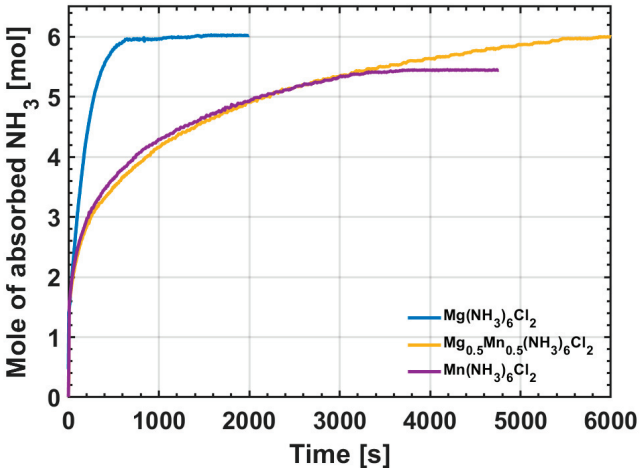

Figure 7. NH_3 absorption processes of $Mg(NH_3)_6Cl_2$ (blue), $Mg_{0.5}Mn_{0.5}(NH_3)_6Cl_2$ (yellow) and $Mn(NH_3)_6Cl_2$ (purple).

The NH_3 desorption processes during cycling were carried out upon heating with a constant heating rate of 2 °C·min^{-1} from RT to 350 °C under an initial NH_3 pressure of 1 bar, see Figure 8. The moles of desorbed NH_3 were calculated using Equation 1 and the pressure increase, ΔP = 0.32 bar, due to NH_3 release. The three desorption steps of NH_3 were observed as a pressure increase and Δn was calculated. For $Mg_{0.5}Mn_{0.5}(NH_3)_2Cl_2$, the first 4 moles of NH_3 starts desorbing at around 100 °C and are fully released at 166 °C. The resulting $Mg_{0.5}Mn_{0.5}(NH_3)_2Cl_2$ desorbs one mole of NH_3 in the temperature range from 240 °C to 260 °C, forming $Mg_{0.5}Mn_{0.5}(NH_3)Cl_2$. The final NH_3 desorption step occurs above 300 °C. However, the transformation from monoammine to fully desorbed mixed metal chloride, $Mg_{0.5}Mn_{0.5}Cl_2$, does not proceed via a single step as for the previous desorption. Instead it undergoes through two discrete steps, consistent with the observations of a different crystalline phase in the in situ SR-PXD experiments.

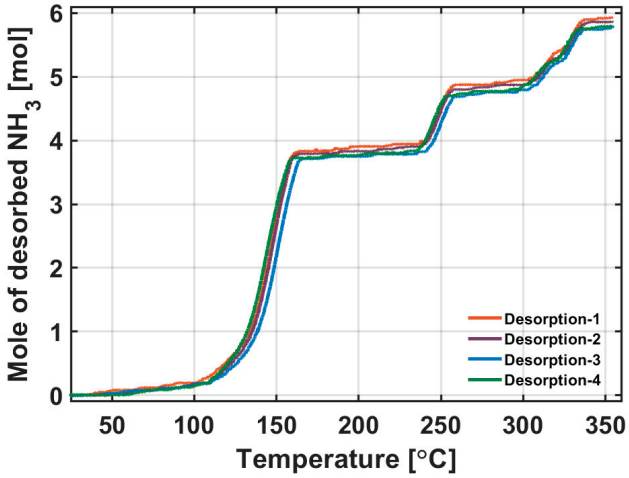

Figure 8. A series of NH_3 desorption from $Mg_{0.5}Mn_{0.5}(NH_3)_6Cl_2$. The four cycles confirm the stability and cyclability of the mixed metal halide after several ab/desorption cycles.

For some hexammines, $M(NH_3)_6Cl_2$ (M = Mg, Ni), the desorption consists of three events [13]. In contrast, $Mn(NH_3)_6Cl_2$ was reported to undergo non-stoichiometric NH_3 release in the last desorption step [13,42]. In our study, we observe two separate steps, and from the number of desorbed NH_3 moles calculated from ΔP in Sieverts studies, δ seems to be equal to 0.5. Furthermore, the NH_3 desorption studies of $Mg_{0.9}Mn_{0.1}(NH_3)_6Cl_2$ (Figure S10) suggest that this phenomenon does not occur in $Mg_{1-x}Mn_x(NH_3)_6Cl_2$ with low Mn content, as the last decomposition step occurs as a single event.

This indicates that sufficiently high amount of Mn in $Mg_{1-x}Mn_x(NH_3)_6Cl_2$ results in a change in the physical behavior to be similar to that of $Mn(NH_3)_6Cl_2$.

These results suggest that by changing the relative Mg:Mn ratio in $Mg_{1-x}Mn_x(NH_3)_6Cl_2$ the NH_3 sorption propertied can be tuned and optimized. For instance, substituting Mg in $Mn(NH_3)_6Cl_2$ increases its stability, avoiding NH_3 desorption at RT. Furthermore, due to the low weight of Mg, the gravimetric capacity increases, with increasing Mg content. Finally, increasing the relative content of magnesium can be beneficial if cost reduction is desirable.

A thorough investigation of the NH_3 desorption reaction enthalpies is planned for further thermodynamic studies of the $Mg_{1-x}Mn_x(NH_3)_6Cl_2$ hexammines by applying pressure composition isotherm (PCI) studies.

4. Conclusions

A series of novel mixed metal halide ammines, $Mg_{1-x}Mn_x(NH_3)_6Cl_2$, with a usable ammonia capacity in the temperature range 20-350 °C were synthesized and characterized. The crystal structures of the different ammine phases are identified and investigated by in situ SR-PXD. All $Mg_{1-x}Mn_x(NH_3)_6Cl_2$ solid solutions crystallize in a cubic unit cell with space group symmetry *Fm*-3*m* and unit cell parameters intermediate that of the two monometallic materials, $Mg(NH_3)_6Cl_2$ and $Mn(NH_3)_6Cl_2$. DSC analysis reveal a decrease in the onset temperature for NH_3 desorption for the solid solutions as compared to the monometallic $Mg(NH_3)_6Cl_2$. Activation energies for each desorption step are calculated and show the possibility of tailoring the activation energies for the NH_3 release in mixed metal chloride hexammines. The lower activation energies for NH_3 desorption in $Mn(NH_3)_6Cl_2$ resulted in a lowering of the activation energies for the solid solution $Mg_{0.5}Mn_{0.5}(NH_3)_6Cl_2$. Finally, NH_3 reversibility measurements reveal that the solid solution has a high stability, thus making them promising candidates for solid-state NH_3 storage systems.

Supplementary Materials: The following are available online at www.mdpi.com/1996-1073/13/11/2746/s1, Table S1: Structural parameters for the $MgCl_2$, $MnCl_2$ and $Mg_{1-x}Mn_xCl_2$ (x = 0.025, 0.05, 0.1, 0.3 and 0.5) solid solutions obtained for this study, Figure S1: Rietveld refinement of SR-PXD data of $Mg(NH_3)_6Cl_2$ at RT, Figure S2: Rietveld refinement of SR-PXD data of $Mg_{0.95}Mn_{0.05}(NH_3)_6Cl_2$ at RT, Figure S3: Rietveld refinement of SR-PXD data of $Mg_{0.9}Mn_{0.1}(NH_3)_6Cl_2$ at RT, Figure S4: Rietveld refinement of SR-PXD data of $Mg_{0.7}Mn_{0.3}(NH_3)_6Cl_2$ at RT, Figure S5: Rietveld refinement of SR-PXD data of $Mn(NH_3)_6Cl_2$ at RT, Figure S6: DSC measurements performed on $Mg(NH_3)_6Cl_2$, $Mn(NH_3)_6Cl_2$ and $Mg_{1-x}Mn_x(NH_3)_6Cl_2$, Table S2: The NH_3 desorption onset temperatures of $Mg(NH_3)_6Cl_2$, $Mn(NH_3)_6Cl_2$ and $Mg_{1-x}Mn_x(NH_3)_6Cl_2$, Table S3: The gravimetric NH_3 capacities of the monometallic and mixed cation hexammines investigated in this study, Figure S7: SR-PXD patterns of $Mg_{1-x}Mn_xCl_2$ after one cycle of NH_3 absorption and desorption, Figure S8: In-situ SR-PXD of $Mg(NH_3)_6Cl_2$ measured from RT to 227 °C, Figure S9: In-situ SR-PXD of $Mn(NH_3)_6Cl_2$ measured from RT to 406 °C, Figure S10: NH_3 desorption upon cycling of $Mg_{0.9}Mn_{0.1}(NH_3)_6Cl_2$.

Author Contributions: Conceptualization, P.B., S.D. and D.B.; methodology, P.B., R.E.J., S.D. and D.B.; formal analysis, P.B., J.B.G. and A.K.; investigation, P.B., J.B.G. and A.K; resources, D.B. and S.D.; data curation, P.B.; writing—original draft preparation, P.B.; writing—review and editing, A.K., J.B.G., R.E.J., D.B., B.C.H. and S.D.; visualization, P.B.; supervision, B.C.H. and S.D.; project administration, D.B.; funding acquisition, D.B. and S.D. All authors have read and agreed to the published version of the manuscript.

Funding: The Nordic Neutron Science Programme from NordForsk is acknowledged for financial support via the project NHS (No. 82206).

Acknowledgments: J. B. Grinderslev gratefully acknowledges NordForsk for financial support via the NNSP project FunHy (No. 81942). The authors are also grateful to the X04SA beamline at the Swiss light source, Villigen, Switzerland and the local contact Antonio Cervellino for assistance with data collection and the beamline I11 at the Diamond light source, Oxford, UK and the local contacts Stephen Thompson and Chiu Tang for assistance with data collection.

Conflicts of Interest: The authors declare no conflict of interest.

References

1. Mohtadi, R.; Orimo, S. The renaissance of hydrides as energy materials. *Nat. Rev. Mater.* **2016**, *2*, 1–15, doi:10.1038/natrevmats.2016.91.
2. He, T.; Pachfule, P.; Wu, H.; Xu, Q.; Chen, P. Hydrogen carriers. *Nat. Rev. Mater.* **2016**, *1*, 1–17, doi:10.1038/natrevmats.2016.59.
3. Milanese, C.; Jensen, T.R.; Hauback, B.C.; Pistidda, C.; Dornheim, M.; Yang, H.; Lombardo, L.; Zuettel, A.; Filinchuk, Y.; Ngene, P.; et al. Complex hydrides for energy storage. *Int. J. Hydrog. Energy* **2019**, *44*, 7860–7874, doi:10.1016/j.ijhydene.2018.11.208.
4. Hirscher, M.; Yartys, V.A.; Baricco, M.; Bellosta von Colbe, J.; Blanchard, D.; Bowman, R.C.; Broom, D.P.; Buckley, C.E.; Chang, F.; Chen, P.; et al. Materials for hydrogen-based energy storage—Past, recent progress and future outlook. *J. Alloys Compd.* **2020**, *827*, 153548, doi:10.1016/j.jallcom.2019.153548.
5. Zamfirescu, C.; Dincer, I. Ammonia as a green fuel and hydrogen source for vehicular applications. *Fuel Process. Technol.* **2009**, *90*, 729–737, doi:10.1016/j.fuproc.2009.02.004.
6. Lan, R.; Irvine, J.T.S.; Tao, S. Ammonia and related chemicals as potential indirect hydrogen storage materials. *Int. J. Hydrog. Energy* **2012**, *37*, 1482–1494, doi:10.1016/j.ijhydene.2011.10.004.
7. Zamfirescu, C.; Dincer, I. Using ammonia as a sustainable fuel. *J. Power Sources* **2008**, *185*, 459–465, doi:10.1016/j.jpowsour.2008.02.097.
8. Christensen, C.H.; Johannessen, T.; Sørensen, R.Z.; Nørskov, J.K. Towards an ammonia-mediated hydrogen economy? *Catal. Today* **2006**, *111*, 140–144, doi:10.1016/j.cattod.2005.10.011.
9. Makepeace, J.W.; He, T.; Weidenthaler, C.; Jensen, T.R.; Chang, F.; Vegge, T.; Ngene, P.; Kojima, Y.; de Jongh, P.E.; Chen, P.; et al. Reversible ammonia-based and liquid organic hydrogen carriers for high-density hydrogen storage: Recent progress. *Int. J. Hydrog. Energy* **2019**, *44*, 7746–7767, doi:10.1016/j.ijhydene.2019.01.144.
10. Kubota, M.; Matsuo, K.; Yamanouchi, R.; Matsuda, H. Absorption and Desorption Characteristics of NH_3 with Metal Chlorides for Ammonia Storage. *J. Chem. Eng. Jpn.* **2014**, doi:10.1252/jcej.13we294.
11. Klerke, A.; Christensen, C.H.; Nørskov, J.K.; Vegge, T. Ammonia for hydrogen storage: Challenges and opportunities. *J. Mater. Chem.* **2008**, *18*, 2304–2310, doi:10.1039/B720020J.
12. Christensen, C.H.; Sørensen, R.Z.; Johannessen, T.; Quaade, U.J.; Honkala, K.; Elmøe, T.D.; Køhler, R.; Nørskov, J.K. Metal ammine complexes for hydrogen storage. *J. Mater. Chem.* **2005**, *15*, 4106–4108, doi:10.1039/B511589B.
13. Sørensen, R.Z.; Hummelshøj, J.S.; Klerke, A.; Reves, J.B.; Vegge, T.; Nørskov, J.K.; Christensen, C.H. Indirect, Reversible High-Density Hydrogen Storage in Compact Metal Ammine Salts. *J. Am. Chem. Soc.* **2008**, *130*, 8660–8668, doi:10.1021/ja076762c.
14. Jacobsen, H.S.; Hansen, H.A.; Andreasen, J.W.; Shi, Q.; Andreasen, A.; Feidenhans'l, R.; Nielsen, M.M.; Ståhl, K.; Vegge, T. Nanoscale structural characterization of $Mg(NH_3)_6Cl_2$ during NH_3 desorption: An in situ small angle X-ray scattering study. *Chem. Phys. Lett.* **2007**, *441*, 255–260, doi:10.1016/j.cplett.2007.05.001.
15. Walker, G. *Solid-State Hydrogen Storage: Materials and Chemistry*; Woodhead Publishing: Cambridge, England, 2008; ISBN 978-1-84569-494-4.
16. Tekin, A.S.; Hummelshøj, J.S.; Jacobsen, H.; Sveinbjörnsson, D.; Blanchard, D.K.; Nørskov, J.; Vegge, T. Ammonia dynamics in magnesium ammine from DFT and neutron scattering. *Energy Environ. Sci.* **2010**, *3*, 448–456, doi:10.1039/B921442A.
17. Elmøe, T.D.; Sørensen, R.Z.; Quaade, U.; Christensen, C.H.; Nørskov, J.K.; Johannessen, T. A high-density ammonia storage/delivery system based on $Mg(NH_3)_6Cl_2$ for SCR–$DeNO_x$ in vehicles. *Chem. Eng. Sci.* **2006**, *61*, 2618–2625, doi:10.1016/j.ces.2005.11.038.
18. Hwang, I.C.; Drews, T.; Seppelt, K. $Mg(NH_3)_6Hg_{22}$, a Mercury Intercalation Compound. *J. Am. Chem. Soc.* **2000**, *122*, 8486–8489, doi:10.1021/ja000960l.
19. Wentworth, W.E.; Raldow, W.M.; Corbett, G.E. Correlation of thermodynamic properties for dissociation of ammines of divalent metal halides. *Inorg. Chim. Acta* **1978**, *30*, L299–L301, doi:10.1016/S0020-1693(00)88985-9.
20. Bevers, E.; Oonk, H.; Haije, W.; van Ekeren, P. Investigation of thermodynamic properties of magnesium chloride amines by HPDSC and TG. *J. Therm. Anal. Calorim.* **2007**, *90*, 923–929, doi:10.1007/s10973-006-8247-1.
21. Aoki, T.; Miyaoka, H.; Inokawa, H.; Ichikawa, T.; Kojima, Y. Activation on Ammonia Absorbing Reaction for Magnesium Chloride. *J. Phys. Chem. C* **2015**, *119*, 26296–26302, doi:10.1021/acs.jpcc.5b07965.

22. Aoki, T.; Ichikawa, T.; Miyaoka, H.; Kojima, Y. Thermodynamics on Ammonia Absorption of Metal Halides and Borohydrides. *J. Phys. Chem. C* **2014**, *118*, 18412–18416, doi:https://doi.org/10.1021/jp5049474.
23. Eßmann, R.; Kreiner, G.; Niemann, A.; Rechenbach, D.; Schmieding, A.; Sichla, T.; Zachwieja, U.; Jacobs, H. Isotype Strukturen einiger Hexaamminmetall(II)-halogenide von 3d-Metallen: $[V(NH_3)_6]I_2$, $[Cr(NH_3)_6]I_2$, $[Mn(NH_3)_6]Cl_2$, $[Fe(NH_3)_6]Cl_2$, $[Fe(NH_3)_6]Br_2$, $[Co(NH_3)_6]Br_2$ und $[Ni(NH_3)_6]Cl_2$. *Z. Anorg. Allg. Chem.* **1996**, *622*, 1161–1166, doi:10.1002/zaac.19966220709.
24. Lysgaard, S.; Ammitzbøll, A.L.; Johnsen, R.E.; Norby, P.; Quaade, U.J.; Vegge, T. Resolving the stability and structure of strontium chloride amines from equilibrium pressures, XRD and DFT. *Int. J. Hydrog. Energy* **2012**, *37*, 18927–18936, doi:10.1016/j.ijhydene.2012.09.129.
25. Bialy, A.; Jensen, P.B.; Blanchard, D.; Vegge, T.; Quaade, U.J. Solid solution barium–strontium chlorides with tunable ammonia desorption properties and superior storage capacity. *J. Solid State Chem.* **2015**, *221*, 32–36, doi:10.1016/j.jssc.2014.09.014.
26. Kishida, Y.; Aoki, M.; Yamauchi, T. Crystal Structure and NH_3 Desorption Properties of Complex Metal Ammine Chloride. *J. Chem. Eng. Jpn.* **2019**, *52*, 239–242, doi:10.1252/jcej.18we161.
27. Lasocha, W.; Eick, H.A. The structure of $Ca_{0.3}Sr_{0.7}Cl_2$ and $Ca_{0.46}Sr_{0.54}Cl_2$ by the X-ray Rietveld refinement procedure. *J. Solid State Chem.* **1988**, *75*, 175–182, doi:10.1016/0022-4596(88)90314-3.
28. Liu, C.Y.; Aika, K. Ammonia Absorption into Alkaline Earth Metal Halide Mixtures as an Ammonia Storage Material. *Ind. Eng. Chem. Res.* **2004**, *43*, 7484–7491, doi:10.1021/ie049874a.
29. Hodorowicz, S.A.; Eick, H.A. Phase relationships in the system $SrBr_2$ $SrCl_2$. *J. Solid State Chem.* **1982**, *43*, 271–277, doi:10.1016/0022-4596(82)90240-7.
30. Hodorowicz, S.A.; Eick, H.A. An X-ray diffraction study of the $SrBr_xI_{2-x}$ system. *J. Solid State Chem.* **1983**, *46*, 313–320, doi:10.1016/0022-4596(83)90155-X.
31. Černý, R.; Penin, N.; D'Anna, V.; Hagemann, H.; Durand, E.; Růžička, J. $Mg_xMn_{(1-x)}(BH_4)_2$ (x=0–0.8), a cation solid solution in a bimetallic borohydride. *Acta Mater.* **2011**, *59*, 5171–5180, doi:10.1016/j.actamat.2011.04.052.
32. Jepsen, L.H.; Ley, M.B.; Filinchuk, Y.; Besenbacher, F.; Jensen, T.R. Tailoring the Properties of Ammine Metal Borohydrides for Solid-State Hydrogen Storage. *ChemSusChem* **2015**, *8*, 1452–1463, doi:10.1002/cssc.201500029.
33. Kissinger, H.E. Variation of Peak Temperature with Heating Rate in Differential Thermal Analysis. *J. Res. Natl. Bur. Stand.* **1956**, *57*, 217–221.
34. Willmott, P.R.; Meister, D.; Leake, S.J.; Lange, M.; Bergamaschi, A.; Böge, M.; Calvi, M.; Cancellieri, C.; Casati, N.; Cervellino, A.; et al. The Materials Science beamline upgrade at the Swiss Light Source. *J. Synchrotron. Radiat.* **2013**, *20*, 667–682, doi:10.1107/S0909049513018475.
35. Thompson, S.P.; Parker, J.E.; Potter, J.; Hill, T.P.; Birt, A.; Cobb, T.M.; Yuan, F.; Tang, C.C. Beamline I11 at Diamond: A new instrument for high resolution powder diffraction. *Rev. Sci. Instrum.* **2009**, *80*, 075107, doi:10.1063/1.3167217.
36. Pathak, P.D.; Vasavada, N.G. Thermal expansion of NaCl, KCl and CsBr by X-ray diffraction and the law of corresponding states. *Acta Crystallogr. A* **1970**, *26*, 655–658, doi:10.1107/S0567739470001602.
37. Coelho, A.A. TOPAS and TOPAS-Academic: An optimization program integrating computer algebra and crystallographic objects written in C++. *J. Appl. Crystallogr.* **2018**, *51*, 210–218, doi:10.1107/S1600576718000183.
38. Tornero, J.D.; Fayos, J. Single crystal structure refinement of $MnCl_2$. *Z. Krist.* **2015**, *192*, 147–148, doi:10.1524/zkri.1990.192.14.147.
39. Feitknecht, W.; Held, F. Über die Hydroxychloride des Magnesiums. *Helv. Chim. Acta* **1944**, *27*, 1480–1495, doi:10.1002/hlca.194402701189.
40. Shannon, R.D. Revised effective ionic radii and systematic studies of interatomic distances in halides and chalcogenides. *Acta Crystallogr. A* **1976**, *32*, 751–767, doi:10.1107/S0567739476001551.
41. King, H.W. Quantitative size-factors for metallic solid solutions. *J. Mater. Sci.* **1966**, *1*, 79–90, doi:10.1007/BF00549722.
42. Reardon, H.; Hanlon, J.M.; Grant, M.; Fullbrook, I.; Gregory, D.H. Ammonia Uptake and Release in the MnX_2–NH_3 (X = Cl, Br) Systems and Structure of the $Mn(NH_3)_nX_2$ (n = 6, 2) Ammines. *Crystals* **2012**, *2*, 193–212, doi:10.3390/cryst2020193.

43. Leineweber, A.; Friedriszik, M.W.; Jacobs, H. Preparation and Crystal Structures of $Mg(NH_3)_2Cl_2$, $Mg(NH_3)_2Br_2$, and $Mg(NH_3)_2I_2$. *J. Solid State Chem.* **1999**, *147*, 229–234, doi:10.1006/jssc.1999.8238.
44. Leineweber, A.; Jacobs, H.; Ehrenberg, H. Crystal Structure of $Ni(NH_3)Cl_2$ and $Ni(NH_3)Br_2$. *Z. Anorg. Allg. Chem.* **2000**, *626*, 2146–2152, doi:10.1002/1521-3749(200010)626:10<2146::AID-ZAAC2146>3.0.CO;2-H.

Supporting Information (SI): Synthesis, structure and NH_3 sorption properties of mixed $Mg_{1-x}Mn_x(NH_3)_6Cl_2$ ammines

Perizat Berdiyeva[a], Anastasiia Karabanova[b], Jakob B. Grinderslev[c], Rune E. Johnsen[b], Didier Blanchard[b], Bjørn C. Hauback[a] and Stefano Deledda[a]*

Stefano.deledda@ife.no, tel: +47 407 26 921

[a)] *Department for Neutron Materials Characterization, Institute for Energy Technology, P.O. Box 40, NO-2027, Kjeller, Norway*

[b)] *Department of Energy Conversion and Storage, Technical University of Denmark, Fysikvej, DK-2800, Lyngby, Denmark*

[c)] *Center for Materials Crystallography, Interdisciplinary Nanoscience Center (iNANO) and Department of Chemistry, Aarhus University, Langelandsgade 140, 8000 Aarhus C, Denmark*

Table S1. Structural parameters for the $MgCl_2$, $MnCl_2$ and $Mg_{1-x}Mn_xCl_2$ (x = 0.025, 0.05, 0.1, 0.3 and 0.5) solid solutions obtained for this study.*

Compound	**Space group**	**a, b (Å)**	**c (Å)**	**V (Å^3)**
$MgCl_2$	R-3m	3.640(3)	17.675(1)	202.875(3)
$Mg_{0.975}Mn_{0.025}Cl_2$	R-3m	3.639(7)	17.680(5)	202.854(1)
$Mg_{0.95}Mn_{0.05}Cl_2$	R-3m	3.639(9)	17.681(6)	202.887(1)
$Mg_{0.9}Mn_{0.1}Cl_2$	R-3m	3.634(6)	17.633(3)	203.217(8)
$Mg_{0.7}Mn_{0.3}Cl_2$	R-3m	3.652(1)	17.662(1)	204.095(3)
$Mg_{0.5}Mn_{0.5}Cl_2$	R-3m	3.668(4)	17.637(3)	205.601(6)
$MnCl_2$	R-3m	3.71(2)	17.59(7)	209.79(4)

**All unit cell parameters are obtained at RT.*

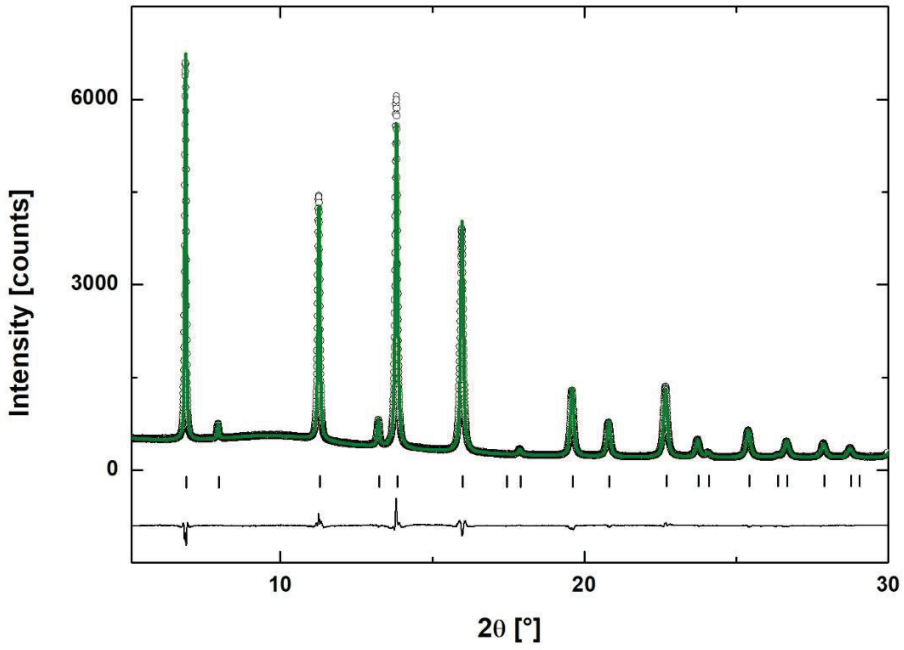

Figure S1. Rietveld refinement of SR-PXD data of $Mg(NH_3)_6Cl_2$ at RT, showing the experimental (black circles), calculated (solid green line) and a difference plot (solid black line) below. The vertical ticks mark the Bragg peak positions for $Mg(NH_3)_6Cl_2$. R_{wp} = 2.22 %. λ= 0.709396 Å

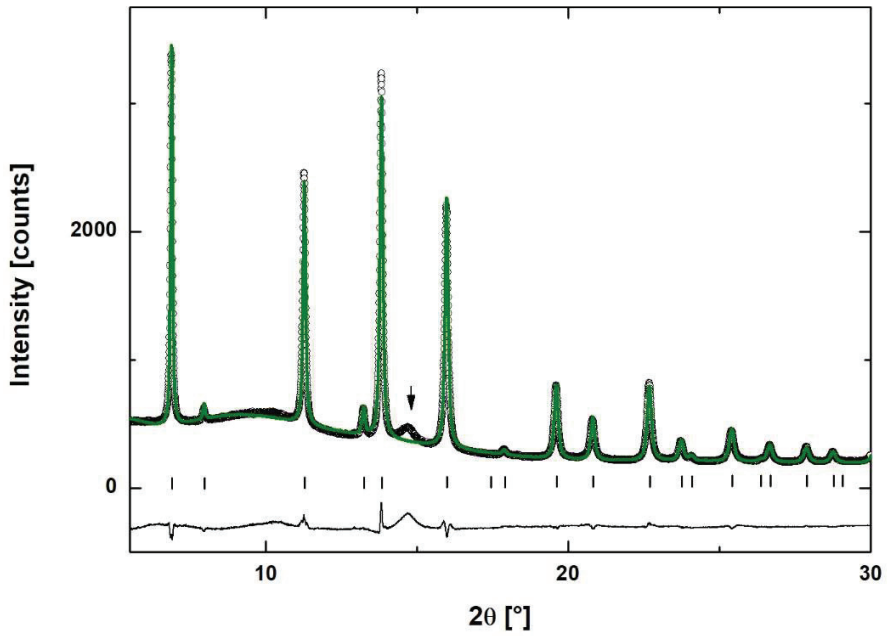

Figure S2. Rietveld refinement of SR-PXD *data of* $Mg_{0.95}Mn_{0.05}(NH_3)_6Cl_2$ *at RT showing the experimental (black circles), calculated (solid green line) and a difference plot (solid black line) below. The vertical ticks mark the Bragg peak positions for* $Mg_{0.95}Mn_{0.05}(NH_3)_6Cl_2$*. The black arrow is pointing at a peak which is likely coming from an impurity oxide phase.* R_{wp} *= 3.58 %.* λ*=0.82646 Å*

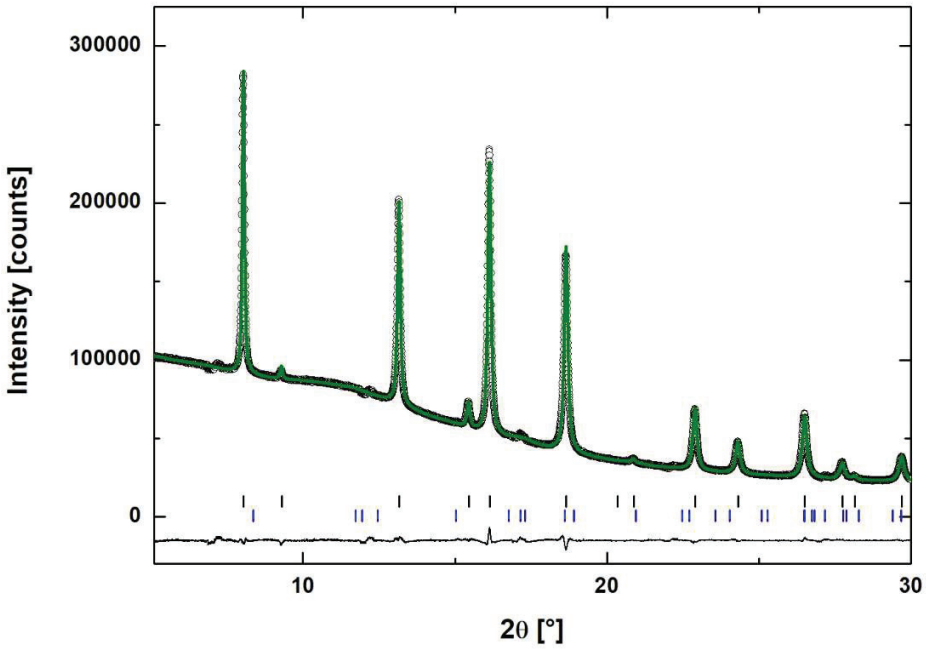

Figure S3. Rietveld refinement of SR-PXD *data of* $Mg_{0.9}Mn_{0.1}(NH_3)_6Cl_2$ *at RT showing the experimental (black circles), calculated (solid green line) and a difference plot (solid black line) below. The vertical ticks mark the Bragg peak positions for* $Mg_{0.9}Mn_{0.1}(NH_3)_6Cl_2$ *(black) and* $Mg_{0.9}Mn_{0.1}(NH_3)_2Cl_2$ *(blue vertical ticks).* R_{wp} *= 1.32 %.* λ*=0.82646 Å*

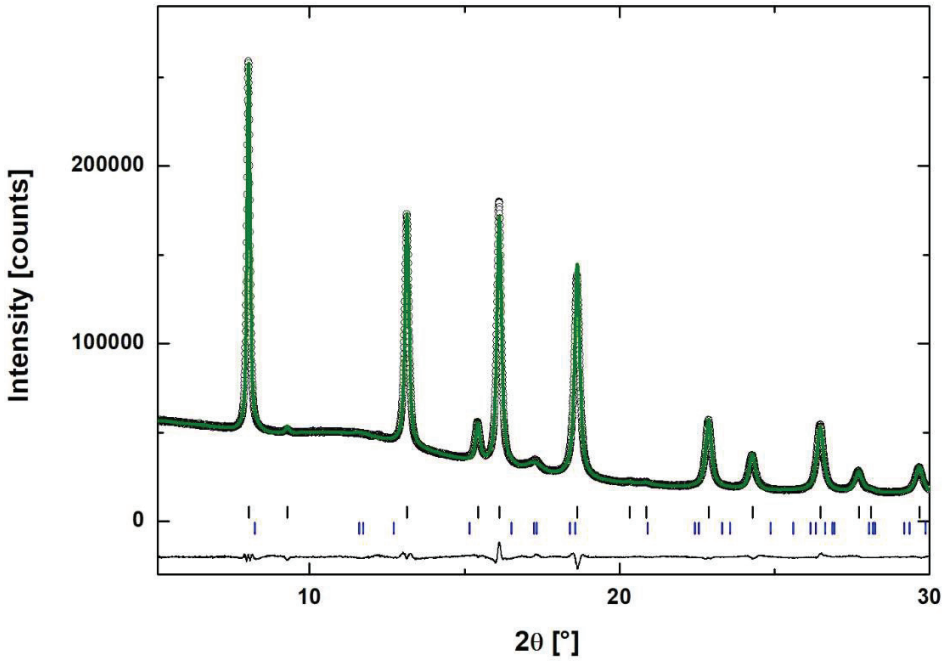

Figure S4. Rietveld refinement of SR-PXD *data of* $Mg_{0.7}Mn_{0.3}(NH_3)_6Cl_2$ *at RT showing the experimental (black circles), calculated (solid green line) and a difference plot (solid black line) below. The vertical ticks mark the Bragg peak positions for* $Mg_{0.7}Mn_{0.3}(NH_3)_6Cl_2$ *(black) and* $Mg_{0.7}Mn_{0.35}(NH_3)_2Cl_2$ *(blue vertical ticks).* R_{wp} *= 1.38 %.* λ*=0.82646 Å*

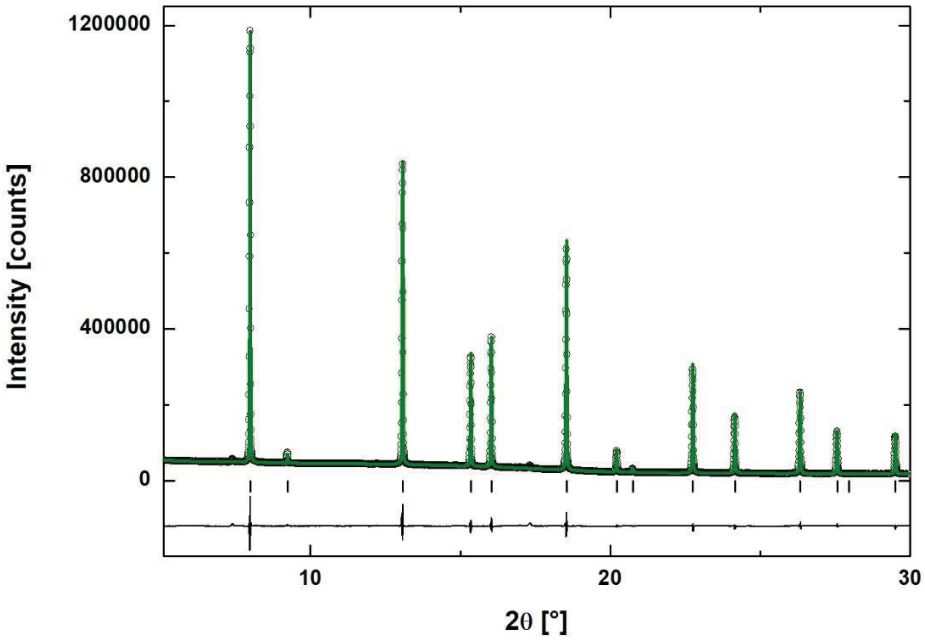

Figure S5. Rietveld refinement of SR-PXD data of $Mn(NH_3)_6Cl_2$ at RT showing the experimental (black circles), calculated (solid green line) and a difference plot (solid black line) below. The vertical ticks mark the Bragg peak positions for $Mn(NH_3)_6Cl_2$. R_{wp} = 2.57 %. λ=0.82646 Å

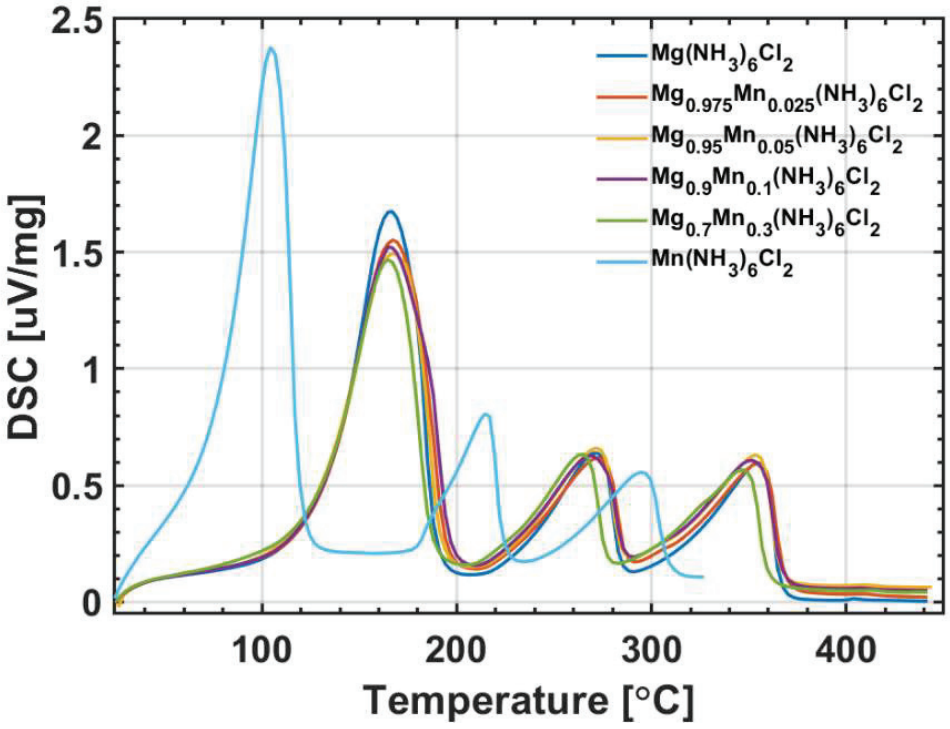

Figure S6. DSC measurements performed on $Mg(NH_3)_6Cl_2$, $Mn(NH_3)_6Cl_2$ and the $Mg_{1-x}Mn_x(NH_3)_6Cl_2$ (x = 0.025, 0.05, 0.1 and 0.3) solid solutions in the temperature range RT to 455 °C, with a heating rate of 5 °C·min^{-1}.

Table S2. The NH_3 desorption onset temperatures of $Mg(NH_3)_6Cl_2$, $Mn(NH_3)_6Cl_2$ and $Mg_{1-x}Mn_x(NH_3)_6Cl_2$ (x = 0.025, 0.05, 0.1 and 0.3) with a heating rate of 5 °C·min^{-1}.

	4NH_3		NH_3		NH_3	
Compound	**Temperature (°C)**	**Mass loss (%)**	**Temperature (°C)**	**Mass loss (%)**	**Temperature (°C)**	**Mass loss (%)**
$Mg(NH_3)_6Cl_2$	130.9	33.6%	228.7	8.7%	316.0	8.5%
$Mg_{0.975}Mn_{0.025}(NH_3)_6Cl_2$	128.7	33.4%	225.5	8.8%	317.1	8.6%
$Mg_{0.95}Mn_{0.05}(NH_3)_6Cl_2$	126.5	33.5%	225.0	8.7%	316.3	8.5%
$Mg_{0.9}Mn_{0.1}(NH_3)_6Cl_2$	127.9	33.3%	224.3	8.7%	310.9	8.6%
$Mg_{0.7}Mn_{0.3}(NH_3)_6Cl_2$	127.7	30.7%	223.2	8.3%	298.3	8.0%
$Mn(NH_3)_6Cl_2$	79.8	29.3%	178.8	7.8%	256.6	7.3%

Table S3. The gravimetric NH_3 capacities of the monometallic and mixed cation hexammines investigated in this study.

Compound	NH_3 (wt%)
$Mg(NH_3)_6Cl_2$	51.8
$Mg_{0.975}Mn_{0.025}(NH_3)_6Cl_2$	51.6
$Mg_{0.95}Mn_{0.05}(NH_3)_6Cl_2$	51.4
$Mg_{0.9}Mn_{0.1}(NH_3)_6Cl_2$	51.0
$Mg_{0.7}Mn_{0.3}(NH_3)_6Cl_2$	49.5
$Mg_{0.5}Mn_{0.5}(NH_3)_6Cl_2$	48.0
$Mn(NH_3)_6Cl_2$	44.8

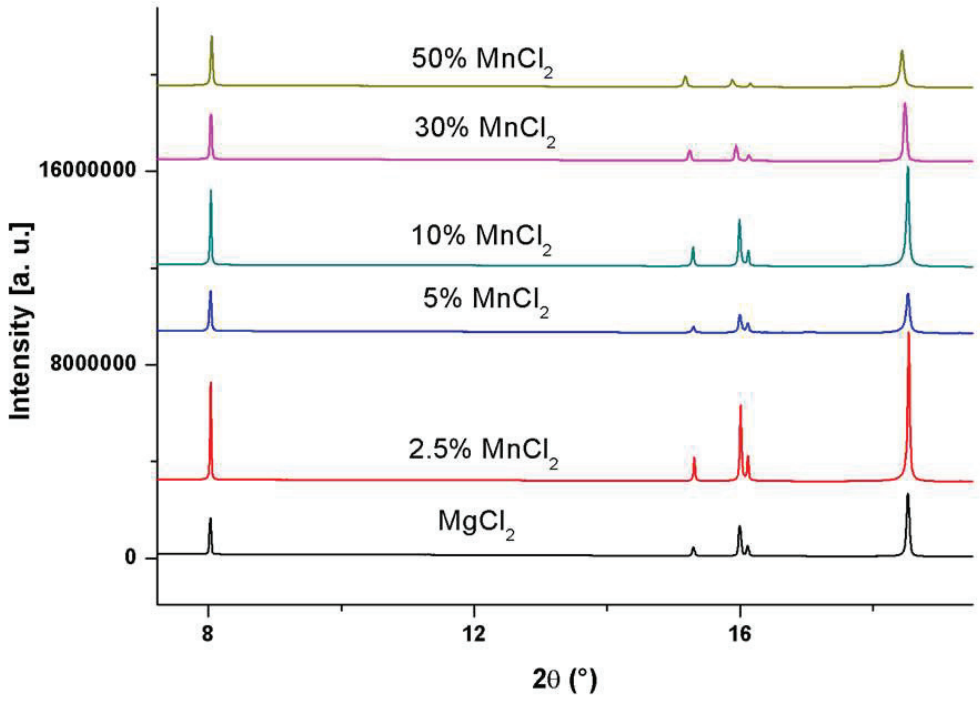

Figure S7. SR-PXD patterns of $Mg_{1-x}Mn_xCl_2$ after one cycle of NH_3 absorption and desorption. The fully desorbed sample was obtained after the TGA-DSC measurement from RT to 455 °C with the heating rate of 5 °C·min^{-1}.

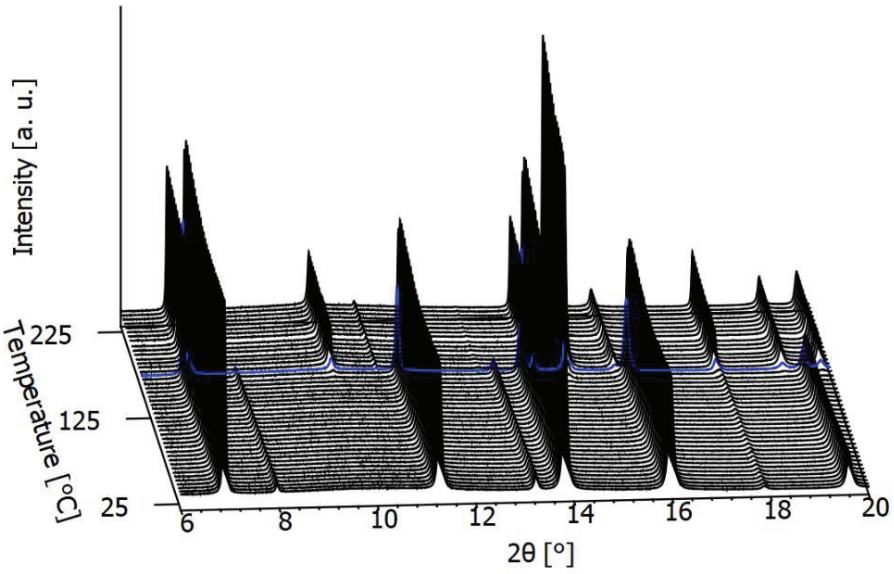

Figure S8. In-situ SR-PXD of $Mg(NH_3)_6Cl_2$ measured from RT to 227 °C with a heating rate 5 °C·min^{-1}. The blue pattern represent the $Mg(NH_3)_2Cl_2$ at T~146 °C. λ=0.709396 Å

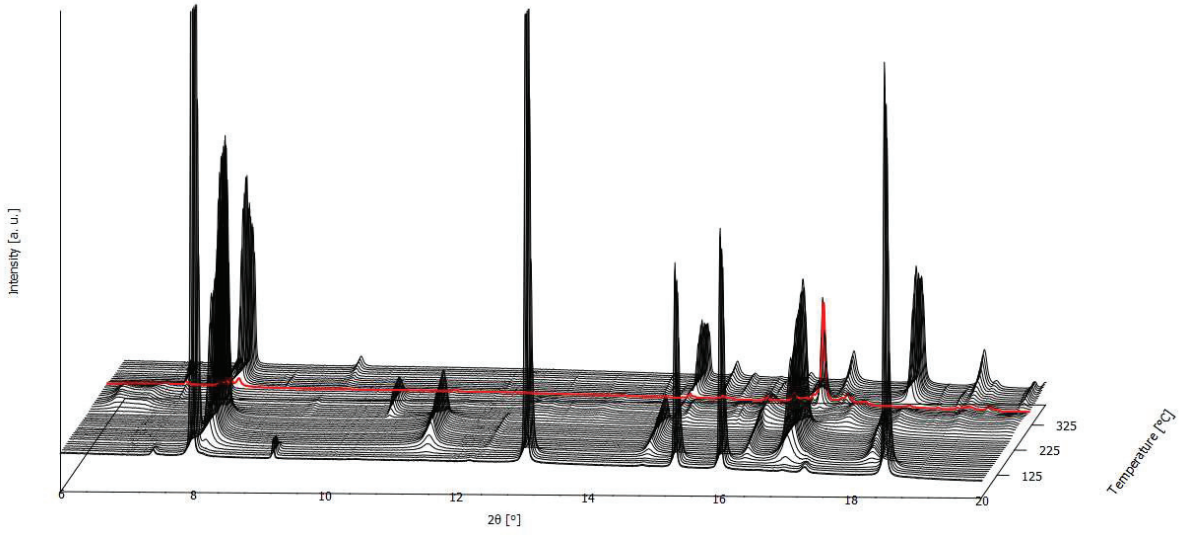

Figure S9. In-situ SR-PXD *of $Mn(NH_3)_6Cl_2$ measured from RT to 406 °C with a heating rate of 5 °C·min^{-1}. The red pattern represent the $Mn(NH_3)_{0.5}Cl_2$ at T~307 °C. λ=0.82646 Å.*

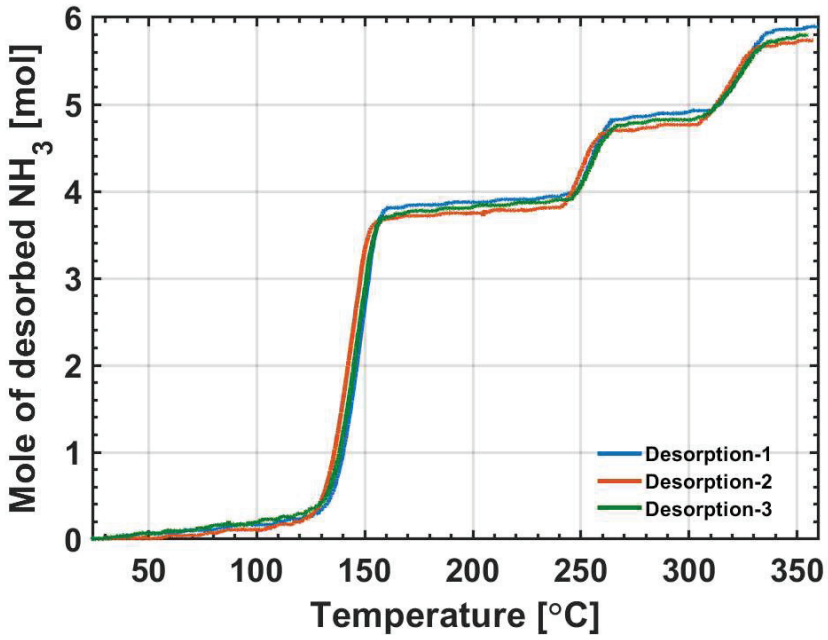

Figure S10. NH_3 desorption upon cycling of $Mg_{0.9}Mn_{0.1}(NH_3)_6Cl_2$.